

Utah State University

DigitalCommons@USU

---

All Graduate Theses and Dissertations

Graduate Studies

---

8-2020

# Storm-Time Equatorial Thermospheric Dynamics and Electrodynamics

Luis A. Navarro Dominguez  
*Utah State University*

Follow this and additional works at: <https://digitalcommons.usu.edu/etd>



Part of the [Physics Commons](#)

---

## Recommended Citation

Navarro Dominguez, Luis A., "Storm-Time Equatorial Thermospheric Dynamics and Electrodynamics" (2020). *All Graduate Theses and Dissertations*. 7847.  
<https://digitalcommons.usu.edu/etd/7847>

This Dissertation is brought to you for free and open access by the Graduate Studies at DigitalCommons@USU. It has been accepted for inclusion in All Graduate Theses and Dissertations by an authorized administrator of DigitalCommons@USU. For more information, please contact [digitalcommons@usu.edu](mailto:digitalcommons@usu.edu).



STORM-TIME EQUATORIAL THERMOSPHERIC DYNAMICS AND  
ELECTRODYNAMICS

by

Luis A. Navarro Dominguez

A dissertation submitted in partial fulfillment  
of the requirements for the degree

of

DOCTOR OF PHILOSOPHY

in

Physics

Approved:

---

Bela G. Fejer, Ph.D.  
Major Professor

---

Ludger Scherliess, Ph.D.  
Committee Member

---

Michael J. Taylor, Ph.D.  
Committee Member

---

Anthony R. Lowry, Ph.D.  
Committee Member

---

David Peak, Ph.D.  
Committee Member

---

Richard S. Inouye, Ph.D.  
Vice Provost for Graduate Studies

UTAH STATE UNIVERSITY  
Logan, Utah

2020

Copyright © Luis A. Navarro Dominguez 2020

All Rights Reserved

## ABSTRACT

## Storm-Time Equatorial Thermospheric Dynamics and Electrodynamics

by

Luis A. Navarro Dominguez, Doctor of Philosophy

Utah State University, 2020

Major Professor: Dr. Bela G. Fejer  
 Department: Physics

We present the first comprehensive study of the equatorial thermospheric dynamics and ionospheric electrodynamics over Peru following enhanced energy depositions into the high-latitude ionosphere during geomagnetic storms. We used extensive observations of ionospheric plasma drifts and of night-time thermospheric neutral winds from the Jicamarca Incoherent Scatter Radar and from the network of Fabry-Perot Interferometers deployed in the central region of Peru respectively. In the first part, empirical seasonal dependent quiet-time neutral wind baselines are derived and compared with current empirical models. Then, we present, for the first time, the seasonal climatology of the equatorial nighttime disturbance winds and their variations under local and extended geomagnetic activity periods. These night-time disturbances are strongest in the east-west direction; they are westward and strongest around midnight. The disturbance winds increase during extended geomagnetic activity periods mostly around midnight and in the postmidnight sector. We present a simple empirical model that provides a significantly more accurate representation of the disturbance winds, particularly during the recovery phase of the storms, than provided by current models. In the second part, we extended the current empirical characterization of storm short-term (time scales between about 3 and 9 hours) storm-time wind-driven



equatorial disturbance dynamo zonal electric fields (vertical plasma drifts) and their dependence on solar flux and level of geomagnetic activity. The vertical disturbance drifts are downward near dusk with largest magnitudes around the equinoxes, where they increase from solar minimum to solar maximum and with the level of geomagnetic activity. Later at night, these disturbance drifts are upward and their magnitudes increase strongly with geomagnetic activity but not much with solar flux. The peak of downward disturbance drifts close to dawn move to later local time with increasing flux. Finally, we show the highly coupled dynamics and electrodynamics of the equatorial zonal ionospheric drifts and thermospheric winds during geomagnetic quiet and disturbed times. The close agreement of the season dependent zonal disturbance drifts and thermospheric winds is presented for the first time. Then, we also present the first experimental evidence of highly correlated perturbations on the zonal drifts and winds due to very short lived (time scales 1-3 hours) prompt penetration electric fields.

(177 pages)

## PUBLIC ABSTRACT

## Storm-Time Equatorial Thermospheric Dynamics and Electrodynamics

Luis A. Navarro Dominguez

We present the first complete study of the dynamics of the equatorial upper atmosphere (180-350 km) during periods of strong magnetic activity driven by the Sun, which are generally referred as geomagnetic storms. These storms have the potential to considerably affect satellite-based communications and navigation systems among other severe technological challenges. We used large databases of two of the most important parameters at these altitudes, which are the velocities of the neutral and ionized gas (plasma) referred to as neutral winds and plasma drifts. These measurements were acquired in the Peruvian equatorial region by the Jicamarca radar and by a network of optical instruments nearby. In the first part, we derived average patterns of the neutral winds under weak geomagnetic activity conditions, or quiet times, for different seasons and compared them with predictions from current upper-atmospheric models. Then, we present, for the first time, the seasonal patterns of the night-time perturbations in the neutral winds at equatorial latitudes, and their variations for different solar-driven geomagnetic storms. These wind perturbations are strongest in the east-west direction and around midnight. They are strongest and longer lasting during and after extended periods of geomagnetic activity. We present a simple empirical model that significantly improves the prediction of the perturbations in the neutral winds compared with current models. In the second part, we derive the velocity perturbations in the plasma drifts along the vertical direction following 3 to 9 hours of geomagnetic activity. We show in detail that these vertical velocity perturbations are small and downward during the day and upward and stronger at night, and vary throughout the year and for different solar conditions. They are strongest near sunrise and sunset and during the equinoxes. In the last part of the thesis, we show the close relationship of the neutral wind

and plasma drift velocities along the east-west direction during both geomagnetic quiet and disturbed conditions. Finally, we summarize our main results and make suggestions to improve the understanding of this important topic.

For two splendid women,  
Elena & Daniela.

## ACKNOWLEDGMENTS

First, I would like to thank Prof. Bela Gyula Fejer from whom I learned the real meaning of the phrase “Standing on the shoulders of giants”, and for the countless conversations about science, life and politics. I will always be grateful for your role model, help and support. Second, I would like to thank Prof. John Williams Meriwether, Jr who first believed on my professional potential, and who has proved to be a sincere friend and mentor. Third, thanks to Dr. Marco Antonio Milla Bravo whom example inspired me to pursue a career on this field. I also would like to thanks the members of my committee Profs. Lowry, Peak, Taylor and Scherliess for their assistance on this manuscript.

I would also like to thank my wife, Daniela, and my family for their love and support over the past few years, and during my entire life. You have all helped me to build a better future for all of us. To my parents whose example I carry deep within myself, to my sister for her always warm friendship, and to my wife for her encouragement and charismatic support. Also, my gratitude to Richard, Jane, Pat, Barty, Ivana, Ken, Neal, Debrup and to the Taylor family for their sincere friendship and generosity during our stay in Logan.

This work could not be possible without the support and help of the staff of the Jicamarca Radio Observatory. Their strong commitment is the foundation of the success of this facility. In particular, to Oscar and Ricardo. Also, thanks to the staff of the Center for Atmospheric and Space Sciences and of the Physics Department, in particular to Karalee and Vanessa. And, to Dr. Harding for providing his work on the estimation of wind fields.

This work was supported by the NASA H-LWS program through grant 80NSSC17K071 and by fellowships from the Howard L. Blood Endowment. The Jicamarca Radio Observatory is a facility of the Instituto Geofisico del Peru operated with support from NSF award AGS-1732209 through Cornell University. The Fabry-Perot Interferometer network in Peru is operated and maintained by technicians and engineers at JRO with support from Clemson University and New Jersey Institute of Technology.

Luis Navarro

## CONTENTS

	Page
ABSTRACT .....	iii
PUBLIC ABSTRACT .....	v
DEDICATION .....	vii
ACKNOWLEDGMENTS .....	viii
LIST OF TABLES .....	xii
LIST OF FIGURES .....	xiii
ACRONYMS .....	xvii
CHAPTER	
1 INTRODUCTION .....	1
1.1 Earth's Thermosphere and Ionosphere .....	1
1.2 Overview of this work .....	3
2 EQUATORIAL THERMOSPHERIC WINDS AND IONOSPHERIC ELECTRIC FIELDS .....	6
2.1 Introduction .....	6
2.1.1 Solar and Geomagnetic Indices .....	7
2.2 Thermospheric Winds .....	8
2.2.1 Quiet-time Dynamics .....	8
2.2.1.1 Equatorial Thermospheric Winds .....	10
2.2.2 Disturbance Thermospheric Winds .....	13
2.2.2.1 Equatorial Disturbance Winds .....	17
2.3 Ionospheric Plasma Drifts .....	22
2.3.1 Quiet-time Electrodynamics .....	22
2.3.1.1 Equatorial Plasma Drifts .....	22
2.3.2 Storm-time Equatorial Ionospheric Electric Fields .....	27
2.3.2.1 Prompt Penetration Electric Fields .....	28
2.3.2.2 Disturbance Dynamo Electric fields .....	29
3 DATA AND METHODOLOGY .....	35
3.1 Fabry-Perot Interferometers .....	35
3.1.1 Oxygen line emission .....	35
3.1.2 Optical principle and instrumental modeling .....	38
3.1.3 Network of Fabry-Perot Interferometers .....	42
3.1.4 Wind Velocity Estimation .....	46
3.1.5 Database and statistics .....	49

3.2	Jicamarca Incoherent Scatter Radar . . . . .	50
4	STORM-TIME THERMOSPHERIC WINDS OVER PERU . . . . .	56
4.1	Introduction . . . . .	56
4.2	Measurement Technique . . . . .	59
4.3	Results . . . . .	62
4.3.1	Quiet-time average winds . . . . .	62
4.3.2	Average disturbance winds . . . . .	68
4.3.3	Extended geomagnetic effects . . . . .	73
4.3.4	Case studies . . . . .	76
4.4	Discussion . . . . .	82
4.5	Summary and conclusions . . . . .	83
5	EQUATORIAL DISTURBANCE DYNAMO VERTICAL PLASMA DRIFTS OVER JICAMARCA . . . . .	85
5.1	Introduction . . . . .	85
5.2	Data and Methodology . . . . .	89
5.3	Results . . . . .	91
5.4	Discussion . . . . .	99
5.5	Summary and conclusions . . . . .	101
6	STORM-TIME COUPLING OF EQUATORIAL ZONAL PLASMA DRIFTS AND NEUTRAL WINDS . . . . .	103
6.1	Introduction . . . . .	103
6.2	Data and Methodology . . . . .	107
6.3	Results . . . . .	108
6.4	Discussion . . . . .	117
6.5	Summary and Conclusions . . . . .	120
7	SUMMARY AND FUTURE WORK . . . . .	121
7.1	Summary and Conclusions . . . . .	121
7.1.1	On the disturbance winds . . . . .	121
7.1.2	On the disturbance dynamo vertical drifts . . . . .	122
7.1.3	On the storm-time coupling of zonal plasma drifts and neutral winds . . . . .	124
7.2	Suggestions for Future Work . . . . .	124
	REFERENCES . . . . .	127
	APPENDIX . . . . .	143
	CURRICULUM VITAE . . . . .	157

## LIST OF TABLES

Table		Page
3.1	Technical Characteristics of the Fabry-Perot Interferometer network in Peru.	44
3.2	Number of hours of data available for each FPI station and for each year. .	49
4.1	Seasonal Distribution of the 15-min averaged Wind Field Database. . . . .	62
5.1	Bimonthly Distribution of the Jicamarca Vertical Disturbance Drifts . . . .	91
6.1	Seasonal Distribution of the 15-min averaged Jicamarca Zonal Drifts. . . . .	108



## LIST OF FIGURES

Figure	Page
1.1 Typical profiles of neutral atmospheric temperature and plasma density with the various layers (After Kelley, 2009). . . . .	2
2.1 Global Thermospheric Wind Circulation for June, December and March. . .	10
2.2 Climatological (right) zonal and (left) meridional equatorial thermospheric winds and model results for high and low solar flux and geomagnetically quiet conditions for Arequipa FPI during equinox (Adapted from Biondi et al., 1999). . . . .	11
2.3 Seasonal comparison of the (bottom) zonal and (top) meridional equatorial thermospheric wind for geomagnetically quiet ( $K_p < 3$ ) and moderate low solar flux conditions for the Arequipa FPI, and predictions from HWM07 and HWM14 (Adapted from Drob et al., 2015). . . . .	13
2.4 Sketch diagram of the wind dynamo on both poles during a geomagnetic storm. . . . .	15
2.5 Horizontal disturbance winds for an average $K_p=4$ from WINDII observations (Adapted from Emmert et al., 2004). . . . .	17
2.6 Average disturbance winds as function of magnetic local time (MLT) for three increasing geomagnetic activity levels and for different magnetic latitudes (After Emmert et al., 2004). . . . .	18
2.7 Average zonal disturbance winds from Arequipa FPI data, UARS/WINDII data, and DE 2/WATS data as a function of $K_p$ . . . . .	19
2.8 Equatorial thermospheric response for the 25-29 August 1998 storm using Arequipa FPI observations. . . . .	21
2.9 Seasonal and solar flux comparison of the quiet-time vertical plasma drifts using Scherliess-Fejer model and averages from Jicamarca observations for equinox, June solstice and December solstice; and for low, medium and high. . . . .	23
2.10 Seasonal and solar flux comparison of the quiet-time zonal plasma drifts using Fejer model and averages from Jicamarca observations for equinox, June solstice and December solstice (After Fejer et al., 2005). . . . .	25

2.11	Annual variation of the quiet-time zonal drifts over Jicamarca for (top) solar minimum and (bottom) solar maximum. . . . .	26
2.12	Equatorial vertical plasma drifts for the August 1972 storm. . . . .	28
2.13	Sketch diagram of the Ionospheric Disturbance dynamo Model. . . . .	30
2.14	Local time variation of the equatorial disturbance dynamo vertical drift following 9-hours of high geomagnetic activity conditions (After Scherliess & Fejer, 1997). . . . .	32
2.15	Fejer model predictions (solid) of the equatorial disturbance zonal drift for low (right) and high (left) solar flux conditions and different seasons (After Fejer et al., 2005). . . . .	33
3.1	Oxygen line emission following a Gaussian distribution with Doppler shift, $\Delta\lambda$ , and broadening, $\sigma_T$ . . . . .	38
3.2	Diagram showing the optical path of an incoming oxygen line emission going through the basic elements of a Fabry-Perot Interferometer. . . . .	39
3.3	Example output for the analysis of a 630 nm airglow image. . . . .	42
3.4	Drawing of the optical mount of the FPIs at Jicamarca and Nasca. (Courtesy of Prof. Meriwether from Clemson University). . . . .	43
3.5	Examples of Interferometric ring patterns for the Arequipa (left), Jicamarca (middle) and Nasca (right) FPIs. . . . .	45
3.6	Estimated wind field map over central Peru for 21th June 2012 around 02 LT. . . . .	48
3.7	Monthly distribution of data available for Jicamarca (top), Arequipa (middle) and Nasca (bottom) FPIs since 2009. . . . .	50
3.8	View of the Jicamarca Radio Observatory. . . . .	52
3.9	Jicamarca vertical and zonal drifts observations from the 22 January 2014. . . . .	54
4.1	Estimated wind field map over central Peru for 16th May 2013 around midnight ( $\sim 23:45$ LT) . . . . .	61
4.2	Comparison of equatorial thermospheric eastward winds for Equinox under (red) local, (green) 12-hours and (blue) 48-hours extended quiet conditions. . . . .	63
4.3	Annual variation and local time dependence of the night-time thermospheric (top) zonal and (bottom) meridional winds for geomagnetically quiet conditions over Peru. . . . .	65

4.4	Seasonal variation of equatorial thermospheric winds under 12-hours of extended geomagnetic quiet conditions and the corresponding quiet-time predictions from the HWM14. . . . .	67
4.5	Seasonal comparison of disturbed equatorial thermospheric winds for local geomagnetic conditions i.e. $K_p > 3$ ; and corresponding predictions from the HWM14 evaluated for $A_p = 25$ . . . . .	69
4.6	Comparison of 12-hours extended quiet and local disturbed thermospheric winds over Peru. . . . .	70
4.7	Local time and seasonal comparisons of FPI disturbance winds ( $K_p > 3$ ) with predictions from the DWM07 for geomagnetic activity enhancement of $\Delta K_p = 3.2$ ( $A_p \approx 25$ ). . . . .	71
4.8	Averaged FPI and DWM07 disturbance winds as a function of local $K_p$ for the midnight period. . . . .	73
4.9	Comparison of equinoctial disturbance eastward winds under local and extended geomagnetically active conditions. . . . .	75
4.10	Disturbance eastward winds of 9-hours extended geomagnetically active conditions for March-June period. . . . .	77
4.11	Thermospheric wind response during the 07-10 May 2016 geomagnetic storm. . . . .	79
4.12	Thermospheric wind response during the 23-26 April 2012 geomagnetic storm. . . . .	81
5.1	Comparison of the bimonthly half-hourly averaged vertical drifts and predictions from Scherliess (1997). . . . .	90
5.2	Scatter plot of season dependent disturbance dynamo drifts after 6 hours of enhanced geomagnetic activity. . . . .	92
5.3	Bimonthly averages of disturbance vertical drifts for moderate flux conditions. . . . .	94
5.4	Annual variation and local time dependence of disturbance vertical drifts for moderate flux conditions. . . . .	96
5.5	Annual variation of the disturbance dynamo vertical drifts for low (green) and high (blue) magnetically active conditions. . . . .	97
5.6	Annual variation of disturbance dynamo vertical drifts for low (green) and high (blue) solar flux conditions. . . . .	99

6.1	Quiet-time zonal plasma drifts and nighttime thermospheric winds. . . . .	109
6.2	Seasonal comparison of the disturbance zonal drifts and winds. . . . .	111
6.3	Time evolution of equatorial zonal plasma drifts and neutral winds for the 06-09 September 2017 storm. . . . .	113
6.4	Comparison of thermospheric winds and ionospheric drifts during the September 2017 storm.. . . .	115
6.5	Time evolution of equatorial zonal plasma drifts and neutral winds for the 25-28 August 2015 storm. . . . .	117

## ACRONYMS

EUV	extreme ultraviolet (related to solar radiation)
AE	Auroral Electrojet (related to geomagnetic index)
AL	Auroral Lower (related to geomagnetic index)
AU	Auroral Upper (related to geomagnetic index)
PC	Polar Cap (related to geomagnetic index)
SYM-H	Symmetric-H (related to geomagnetic index)
DST	Disturbance (related to geomagnetic index)
NCAR	National Center for Atmospheric Research
TIEGCM	Thermosphere Ionosphere Electrodynamic General Circulation Model
HWM	Horizontal Wind Model
DWM	Disturbance Wind Model
FPI	Fabry-Perot Interferometer
ISR	Incoherent Scatter Radar
JRO	Jicamarca Radio Observatory
TAD	Traveling Atmospheric Disturbances
EPB	Equatorial Plasma Bubbles
DE-2	Dynamics Explorer-2 (satellite)
WATS	Wind and Temperature Spectrometer (related to DE-2)
UARS	Upper Atmosphere Research Satellite
WINDII	Wind Imaging Interferometer (related to UARS)
CHAMP	Challenging Minisatellite Payload (satellite)
ROCSAT-1	Republic of China Satellite-1
C/NOFS	Communication/Navigation Outage Forecasting System (satellite)
ICON	Ionospheric Connection Explorer (satellite)

## CHAPTER 1

### INTRODUCTION

#### 1.1 Earth's Thermosphere and Ionosphere

Earth's atmosphere is the near-space region surrounding Earth that is influenced by Earth's gravity. It extends up to about 100,000 km and it is horizontally stratified in regions. Its structure has been organized depending based on different features and processes. The most widely used, and the ones important for this dissertation, are the organizations related to the temperature of the neutral gas and to the plasma density of the ionized gas. The ionized gas is referred to the ionosphere which is the region where there are sufficient ions and electrons to affect the propagation of electromagnetic waves.

Figure 1.1 shows typical vertical structures of the neutral and ionized gases with its corresponding regions. The neutral gas is classified into four thermal regions from which only the mesosphere and the thermosphere are affected by the ionosphere. We will focus on the thermosphere which is the main focus of this dissertation. The thermosphere has a strong temperature increase in its lower boundary due to the absorption of extreme ultraviolet (EUV) radiation from the sun, and reach a steady temperature above about 300 km. The EUV absorption produces a thermal expansion of the thermospheric neutral gas producing an atmospheric circulation that is generally referred to as thermospheric wind system. It also produces ionization of the neutral gas generating ions, electrons and associated currents, which form the ionosphere ([Rishbeth & Garriot, 1969](#); [Prölss, 2004](#)).

The vertical structure of the ionosphere is determined by the relative ratio of ionization and recombination and by the importance of transport processes. As seen in Figure 1.1, its vertical structure can significantly change from day to night. The ionospheric regions are known as D, E, F regions and protonosphere with strong differences in density but also in composition. We will focus on the F-region which is also a main focus of this dissertation.

The F-region shows a peak density and ranges from 150 to about 500 km. The dominant ion species is the oxygen ion. The topside ionosphere is the general term applied to the regions above the F-region peak. Above this altitude, in the protonosphere, the plasma density is determined by transport processes like ambipolar diffusion, neutral wind drag and electrodynamics rather than local ionization ([Kelley, 2009](#); [Schunk & Nagy, 2009](#)).

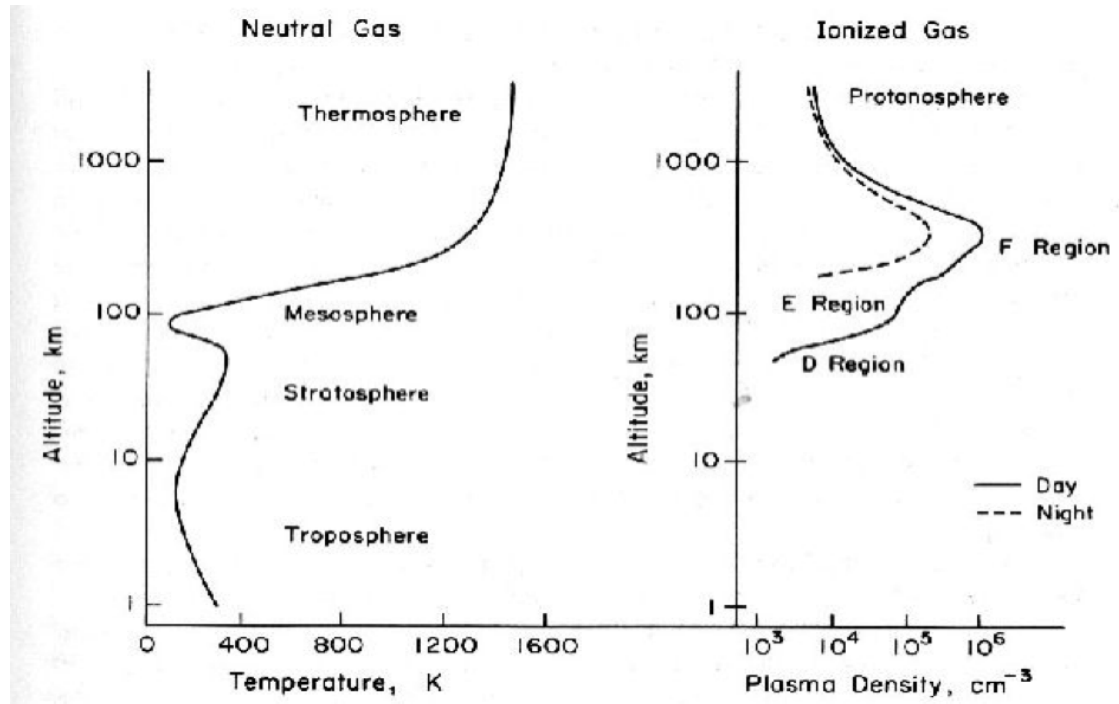


Figure. 1.1: Typical profiles of neutral atmospheric temperature and plasma density with the various layers (After [Kelley, 2009](#)).

Thermospheric winds, driven by daily pressure variations due to solar heating, set the charged particles of the F-region ionosphere into motion. This motion is the drifts of ions and electrons along Earth's magnetic field lines ([Rishbeth, 1971a](#)). The geometry of the Earth's magnetic field imposes different effects on the plasma density distribution and on the thermospheric dynamics and electrodynamics. This geometry leads to the latitudinal classification of high-, mid- and low-latitude that is widely used in aeronomy studies. At high

latitude, the ionosphere is directly connected to the magnetosphere through the magnetic field lines. This coupling provides a dominant source of energy from particle precipitation and strong magnetic fields which drive the high-latitude convection and impart momentum into the thermospheric winds. At mid latitudes, the height of the F-region electron density is mainly affected by the transport of neutral winds, diffusion and recombination. At low latitudes, the magnetic field is nearly horizontal which results in unique transport effects and on unique phenomena associated with the upward motion of the plasma drifts. Equatorial ionosphere and thermosphere is generally referred to the latitudinal region below about  $15^\circ$ .

The dynamics and electrodynamics of the thermosphere have been extensively studied in the past five decades using ground- and space-based instrumentation and theoretical models (Kelley, 2009; Richmond, 2016; Schunk & Nagy, 2009). However, there are still outstanding questions regarding the strong variations observed in the equatorial thermospheric winds and ionospheric F-region plasma drifts during periods of strong magnetic activity or geomagnetic storms (Fejer et al., 2017). During these periods, ionospheric electric currents variations at the high latitude ionosphere generates global wide changes in the thermospheric winds and in the ionospheric drifts that propagates to equatorial latitudes at different spatial and time scales. The equatorial thermospheric winds are affected through a disturbance wind circulation that propagates equatorward from Joule heated regions at high latitudes. The equatorial ionospheric drifts are affected through two main sources related to the penetration of electric fields of magnetospheric origin, and to the ionospheric disturbance dynamo electric fields which are also related to the Joule heating of the high latitude ionosphere. On this dissertation we will focus on the effects of the disturbance thermospheric winds and on the ionospheric disturbance dynamo drifts at equatorial latitudes.

## 1.2 Overview of this work

In this dissertation we present a comprehensive climatological study of the equatorial thermospheric winds and of the ionospheric drifts during geomagnetically active periods over Peru. The disturbances covered on this study are mostly related to Joule-heating-



driven wind disturbances and to disturbance dynamo effects. Other storm-time effects on the ionospheric drifts, the prompt penetration electric fields, are not covered by this study, except for a specific storm case when the effects of these disturbances are observed in winds and drifts for the first time.

We have used thermospheric winds and F-region ionospheric plasma drifts observations from the network of Fabry-Perot Interferometers recently deployed in the central region of Peru, and from the Jicamarca incoherent scatter radar in Peru respectively. The database used on this study extends from 2011 for the thermospheric winds and from 1968 for the ionospheric plasma drifts.

The focus of this dissertation will have a major emphasis on the equatorial thermospheric winds. The seasonal dependence of the equatorial disturbance winds and the empirical representation of these disturbances during long storms considering not only the current but also previous values of the magnetic activity are presented for the first time. The extensive ionospheric plasma drifts database is used to present the most detailed study of the shorter time scale (between about 3 and 9 hours) equatorial disturbance vertical plasma drifts as another major point on this dissertation. Finally, we show for the first time the strong coupling under disturbance dynamo and prompt penetration electric fields between zonal plasma drifts and neutral winds.

This dissertation comprises seven chapters. In this first chapter, we present an introduction to Earth's upper atmosphere. Chapter 2 presents the background information needed to understand the thermospheric winds and ionospheric electric fields during geomagnetically quiet and, in particular, active conditions. Chapter 3 describes the instrumentation, processing methodology and database of the thermospheric winds, and an overview of the ionospheric plasma drifts used on this study. Chapter 4 presents initially the quiet-time seasonal dependent equatorial thermospheric winds. Later, presents the seasonal dependence of the equatorial disturbance winds and outlines a simple empirical model that significantly improves the prediction of thermospheric winds for long storm cases also presented. These results are also compared with existing empirical models. Chapter 5 presents the solar flux

and geomagnetic activity dependence of the annual variation of the equatorial disturbance dynamo vertical plasma drifts. Chapter 6 presents initially the strong drifts and winds coupling using climatological averages of the zonal plasma drifts and zonal neutral winds during quiet- and storm-time conditions. Later, presents strong winds and drift coupling during prompt penetration and disturbance dynamo electric fields for two storm cases. Chapter 7 summarized our major conclusions and present suggestions for further studies of the equatorial disturbance winds, equatorial disturbance dynamo drifts and their coupling.

## CHAPTER 2

### EQUATORIAL THERMOSPHERIC WINDS AND IONOSPHERIC ELECTRIC FIELDS

#### 2.1 Introduction

The equatorial thermospheric winds and ionospheric plasma drifts are the most important parameters to understand the low latitude dynamics and electrodynamics. These parameters can show large departures from their regular quiet-time patterns during periods of strong magnetic activity, generally referred as geomagnetic storms. On this sense, there has been extensive efforts to deploy and maintain instrumentation, and to develop theoretical and empirical models which led to significant progress on understanding the morphology, dynamos and coupling relationships responsible for these observations. However, even though quiet-time dynamics and electrodynamics are fairly well understood, the disturbances during storm-time periods are still not fully accounted by current empirical or theoretical models.

In this chapter we will introduce the essential background information needed to understand the global variations in the equatorial thermosphere and ionosphere during storm-time conditions. First, we will briefly describe the quiet-time thermospheric winds especially under low and equatorial latitudes. Then, we will describe the storm-time variations of the low-latitude and equatorial thermospheric winds. Later, we will briefly describe the quiet-time equatorial ionospheric vertical and zonal plasma drifts. Finally, we will describe the variations of the equatorial ionospheric plasma drifts under storm-time conditions. We will discuss briefly prompt penetration electric fields, and then, in more detail, the equatorial disturbance dynamo electric fields. A major emphasis will be given to the equatorial disturbance winds and to the equatorial ionospheric disturbance dynamo drifts which are the main focus of this dissertation.

### 2.1.1 Solar and Geomagnetic Indices

One of the most important indices to monitor the solar activity is the Covington index or solar flux index (F10.7). It was first introduced by [Covington \(1947\)](#) and have been measured since 1947 in Canada. It corresponds to the mean spectral energy flux density of the solar disk measured at a frequency of 2.8GHz, or wavelength of 10.7 cm, in units of  $10^{-22} \text{ Wm}^{-2} \text{ Hz}^{-1}$ . These flux densities are generally referred in solar flux units (sfu). They range from 50, for solar quiet activity conditions, and up to 300, for extremely solar activity conditions. They are statistically correlated with the EUV and X-ray radiation intensities, and so they are regularly used as a good proxy for the daily level of ionization ([Prölss, 2004](#)). For detailed information about this index, the reader might refer to [Prölss \(2004\)](#) or [Tapping \(2013\)](#) and references therein.

Similarly, several indices are used to monitor magnetic field fluctuations on Earth's magnetic field. These disturbances are complex, global wide and have effects on different time and spatial scales on the ionosphere and thermosphere. The most common geomagnetic index used for low and mid latitudes upper atmospheric studies is the 3-hour Kp index, introduced by Bartels in 1932 ([Bartels et al., 1939](#)). It is calculated from magnetic field's fluctuations at 13 observatories at midlatitudes in both hemispheres and ranges from 0 to 9 from geomagnetically quiet to active conditions in steps of  $1/3$  units.

The auroral electrojet, or AE index introduced by [Davis and Sugiura \(1966\)](#), is based on magnetic activity fluctuations around the auroral zone, and so it is a good proxy for current enhancements due to energy injections within the auroral oval. It is derived every minute from an array of 12 observatories deployed along the auroral zone in the northern hemisphere. The observations from the entire array are used to calculate the maximum and minimum deviations with respect to a monthly quiet-time baseline previously determined. These values are referred as Auroral Upper, AU index, and Auroral Lower, AL, respectively. The AE index is later calculated as the differences between them. This index is compiled and provided by the World Data Center C for Geomagnetism at Kyoto, Japan. For more information about this index, the reader might refer to [Mayaud \(1980\)](#).

Finally, the Symmetric-H index, or SYM-H, is a good proxy for the geomagnetic disturbances of the horizontal component, or H-component, of the magnetic field at mid and low latitudes, and to monitor the state of the geomagnetic storms. It is derived every minute and is very well correlated to the Disturbance index, or DST index. The Dst index is an hourly index that monitors the state of the H-component of the magnetic field at low latitudes. It is generally used to monitor the different phases of the geomagnetic storms. The storms are generally seen on this index as sharp decreases followed by slow recovery on the magnitude of this index. The strength of the storm can also be classified depending on how low this index got. Some classifications state strong storms for DST index slower than -80 nT ([Gonzalez et al., 1994](#)). Thus, DST and SYM-H index are good indicators of the magnetic state of the ring current and to discern between different storm phases. Similarly, this index is compiled and provided by the World Data Center C for Geomagnetism at Kyoto, Japan. For more information about this index, the reader might refer to [Mayaud \(1980\)](#), [Gonzalez et al. \(1994\)](#) or [Wanliss and Showalter \(2006\)](#) and references therein.

## 2.2 Thermospheric Winds

### 2.2.1 Quiet-time Dynamics

Thermospheric winds are intrinsically important parameters and have a large and global impact on the structure and composition of the upper atmosphere, and are key drivers of ionospheric electric fields. Their circulation is fueled by the thermal expansion of the neutral gas due to solar atmospheric heating as a consequence of the absorption of the Extreme UltraViolet (EUV) radiation ([Prölss, 2004](#)). This expansion forms a diurnal pressure bulge and gives rise to the horizontal pressure gradients that ultimately drives the horizontal winds system. This airflow, also denoted tidal winds because of its 24 hours periodicity, is outward from the peak location of the bulge. This peak location follows the seasonal location of the subsolar point in latitude and is shifted about 2 hours in longitude (e.g., [Jacchia & Slowey, 1966](#)).

Several other forces are also important drivers of the thermospheric circulation and they are expressed in the momentum equation,

$$\frac{D\bar{u}}{Dt} = -\frac{1}{\rho}\nabla\rho - 2(\bar{\Omega} \times \bar{u}) - v_{in}(\bar{u} - \bar{v}) + \bar{g} + \frac{1}{\rho}\nabla(u\nabla u)$$

where  $\bar{u}$ ,  $\bar{\Omega}$ ,  $\bar{v}$ ,  $\bar{g}$ ,  $\rho$ ,  $v_{in}$  are the neutral wind velocity, Earth's rotational velocity, ion velocity, gravity, mass density and ion-neutral collision frequency. The left-hand term corresponds to the convective derivative of the neutral gas which include acceleration of the neutral gas and also changes due to advection. The right-hand terms correspond to forces due to pressure gradient, Coriolis, ion drag, gravity and viscosity respectively. This equation is not self-consistent to solve for the neutral winds and it is used along with other equations for this end by theoretical models such like the Thermosphere Ionosphere Electrodynamic General Circulation Model (TIEGCM) developed by the National Center for Atmospheric Research (NCAR) (e.g., [Qian et al., 2014](#); [Richmond et al., 1992](#); [Roble et al., 1988](#)).

Figure 2.1 shows the horizontal wind circulation for June, December and March at 00 UT and moderate solar activity conditions, F107=100, and geomagnetically quiet conditions, Kp=2+, simulated by [Rishbeth et al. \(2000\)](#). They are representative of June solstice, December solstice and Equinox respectively and the letters N, S, SP denote the geographic locations of the North and South magnetic poles, and subsolar point respectively. It shows how the global circulation of thermospheric winds follow the sub solar point. They show the diurnal bulge to be the main driver for the thermospheric wind circulation producing an overall summer-to-winter circulation for solstices and quasi symmetric from equator towards poles at equinox. The polar winds are strongly controlled by ion drag where the ion-neutral collision frequency is sufficiently large and acts over a sufficient length of time ([Richmond, 1995a](#)). This circulation has strong consequences on the global composition and on the F2-layer variation ([Rishbeth et al., 2000](#)). For a deeper discussion on the momentum equation, the reader might refer to [Rishbeth and Garriot \(1969\)](#), [Rishbeth \(1972a\)](#) and [Pröls \(2004\)](#).

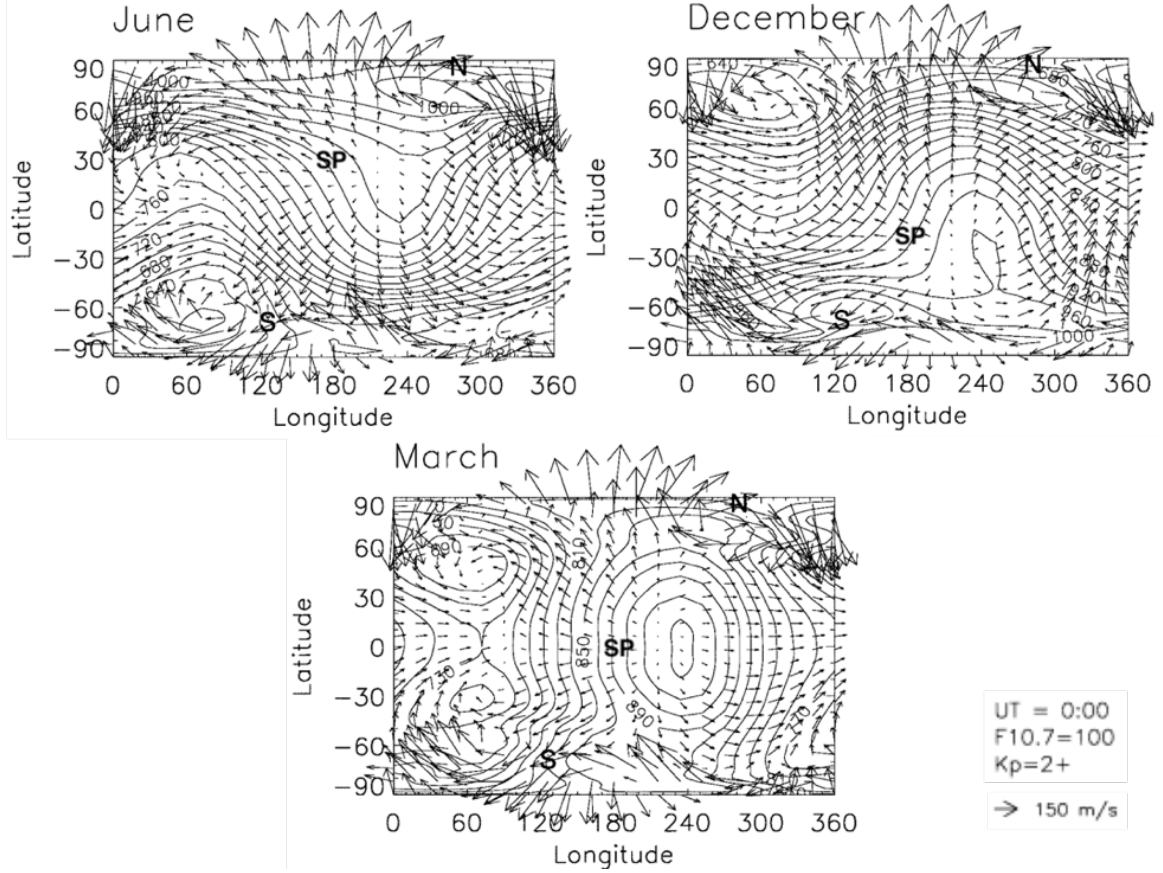


Figure. 2.1: Global Thermospheric Wind Circulation for June, December and March. Noon meridional is at center of each box. Letters N, S and SP indicate positions of the North and South magnetic poles, and the subsolar point (Adapted from [Rishbeth et al., 2000](#)).

### 2.2.1.1 Equatorial Thermospheric Winds

At the magnetic equator, several studies have used measurements from the Fabry-Perot Interferometer (FPI) located at Arequipa, Peru ( $16^{\circ}28' \text{ S}$ ,  $71^{\circ}30' \text{ W}$ , magnetic latitude  $\sim 6.7^{\circ} \text{ S}$ ) which routinely monitored the night-time thermospheric winds since 1984. [Biondi et al. \(1990, 1991, 1999\)](#), [Meriwether et al. \(1986, 2008\)](#) and [Emmert et al. \(2006\)](#) determined the local time, seasonal and solar flux dependence of the geomagnetically quiet nighttime equatorial thermospheric winds only during June solstice and Equinox due to the large uncertainty of the observations during December solstice caused by the high frequency

of cloudy nights (Meriwether et al., 1986, 2008) and by the high occurrence of plasma irregularities during this season (Fejer et al., 1999).

The equatorial night-time winds are eastward with stronger magnitudes before midnight in the zonal direction, and have small magnitudes in the meridional direction, except at early night for June solstice and Equinox when they start southward. They modestly increase for increasing solar flux conditions. Their temporal and seasonal variations are mostly driven by pressure gradients and by the location of the diurnal bulge, and the increasing solar flux variations on the zonal winds are balanced out by stronger ion drag due to increasing ionospheric F-region plasma density. Figure 2.2 shows some results of the early climatology studies using Arequipa FPI observations and models predictions from 1983 to 1990. It shows hourly averages, multivariate regression estimates and TIEGCM predictions for geomagnetically quiet conditions ( $K_p \leq 3$ ) during equinox (Mar-April, Sep-Oct) and for low ( $S_a=94$ ) and high ( $S_a=176$ ) solar flux activity conditions.

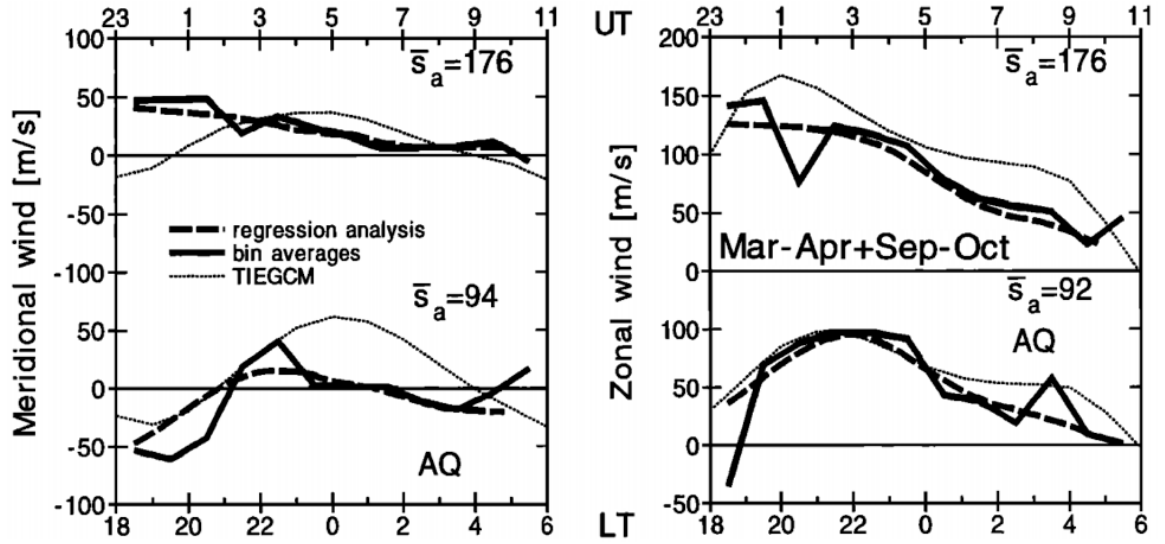


Figure. 2.2: Climatological (right) zonal and (left) meridional equatorial thermospheric winds and model results for high and low solar flux and geomagnetically quiet conditions for Arequipa FPI during equinox (Adapted from Biondi et al., 1999).



Recently deployed FPIs at Jicamarca ( $11^{\circ}57'$  S,  $76^{\circ}51'$  W, magnetic latitude  $\sim 2^{\circ}$  S), and Nasca ( $14^{\circ}58'$  S,  $74^{\circ}53'$  W, magnetic latitude  $\sim 5^{\circ}$  S) since 2009 and 2011 respectively have been also used for different studies and to update empirical models. [Meriwether et al. \(2011\)](#), [Makela et al. \(2013\)](#), [Fisher et al. \(2015\)](#) and [Tesema et al. \(2017\)](#) have studied quiet-time thermospheric winds over the equatorial Brazilian and African sector respectively. They found similar zonal wind velocities but also lower than those reported over the Peruvian sector. They suggested the differences might correspond to differences on the ion drag due to differences on the plasma density on each location among other causes (e.g., [Martinis et al., 2001](#); [Meriwether et al., 2016](#)).

[Biondi et al. \(1988\)](#) compared zonal drifts from the Jicamarca Incoherent Scatter Radar (ISR) and zonal winds from the Arequipa FPI. They found a better agreement between both components for the late night hours and attributed their better correlation to the decrease of the electron density and the consequent decreasing shorting effect of the E-region and decoupling of the F-region to lower altitudes which allows the plasma to drift with the thermosphere. Similar agreements were obtained by [Fejer et al. \(1985\)](#) when comparing zonal drifts and wind velocities from the Dynamics Explorer-2, or DE-2. Different Satellite missions have been deployed to study longitudinal dependence of the thermospheric winds for different seasons (e.g., [Emmert et al., 2001](#); [Häusler & Lühr, 2011](#); [Wu et al., 1994](#); [Xiong et al., 2016](#)).

The most widely used empirical model is the Horizontal Wind Model (HWM) which derived the global climatological thermospheric wind circulation from different ground- and space-based observations. It was first introduced as such by [Hedin et al. \(1988\)](#) and have undergone different updates since then ([Hedin et al., 1991, 1996](#)). [Drob et al. \(2008\)](#) presented the version HWM07 which included, for the first time, a separate empirical wind component corresponding to the disturbances generated under geomagnetically active conditions. It is called Disturbance Wind Model (DWM) and we will describe it later in more detail. And so, the HWM07 provides spatial, temporal, seasonal and geomagnetic activity dependent thermospheric wind predictions. [Drob et al. \(2015\)](#) presented the last update

of this mode, which only updated its quiet-time component. It is generally called HWM14 and includes observations from Jicamarca and Nasca FPIs. Figure 2.3 shows a comparison of the equatorial thermospheric winds between quiet-time averages Arequipa FPI and predictions from HWM07 and HWM14 evaluated at the same magnetic latitude.

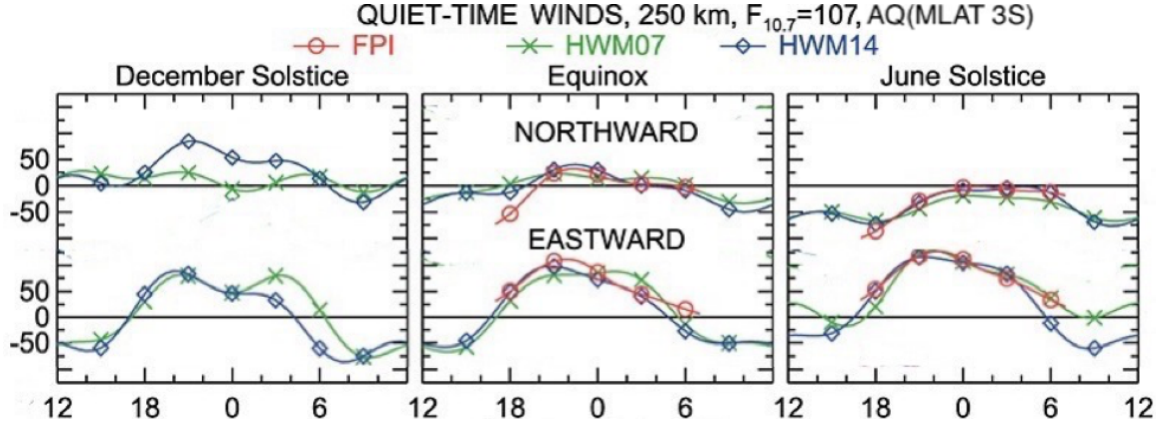


Figure. 2.3: Seasonal comparison of the (bottom) zonal and (top) meridional equatorial thermospheric wind for geomagnetically quiet ( $K_p < 3$ ) and moderate low solar flux conditions for the Arequipa FPI, and predictions from HWM07 and HWM14 (Adapted from [Drob et al., 2015](#)).

### 2.2.2 Disturbance Thermospheric Winds

Global scale variations are observed during periods of strong magnetic activity, called geomagnetic storms, caused by solar-related phenomena like Coronal Mass Ejections among others that deposit energy into the high-latitude ionosphere through different magnetospheric processes (e.g., [Gonzalez et al., 1994](#)). The effects of these large-scale variations can strongly affect the global economy and our lifestyle ([Oughton et al., 2017](#)). However, despite the engineering challenges to overcome this threat, there are great physics questions on how this phenomena affects the near-Earth's atmosphere.

Under strong geomagnetic activity, changes on the high latitude electrical currents and precipitation of charged particles play an important role on driving different global distur-

bances that affect the earth's upper atmosphere at different time scales. The main sources of these disturbances are the solar-wind/magnetospheric and the ionospheric disturbance dynamos. On this dissertation we will focus on the later dynamo which is longer lived and originates from energy depositions at high latitudes, mostly through Joule heating.

Figure 2.4 shows a simplified sketch diagram of the wind dynamo following energy depositions at high latitudes. The energy deposited at the poles by current enhancements or particle precipitation heats up the thermosphere causing global increments on the thermospheric temperature and crucial changes on the regular thermospheric wind circulation. Heated regions of polar thermospheric air parcels upwardly expand and create horizontal pressure gradients which cause the air to flow outward and away from the heating source. This motion distributes the heat globally and creates gravity waves of different spatial scales. Some of them are short lived waves and are dissipated locally while others superpose generating a surge-like bulge that propagates equatorward as travelling atmospheric disturbances, or TADs, creating a meridional wind circulation. They effectively transfer energy from high to low latitude regions. Other global disturbances caused by these heated regions include global density variations and also the onset of the disturbance dynamo electric fields that we will describe in detail later.

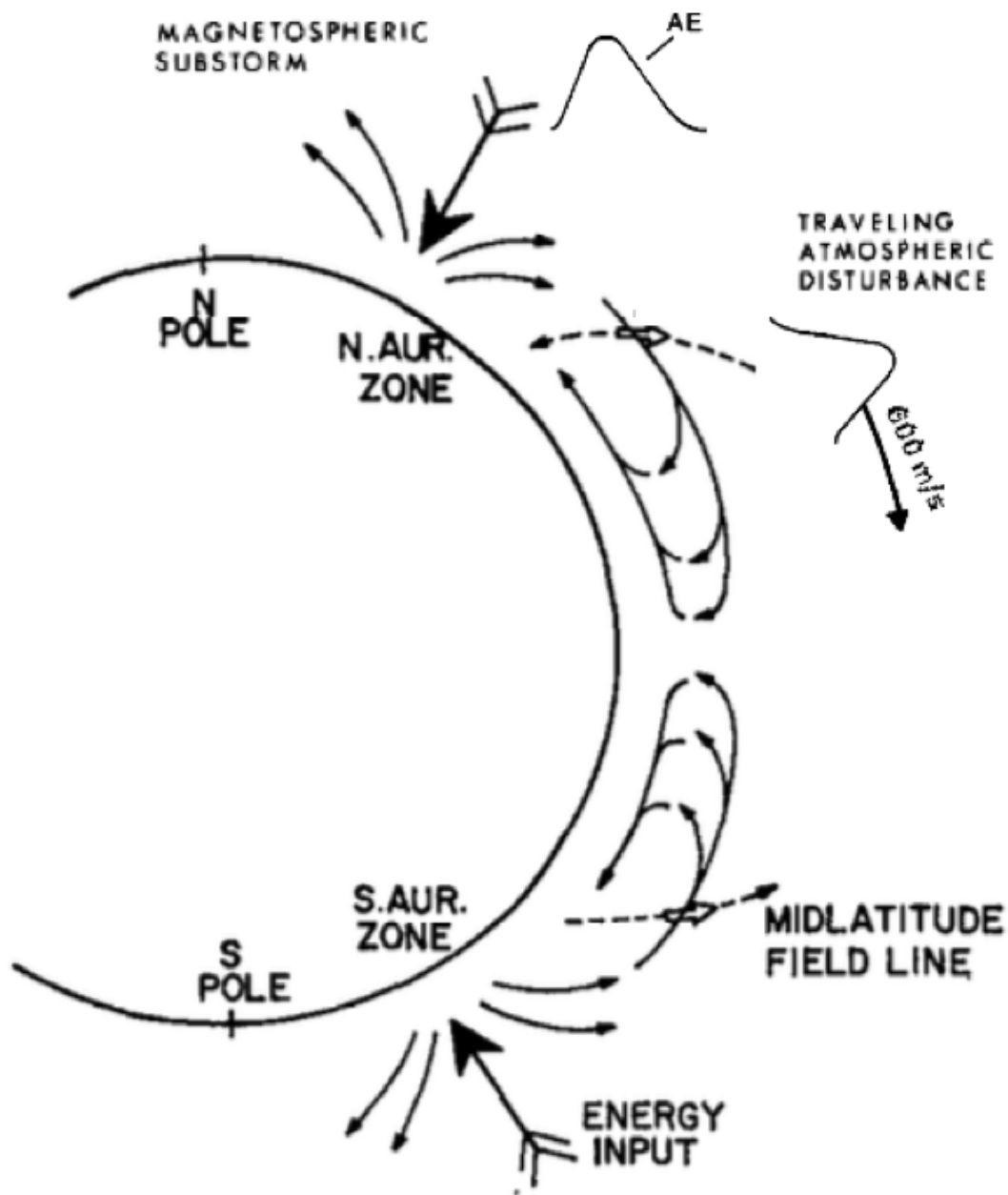


Figure. 2.4: Sketch diagram of the wind dynamo on both poles during a geomagnetic storm. as observed from an increment of the Auroral Electrojet index, AE, on both poles. traveling atmospheric disturbances transfer energy from higher to lower latitudes causing global changes on the wind circulation and temperature among other changes due to thermosphere-ionosphere coupling. (Adapted from [Rishbeth \(1975\)](#) and [Prölss \(1993\)](#)).

[Richmond and Matsushita \(1975\)](#) first pointed out that large global wind perturbations extend down from high to equatorial latitudes due to an increment of auroral currents during geomagnetic storms. [Richmond \(1978, 1979a, 1979b\)](#) studied the relative changes in wave energy due to production, transport and dissipation. They showed that low-frequency and high-velocity waves are least affected by dissipative processes in traveling towards mid and low latitudes over large distances. Moreover, wave energy reaching mid and low latitudes are independent of the dimensions or time scales of the source but mainly on the total heat input. Joule heating dominates the production of observable TADs at low latitudes. Equatorward wind surges have velocities of about 750 m/s and reach lower latitudes in about 4 to 5 hours and later propagates into the opposite hemisphere. Other recent studies have obtained similar results (e.g., [Emery et al., 1999](#); [Fuller-Rowell, Codrescu, et al., 2013](#); [Fuller-Rowell, Richmond, & Maruyama, 2013](#)).

Equatorward moving air parcels develop a westward motion in the frame of a rotating Earth to conserve angular momentum due to the Coriolis force acting over the disturbance winds traveling equatorward. This building effect of westward disturbance winds is important to understand the dissipation of the TAD and possible saturation. It has been postulated by [Fuller-Rowell et al. \(1994\)](#) that the meridional circulation is regulated by the conservation of angular momentum effect over the induced westward winds which in turn builds up a poleward wind that limits the meridional circulation and also the westward winds. Other factors like heat conductivity, viscosity and ion drag are also important role on the dissipation and duration of the disturbance wind circulation. Joule dissipation plays an important role on limiting the westward circulation and on the effective energy dissipation at lower latitudes (e.g., [Fuller-Rowell et al., 1996](#); [Richmond, 1979a](#); [Richmond & Matsushita, 1975](#)).

Figure 2.5 shows the global disturbance winds obtained from Upper Atmosphere Research Satellite (UARS) Wind Imaging Interferometer (WINDII) measurements for a geomagnetic activity level of  $K_p=4$ . It shows the equatorward and westward motions of the thermospheric disturbances developing at low latitudes.

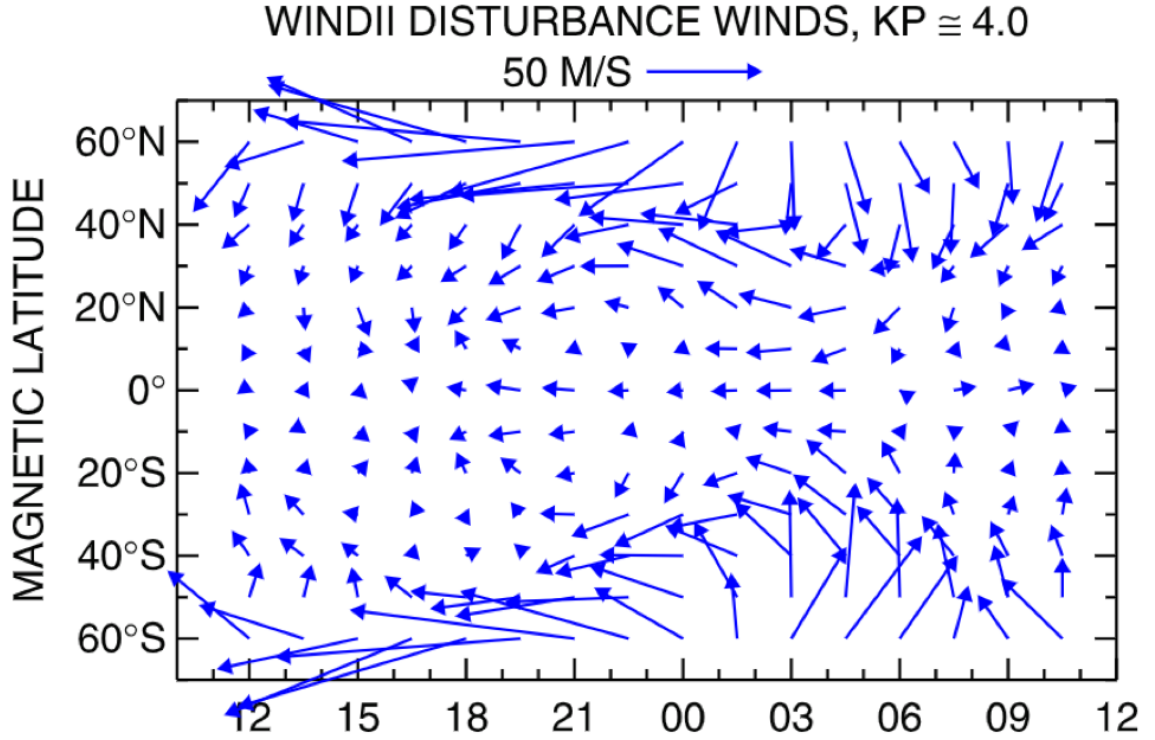


Figure. 2.5: Horizontal disturbance winds for an average  $K_p=4$  from WINDII observations (Adapted from [Emmert et al., 2004](#)).

#### 2.2.2.1 Equatorial Disturbance Winds

At equatorial latitudes, most of the storm-time climatological thermospheric disturbance wind studies have used longitudinal averaged observations by the Wind Imaging Interferometer (WINDII) from the Upper Atmosphere Research Satellite (UARS) (e.g., [Emmert et al., 2001, 2002, 2004](#); [Fejer et al., 2000](#)). They found that geomagnetic effects over the equatorial thermospheric winds are stronger in the zonal component. Figure 2.6 shows the low latitude and equatorial average disturbance winds from WINDII observations for three increasing geomagnetic activity levels. The equatorial zonal disturbance winds are stronger and westward at night and small and eastward in the morning. They increase with increasing geomagnetic activity and are strongest around 03 LT. They also found disturbance winds increase equatorward for increasing solar flux.

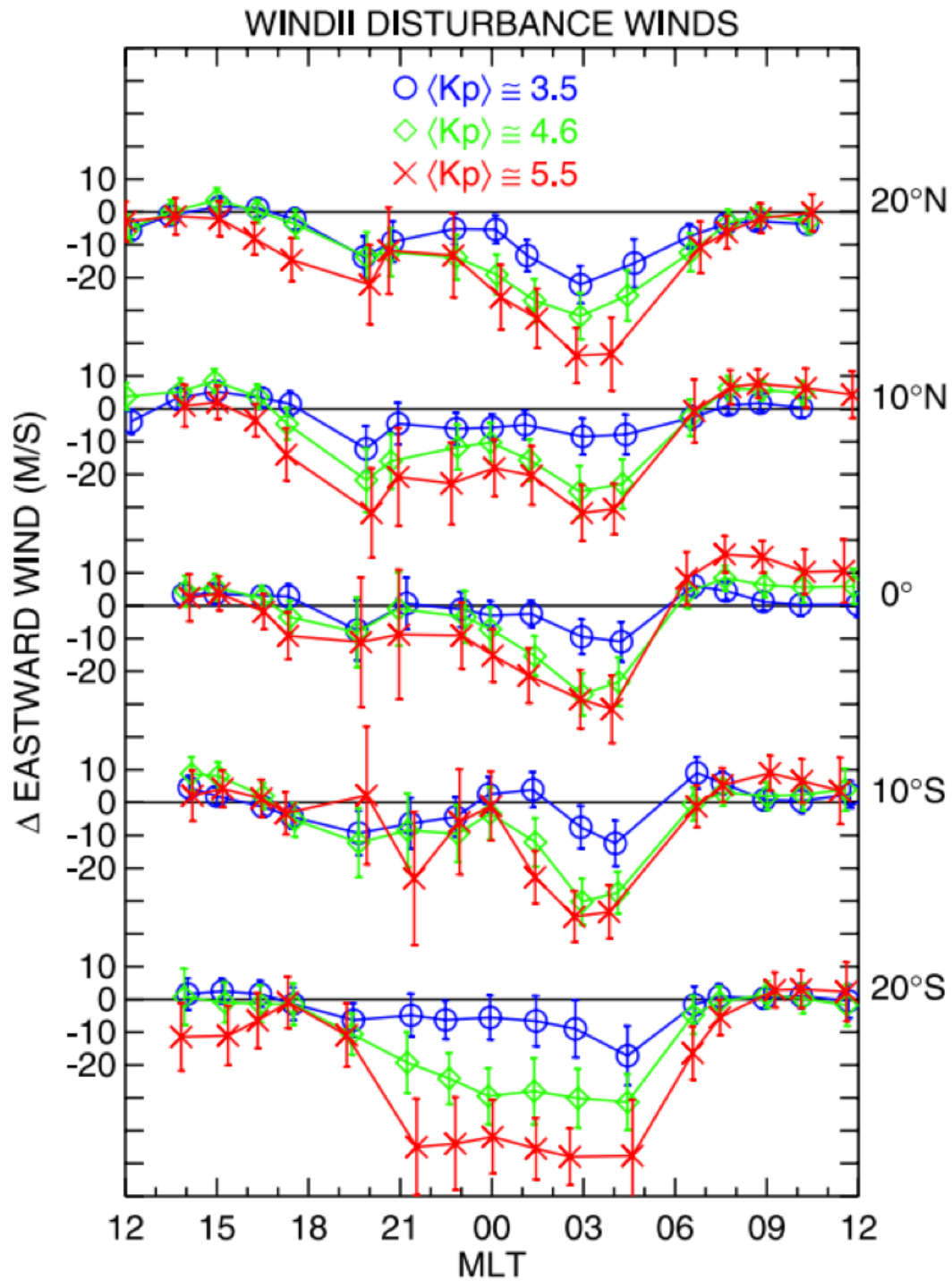


Figure. 2.6: Average disturbance winds as function of magnetic local time (MLT) for three increasing geomagnetic activity levels and for different magnetic latitudes (After Emmert et al., 2004).

Emmert et al. (2008) used UARS WINDII, Dynamic Explorer (DE-2) Wind and Temperature Spectrometer (WATS) and seven FPIs to derive and present the Disturbance Wind Model (DWM07). The DWM07 provides spatial, temporal and geomagnetic activity dependent empirical predictions of disturbance winds. It uses the Kp index at the time of the observation to parametrize the geomagnetic activity level.

Figure 2.7 shows a comparison of the zonal disturbances from DWM07 predictions and averages for Arequipa (magnetic latitude  $\sim 4^\circ$  S) at specific magnetic local times as a function of Kp presented by Emmert et al. (2008). The Arequipa FPI nighttime average disturbances are westward with strongest magnitude around midnight of about 25 m/s for Kp=8, DE-2 and WINDII averages showed stronger disturbances around 03 LT reaching about 50 m/s for Kp=9. It also highlights the strong linear Kp dependence of the zonal disturbances.

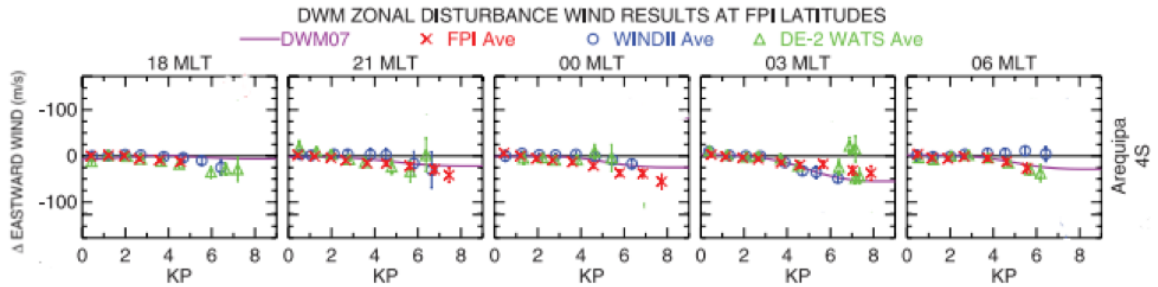


Figure. 2.7: Average zonal disturbance winds from Arequipa FPI data, UARS/WINDII data, and DE 2/WATS data as a function of Kp. Error bars denote the standard errors of the mean. (Adapted from Emmert et al., 2008)

More recently, Xiong et al. (2015, 2016) used longitudinal averaged equatorial zonal disturbance winds from the Challenging Minisatellite Payload (CHAMP) and Republic of China Satellite-1 (ROCSAT-1) and found overall similar results as previous studies except that they found largest disturbances around midnight for all seasons, except for June solstice where largest are around 03 LT. They also suggested that prompt penetration electric fields, due to sudden changes in the magnetospheric convection (e.g., Fejer, 2011), produce



additional zonal disturbance winds that are westward in the afternoon sector and eastward in the post-midnight sector. These studies observed that disturbances occur about 3-4 hours after the high-latitude energy injections and last about 24 hours or longer, which is consistent with model results presented by [Richmond and Matsushita \(1975\)](#) and [Blanc and Richmond \(1980\)](#).

Few studies have examined the response of low latitude thermospheric winds to large geomagnetic storms. [Emery et al. \(1999\)](#) studied the thermospheric response to the November 1993 storm using TIEGCM along with the Assimilative Mapping of Ionospheric Electrodynamics (AMIE) procedure. They found TAD velocities of about 700 m/s reaching equatorial latitudes in about 4 hours, and that largest equatorial westward disturbances occurred around 22 LT for all longitudes. [Fejer and Emmert \(2003\)](#) studied the recovery phase of the October 1998 storm using observations from WINDII. They found large latitudinal variability on the daytime disturbance winds and that disturbance winds reverse from westward to eastward around 30°. [Earle et al. \(2013\)](#) studied three storms in autumn 2011 using Second-generation, Optimized, Fabry-Perot Doppler Imager (SOFDI) observations ([Gerrard & Meriwether, 2011](#)). They found that the disturbances at equatorial latitudes were observed about 5-7 hrs after the initial perturbations in the interplanetary magnetic field and that they persisted for 20-30 hours.

[Meriwether \(2013\)](#) studied the August 1998 and the October 2000 storms using Arequipa FPI observations. Figure 2.8 shows results for the August storm. He used the geomagnetic indices of Kp and Dst to monitor the magnetic activity levels of the storms, and found a reduction on the eastward winds that lasted for about two nights and poleward winds 24 hours after the onset of the storm.

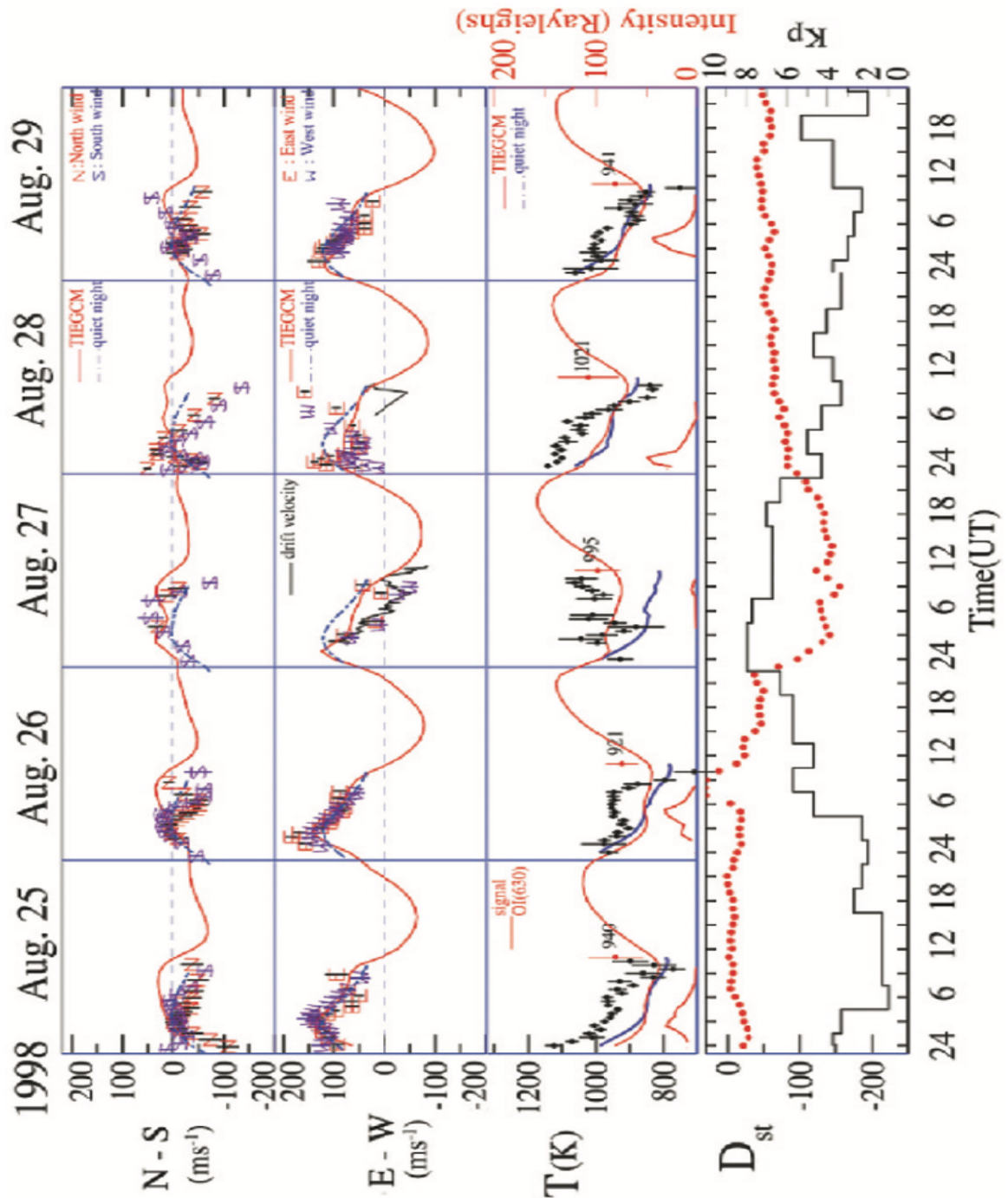


Figure. 2.8: Equatorial thermospheric response for the 25-29 August 1998 storm using Arequipa FPI observations. From top to bottom: Meridional winds, zonal winds, temperatures, and geomagnetic indices Dst (left) and Kp (right). Solid lines and dashed blue lined shows TIEGCM predictions and quiet-time averages. (After Meriwether, 2013)

C. M. Huang et al. (2005), C. M. Huang and Chen (2008) and C. M. Huang (2013) used the National Center for Atmospheric Research Thermosphere Ionosphere Electrodynamics General Circulation Model NCAR/TIEGCM to study the time variations of thermospheric winds in the post storm recovery period. They found that the disturbance winds are stronger around midnight and that they are more persistent in the zonal than in the meridional direction. These disturbances lasted for about 10 days in the zonal direction and for about 8 in the meridional direction for nighttime at equatorial latitudes.

## 2.3 Ionospheric Plasma Drifts

### 2.3.1 Quiet-time Electrodynamics

Neutral wind circulation has important effects on the ionospheric plasma density and dynamics. The neutral winds move the plasma along the magnetic field lines. Thus, an equatorward meridional circulation pushes the plasma both equatorward and upward and have a big effect on the height of ionized layers like the fountain effect (Coley et al., 1990). They also generate polarization electric fields and other related phenomena like the day-night asymmetry of the zonal drifts due to the strong daytime E-region conductivities (Rishbeth, 1971b); and ion drag effects that allows the zonal winds to reach faster velocities at early nighttime due to an upward plasma motion before sunset (Anderson & Roble, 1974).

#### 2.3.1.1 Equatorial Plasma Drifts

Most studies of the equatorial ionospheric electrodynamics used observations of the Jicamarca Incoherent Scatter Radar ( $12^\circ$  S,  $76.9^\circ$  W; magnetic dip  $2^\circ$  N). Fejer, Farley, et al. (1979); Fejer et al. (1985, 1991, 2005) showed the seasonal and solar cycle dependence of the quiet-time F-region vertical and zonal plasma drifts.

Quiet-time equatorial vertical plasma drifts are upward (downward) during the day (night) with an enhancement prior to the evening reversal called pre-reversal enhancement. Figure 2.9 shows the seasonal and solar flux dependence of the equatorial vertical plasma

drifts over Peru. The strongest seasonal and solar flux effects occur around the pre-reversal enhancement period. This has important implications for the development of plasma irregularities (Fejer & Kelley, 1980; Fejer et al., 1999). Various mechanisms were proposed to explain the evening pre-reversal enhancement (e.g., Farley et al., 1986; Kelley, 2009). Scherliess and Fejer (1999) presented the most widely used empirical model of the quiet-time equatorial vertical plasma drifts derived from ground and space-based observations. It provides longitudinal, temporal, seasonal and solar flux dependent equatorial vertical drift predictions. Other empirical models have also been developed for the daytime E-region vertical drifts (e.g., Alken, 2009).

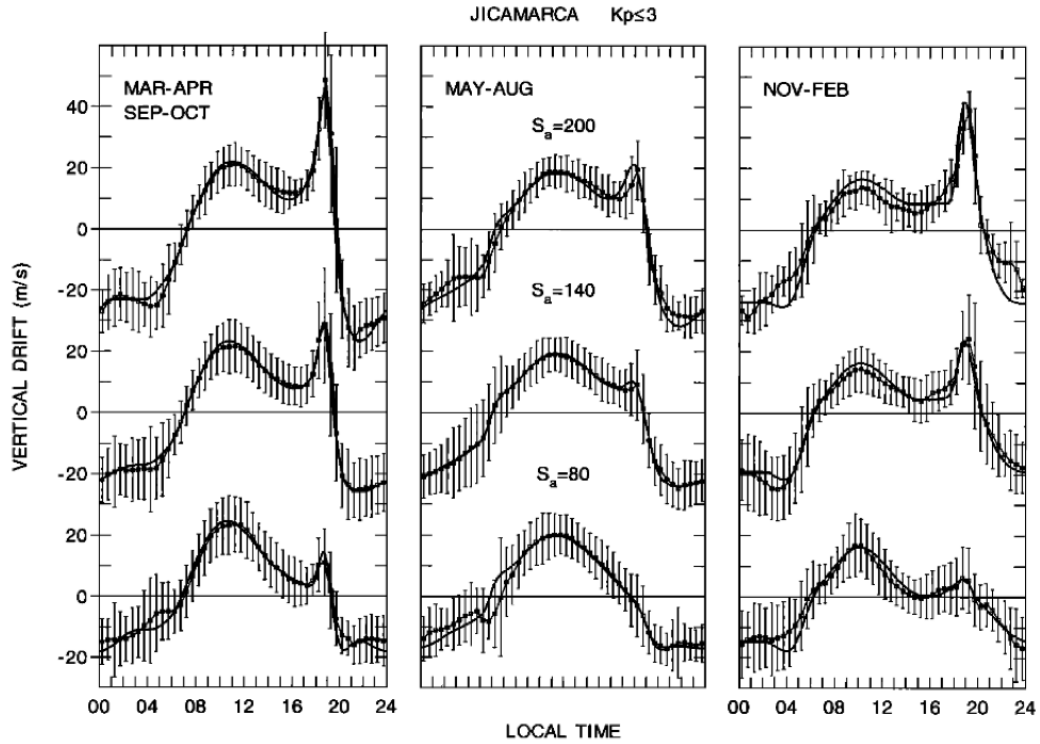


Figure. 2.9: Seasonal and solar flux comparison of the quiet-time vertical plasma drifts using Scherliess-Fejer model and averages from Jicamarca observations for equinox, June solstice and December solstice; and for low, medium and high. Errorbars show the standard deviations. (After Scherliess & Fejer, 1999)

Quiet-time equatorial zonal plasma drifts are eastward (westward) during the night (day). Figure 2.10 shows the dependence of the equatorial quiet-time zonal plasma drifts over Peru in season and solar flux. These drifts also have largest seasonal and solar cycle effects near dusk and early midnight. The large day-night asymmetry on the magnitudes of the zonal drifts is attributed to the strong daytime conductivities in the E-region and to the action of the prereversal enhancement on the nighttime zonal F-region drifts and winds (Kelley, 2009; Richmond, 1995b; Richmond et al., 1992). The ionospheric uplifting around sunset allows stronger zonal winds due to the reduced evening ion drag (Anderson & Roble, 1974), and consequently stronger eastward wind generates electric fields that yield to stronger zonal ion drifts (Rishbeth, 1971b). Fejer et al. (2005) derived the empirical model of the quiet-time equatorial zonal plasma drifts from Jicamarca radar observations. It provides temporal, seasonal and solar flux dependent equatorial zonal drift predictions.

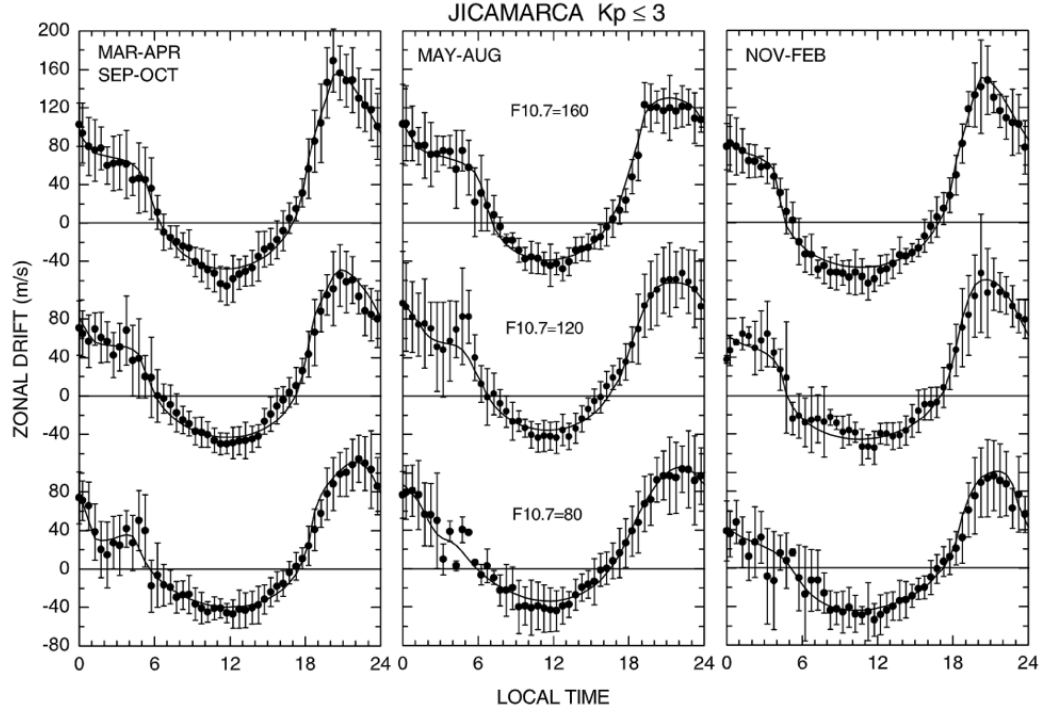


Figure. 2.10: Seasonal and solar flux comparison of the quiet-time zonal plasma drifts using Fejer model and averages from Jicamarca observations for equinox, June solstice and December solstice (After [Fejer et al., 2005](#)).

Figure 2.11 shows in more detail the annual variation of the equatorial zonal plasma drifts for solar minimum and maximum. The peak magnitudes are largest around the equinoxes with slightly stronger drifts in the vernal equinox. The daytime zonal drifts exhibit an apparent annual variation on the noon zonal drifts, which are westward and strongest for autumnal equinox during low solar flux conditions. This variation seems to become biannual for higher solar flux.

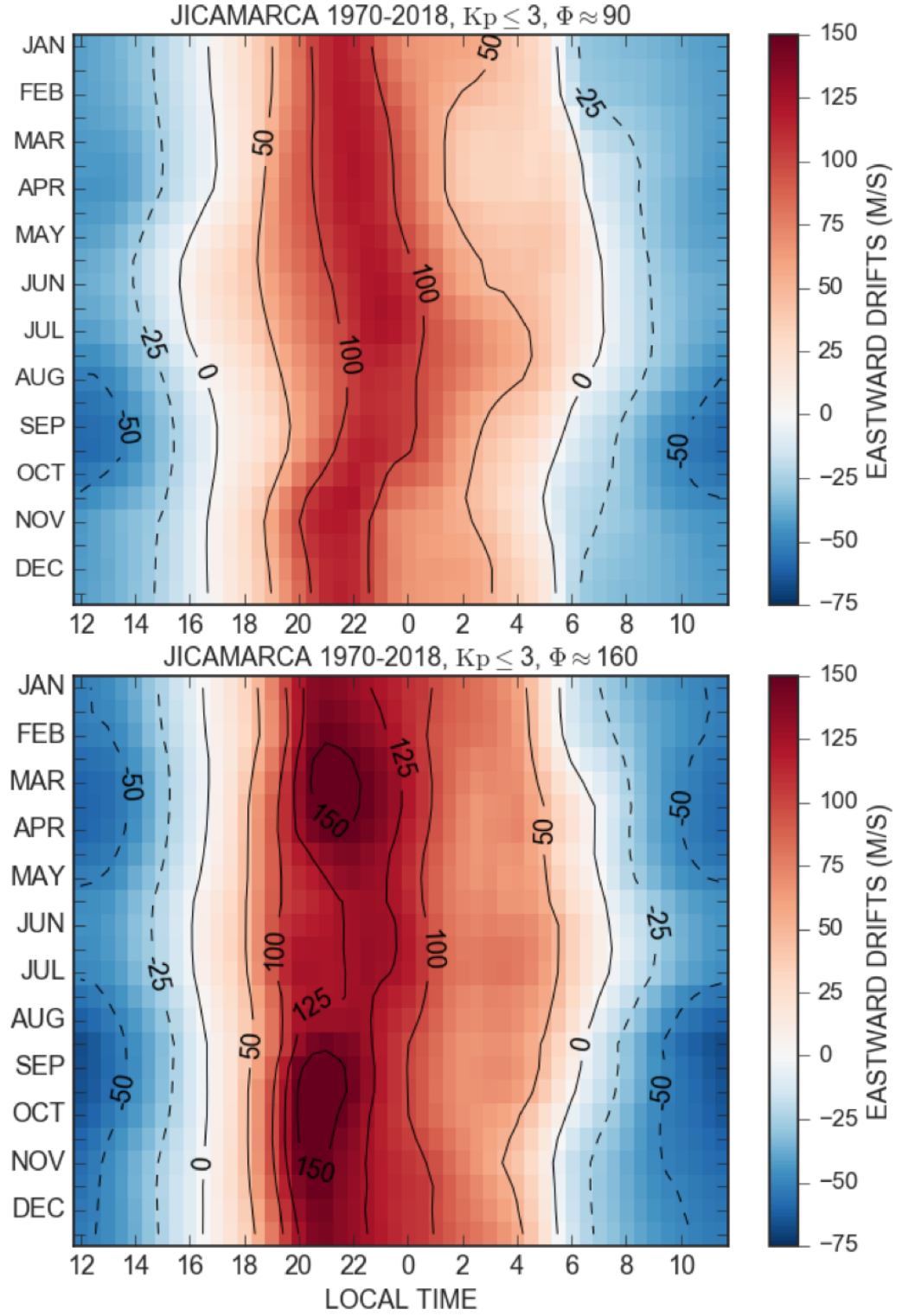


Figure. 2.11: Annual variation of the quiet-time zonal drifts over Jicamarca for (top) solar minimum and (bottom) solar maximum.

Other studies include longitudinal dependence of the quiet-time plasma drifts using observations from different satellite missions ([Jensen, 2007](#); [Fejer et al., 2008a](#); [Stoneback et al., 2011](#); [Fejer et al., 2013](#); [Coley et al., 2014](#)), altitudinal dependence of the plasma drifts using Jicamarca observations ([Fejer et al., 1985](#); [Pingree & Fejer, 1987](#); [Fejer et al., 2014](#); [Hui & Fejer, 2015](#); [Shidler et al., 2019](#); [Shidler & Rodrigues, 2019](#)), day-to-day variability ([Fejer & Scherliess, 2001](#)), on the development of plasma irregularities [Fejer et al. \(1999\)](#), and comparisons with theoretical models ([Liu et al., 2018](#); [Richmond & Maute, 2014](#); [Fang et al., 2014](#); [Rodrigues et al., 2012](#); [Richmond et al., 1992](#); [Fesen et al., 2002](#)) among many others.

### 2.3.2 Storm-time Equatorial Ionospheric Electric Fields

Enhanced geomagnetic activity can drive large perturbation on the global ionospheric electric field with a broad range of temporal and spatial scales (e.g., [Fejer, 1981](#); [Fejer et al., 2017, 2002](#)). The main sources of these disturbances are the solar-wind/magnetospheric and the ionospheric disturbance dynamos ([Fejer et al., 2017](#); [Kikuchi & Hashimoto, 2016](#)). The electric fields of magnetospheric origin can penetrate into the low latitude ionosphere following sudden changes in the high latitude current system ([Fejer & Scherliess, 1997](#)). They are shorter time scale (less than a few hours) disturbances, occur nearly simultaneously from auroral to equatorial latitudes and are called prompt penetration electric fields. The ionospheric disturbance dynamo is a wind-driven electric field with short- and long-lasting effects over the equatorial ionosphere. Its disturbances can arrive at equatorial latitudes in about 1-3 hours and can last up to 48 hours ([Scherliess, 1997](#); [Scherliess & Fejer, 1997](#)).

Figure [2.12](#) shows an example of these disturbances over the equatorial ionosphere during the large storm 8-10 August 1972. The vertical plasma drifts are largely disturbed during two main periods around midnight and in the postmidnight sector on the 9 and 10 of August. The first perturbations occur almost simultaneously following a sharp and large increase on the AE index, and so they are considered to be due to prompt penetration electric fields. The second perturbation is not followed by any considerable change in the magnetic activity at the time of the observations nor even about 12 hours before, and so



they are considered to be most likely due to disturbance dynamo electric fields.

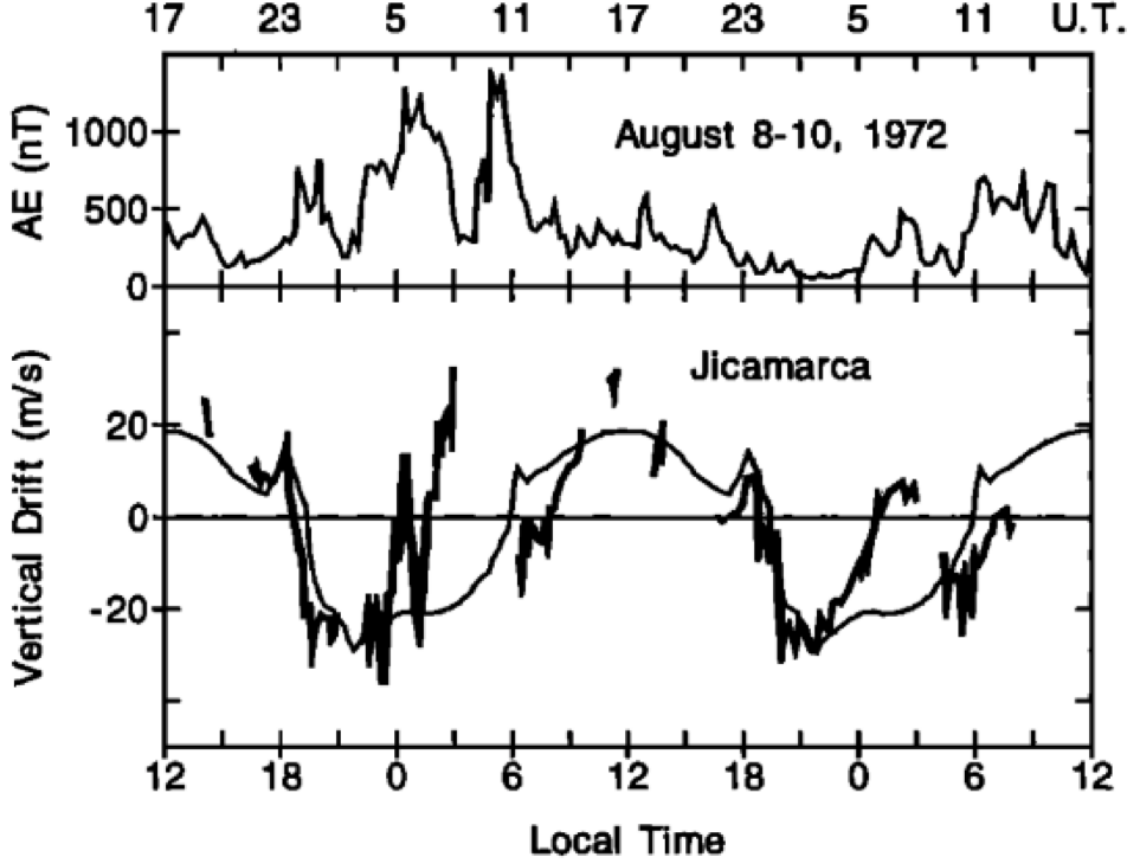


Figure. 2.12: Equatorial vertical plasma drifts for the August 1972 storm. Jicamarca Incoherent Scatter Radar observations and quiet-time vertical plasma drifts (After [Fejer et al. \(1983\)](#) and [Scherliess and Fejer \(1997\)](#)).

### 2.3.2.1 Prompt Penetration Electric Fields

Electric fields of magnetospheric origin can penetrate into the low latitude ionosphere following sudden changes in the high-latitude convection electric field which can be seen as sudden increases/decreases on the AE index ([Fejer & Scherliess, 1995](#)). These large changes occur as a result of an imbalance in the high latitude field aligned currents system due to the solar wind-magnetosphere dynamo ([Sazykin, 2000](#)). The resultant disturbances,

generally called prompt penetration electric fields, are eastward (westward) at day(night) and southward(northward) from midnight to noon (noon to midnight). After decreases in the polar cap potential drop, i.e. sudden AE decrease, these polarities are reversed (Kelley et al., 1979, 2003; Fejer & Scherliess, 1995, 1997; Fejer, Gonzales, et al., 1979; Fejer et al., 2007). They are also short lived and the largest event was observed around dusk for the Nov 2003 storm (Fejer et al., 2007). Empirical models have also been developed using AE index (Fejer & Scherliess, 1997) and also solar wind parameters (Manoj et al., 2008). For different dependencies of these disturbances like solar flux, seasonal and rotation of the polar cap potential the reader might refer to Sazykin (2000).

These disturbances and the disturbance dynamo electric fields can affect the low latitude ionosphere at the same time and their effects can have similar or opposite polarities. However, it is possible to remove the effects from these drifts using the AE index to track and filter out observations following sudden increases or decreases which will represent sudden changes of the high latitude convection electric field (Fejer & Scherliess, 1995, 1997).

### 2.3.2.2 Disturbance Dynamo Electric fields

Storm-time equatorial wind surges and changes on the meridional circulation produce strong changes in the global conductivity and ionospheric electric field. Blanc and Richmond (1980) presented the first theoretical description of the ionospheric disturbance dynamo and showed that storm-time heating at high latitudes can lead to significant disturbances in the thermospheric wind fields and on the global conductivity distribution which generate disturbance ionospheric electric fields and currents.

Figure 2.13 shows a simplified schematic of the ionospheric disturbance dynamo presented by Mazaudier and Venkateswaran (1990). As the equatorward thermospheric wind circulation ( $V_S$ ) takes place, westward motion is developed on the winds ( $V_W$ ) to conserve angular momentum. These winds drive westward drifts that generate equatorward ionospheric Pedersen currents ( $J_P$ ) which are stronger near 150 km where the Pedersen conductivity is high. These currents build up and accumulate positive electric charges at the geomagnetic equator. These charges generate a poleward electric field ( $E_N$ ) which

drives eastward Hall currents ( $J_H$ ) and westward plasma drifts which are maximum at midlatitudes. These currents cannot go through the dusk and dawn terminators due to the large conductivity gradients. Thus, they accumulate electric charges giving rise to the dusk-to-dawn electric field and are deflected to high and low latitudes creating the polar and equatorial vortex. It is important to mention that the equatorial vortex is opposite to the quiet-time current system and so the ionospheric disturbance dynamo has a counter effect at equatorial latitudes.

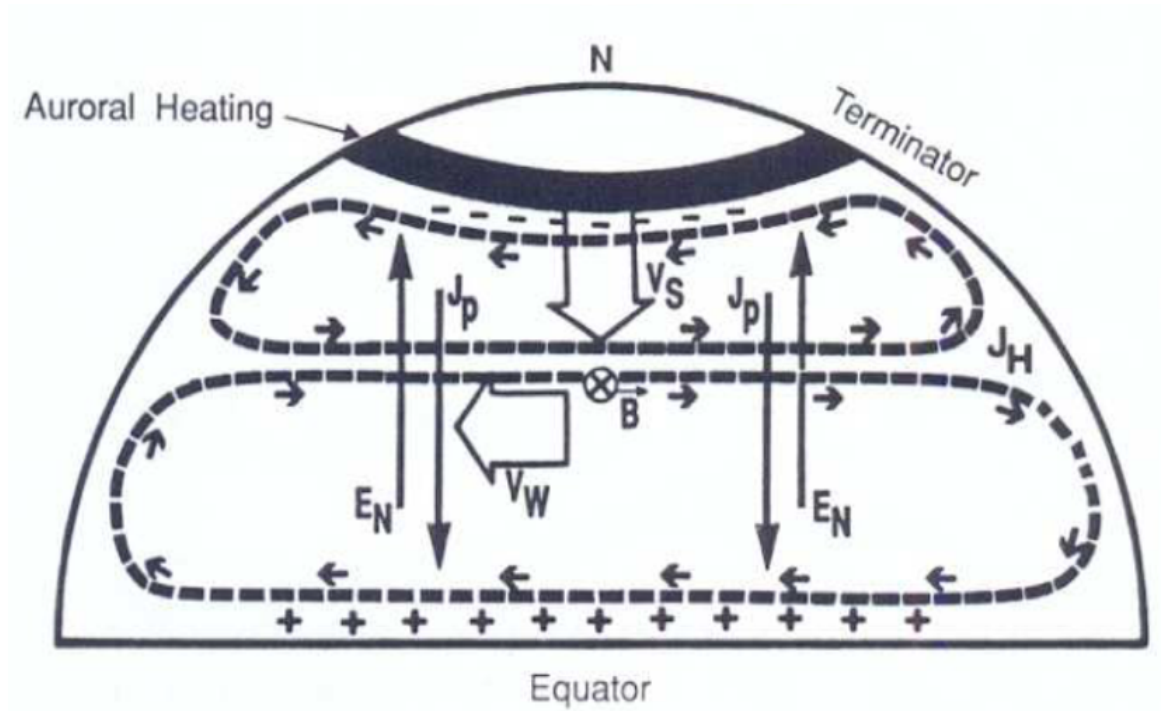


Figure. 2.13: Sketch diagram of the Ionospheric Disturbance dynamo Model. It shows that equatorward wind circulation at high latitudes ultimately generates an electric field opposite to the quiet-time electric field at equatorial latitudes. Detailed description of this figure on the text above (After [Mazaudier & Venkateswaran, 1990](#)).

At equatorial latitudes, [Fejer et al. \(1983\)](#) used initially Jicamarca Incoherent Scatter vertical drifts observations and showed that the equatorial vertical disturbance dynamo

drifts were opposite to the normal quiet patterns in agreement with the Blanc-Richmond model but also noted that, for most storms, there is an inherent difficulty to separate competing effects from the equatorial disturbance dynamo and prompt penetration electric fields (e.g., [Fejer & Scherliess, 1997](#); [Wolf, 1995](#)). [Fejer and Scherliess \(1995\)](#) used a binning technique to successfully separate these competing effects using the auroral electrojet index, AE index, as a proxy for this goal. The derived disturbance dynamo disturbances were used to determine the time delays between geomagnetic activity enhancements, as indicated by AE indices, and the equatorial electrodynamic responses.

[Scherliess and Fejer \(1997\)](#) developed the first empirical model of equatorial disturbance dynamo vertical drifts using very extensive Jicamarca observations and AE indices. They showed that the disturbance dynamo vertical drifts are downward with small values during the day, and upward at night with largest magnitudes near sunrise. The time delays between the high latitude current enhancements and the corresponding equatorial disturbance dynamo disturbances are about 1-12 hours and 12-28 hours.

Figure [2.14](#) shows the equatorial disturbance dynamo vertical drifts from the Scherliess-Fejer model and data averages following steady 9-hours of enhanced geomagnetic activity. They are upward around and after midnight with strongest magnitudes before sunset, and downward during early morning and also around dusk. This response is associated with fast traveling atmospheric disturbances ([Fejer & Scherliess, 1997](#); [Fejer et al., 2017](#)) but possibly to other processes like fossil winds ([Fejer et al., 1990](#); [Scherliess, 1997](#); [Scherliess & Fejer, 1997](#)). The long-term disturbances are associated with changes in the thermospheric circulation and ionospheric composition ([Fuller-Rowell et al., 1994, 1996, 2002](#)) and, probably, also to electric fields resulting from the decay of the storm-time ring current in the recovery phase of a magnetic storm ([Scherliess, 1997](#); [Scherliess & Fejer, 1997](#)). They are largest under short-term geomagnetically quiet conditions.

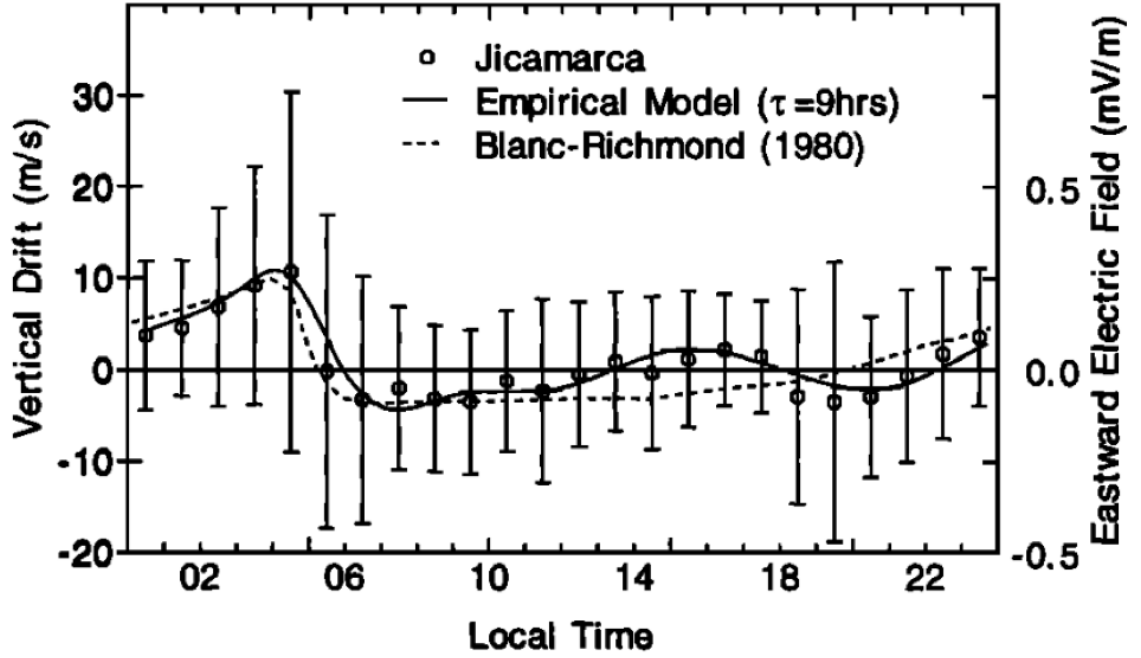


Figure. 2.14: Local time variation of the equatorial disturbance dynamo vertical drift following 9-hours of high geomagnetic activity conditions (After [Scherliess & Fejer, 1997](#)).

Other studies used satellite observations from ROCSAT-1 to study seasonal and solar flux dependence of longitudinal dependent equatorial disturbance dynamo drifts. [Jensen \(2007\)](#) showed that downward disturbance drift around dusk increase strongly from moderate to high solar flux. [Fejer et al. \(2008b\)](#) used observations of an altitude of about 600 km and found that the evening downward dynamo drifts are largest during equinox and smallest during June solstice while the nighttime upward drifts were largest during December solstice. [Xiong et al. \(2016\)](#) used also CHAMP observations and found disturbance dynamo effect at equatorial latitudes after 4.5 hours in the postmidnight sector which gradually decrease after 24 hours.

On the other hand, [Fejer and Scherliess \(1997\)](#); [Fejer et al. \(2005\)](#) used Jicamarca observations to study geomagnetic effects over the zonal plasma drifts. They found that nighttime (daytime) zonal drifts are eastward (westward). They showed strongest zonal

disturbance drifts around midnight and during equinox. Figure 2.15 shows Fejer model predictions of the equatorial disturbance zonal drift for low ( $F_{10.7}=90$ ) and high ( $F_{10.7}=180$ ) solar flux conditions and different seasons. They also used a similar binning technique in terms of the Kp index and found that long terms effects are strongest around 03 LT and short terms effects are strongest around midnight.

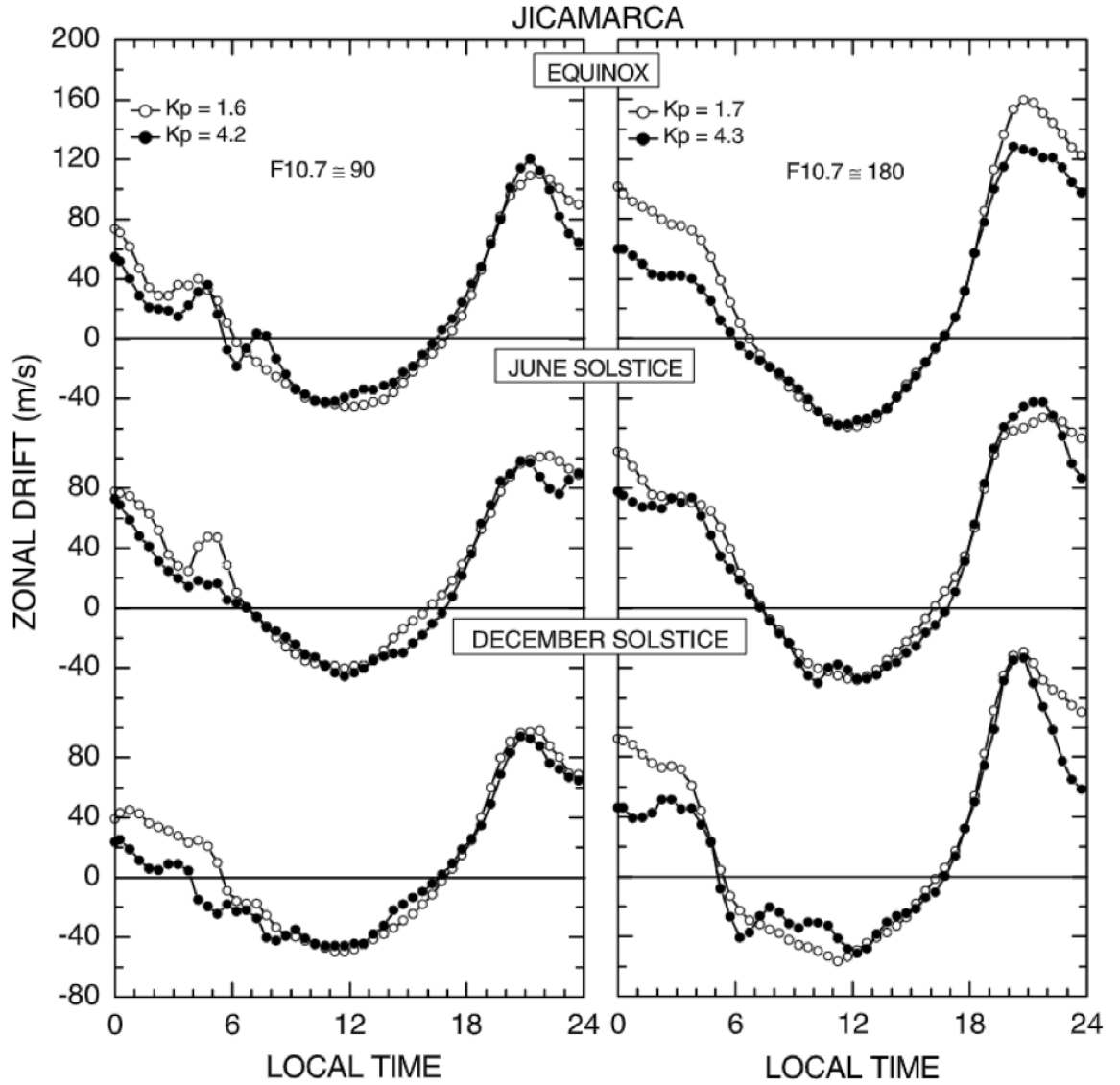


Figure. 2.15: Fejer model predictions (solid) of the equatorial disturbance zonal drift for low (right) and high (left) solar flux conditions and different seasons (After [Fejer et al., 2005](#)).

[Fejer and Emmert \(2003\)](#) used Jicamarca and Arecibo vertical plasma drifts and UARS wind measurements for the first detailed study of low latitude disturbance dynamo effects during the recovery of the 19–21 October 1998 major geomagnetic storm. These observations showed large latitudinal variability of the disturbance drifts, and reported that the amplitudes were initially much larger than the expected climatological values. [R. Zhang, Liu, Le, and Chen \(2017\)](#) used Communication/Navigation Outage Forecasting System (C/NOFS) and ROCSAT-1 observations and suggested that strong disturbance winds can corotate to later local time and drive disturbance dynamo drifts to extend from the nightside to the dayside.

[C. M. Huang et al. \(2005\)](#), [C. M. Huang and Chen \(2008\)](#) and [C. M. Huang \(2013\)](#) used the NCAR/TIEGCM simulations to study longitudinal, seasonal and solar cycle dependence of the equatorial disturbance dynamo vertical plasma drifts. These simulations reproduced the observed decrease of the magnitudes of the disturbance dynamo drifts with decreasing solar flux, the occurrence of larger magnitudes during equinox than during June solstice, and the stronger disturbance effects near dusk close to the Indian sector than over Jicamarca.

## CHAPTER 3

### DATA AND METHODOLOGY

In this chapter we introduce the instrumentation and data analysis techniques used in our studies of thermospheric neutral winds and ionospheric plasma drifts at Jicamarca. The main emphasis is on the instrumentation and analysis of thermospheric neutral winds since the methodology for probing plasma drifts over Peru has been described in detail in several publications (e.g., [Farley et al., 1981](#); [Fejer et al., 2014](#); [Hysell et al., 2017](#); [Pingree, 1990](#); [Pingree & Fejer, 1987](#); [Woodman, 1970, 1971](#); [Woodman & Hagfors, 1969](#)).

The thermospheric winds are routinely observed by a recently deployed network of Fabry Perot Interferometers over the central region of Peru. These instruments probe the thermospheric winds by measuring the Doppler shift of the oxygen 630 nm line. We will describe initially the generation mechanism of the oxygen 630 nm emission line, the instrumentation of the FPI network, the estimated wind field from the line-of-sight observations, and, finally, the statistics of the resultant wind database.

One of the most powerful and important instruments on space physics and aeronomy is the Jicamarca Incoherent Scatter Radar. It provides with the most extensive and accurate database of plasma drifts and electric field observations in the field. We will briefly describe the Jicamarca Incoherent Scatter Radar and the statistics of the available observations gathered since 1968.

### 3.1 Fabry-Perot Interferometers

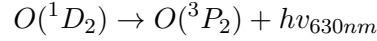
#### 3.1.1 Oxygen line emission

Fabry-Perot Interferometers are versatile and powerful spectroscopic instruments widely used in aeronomy to remotely sense and resolve Doppler frequency and broadening of the spectrum of naturally faint emissions occurring at the upper atmosphere ([Hernandez, 1988](#)).



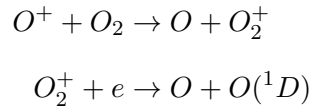
These optical emissions are the result of the de-excitation of atmospheric species by spontaneous emission or by losing energy through collisions. They are generally called airglow when the original source of excitation is the solar radiation in the extreme ultra-violet violet radiation range (Schunk & Nagy, 2009).

In the nighttime thermosphere, the volume emission rate of the 630 nm glow is dominant about 250 km. It is emitted when an excited  $O(^1D_2)$  atom decays to its ground state  $O(^3P_2)$ . This is summarized on the following reaction



Other emissions are also possible for different transitions. For example, a 636.4 nm photon is emitted if excited oxygen atom decays into its  $O(^3P_1)$  ground state or a 557.7 nm emission if the transition goes from the  $O(^1S_0)$  to the  $O(^1D_2)$  energy levels. However, the intensities of these emissions are about three times weaker (Rishbeth & Garriot, 1969). The radiative lifetime of the  $O(^1D)$  energy level is much longer ( $\sim 110$  sec) than at other energy levels and its collision time with F-region particles ( $\sim 0.3$  sec) settles this line as a suitable proxy to observe wind and temperatures for the thermosphere (Schunk & Nagy, 2009).

The dominant reaction responsible for the production of the excited atoms is generally explained by a two-step process. A molecular oxygen is positively charged by charge exchange with oxygen ions and later dissociated into an excited and a ground-energy oxygen atom when interacts with free electrons by dissociative recombination. These reactions are summarized in



The last step can also produce oxygen on different energy levels than  $O(^1D)$  and eventually produce other wavelengths however they are too dim in respect to the 630 nm emission

line (Abreu et al., 1982; Rishbeth & Garriot, 1969).

Another aspect to take into account is whether the emitted 630 nm photons are a good proxy for the ambient neutral atmosphere. After the dissociative recombination, the excited oxygen atoms,  $O^1(D)$ , need to remain excited long enough to reach thermal equilibrium with the ambient neutral background, i.e. thermalize, through collisions before they relax to ground state. This might translate into having populations of oxygen atoms with different velocities. However, any non-thermal effect would be reflected only on temperature estimations and will be stronger for higher altitudes since it is collision dependent (Hernandez, 1971; Sipler & Biondi, 2003; Yee, 1988). Thus, it is generally assumed that at our altitudes of interest, 200 km to 300 km, oxygen atoms have reached thermalization at night time being a good proxy for the thermospheric winds.

Figure 3.1 shows the expected oxygen line spectrum to be observed by the Fabry-Perot Interferometers where the Doppler shift,  $\Delta\lambda$ , and broadening,  $\sigma_T$ , are related to the bulk velocity vector of the oxygen  $O^1(D)$  population (already thermalized),  $v_b$ , and to the temperature,  $T$ , within the airglow layer,  $k$ ,  $m$  and  $c$  are the Boltzmann constant, atomic mass and speed of light respectively.

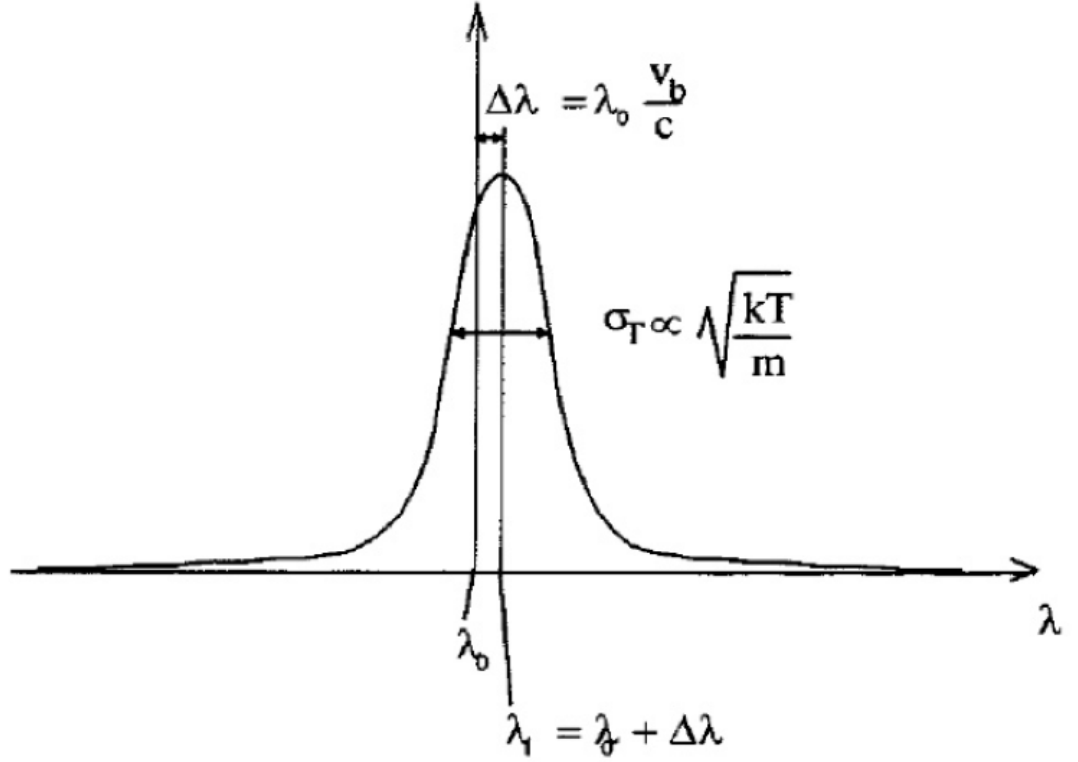


Figure. 3.1: Oxygen line emission following a Gaussian distribution with Doppler shift,  $\Delta\lambda$ , and broadening,  $\sigma_T$ .

### 3.1.2 Optical principle and instrumental modeling

Fabry-Perot Interferometers use the principle of multiple-beam interference to relate the wavelength of the incoming emission to the angular displacement of the resultant interferometric pattern. Figure 3.2 shows a simple diagram of the optical path of an incoming airglow emission going through the basic optical elements of a Fabry-Perot Interferometer instruments used on our study. It uses two semi reflective parallel mirrors, called etalons, to divide, or beam-split, the incident wave and to produce stationary coherent waves. They are later superimposed using an objective lens to generate an interferometric ring pattern.

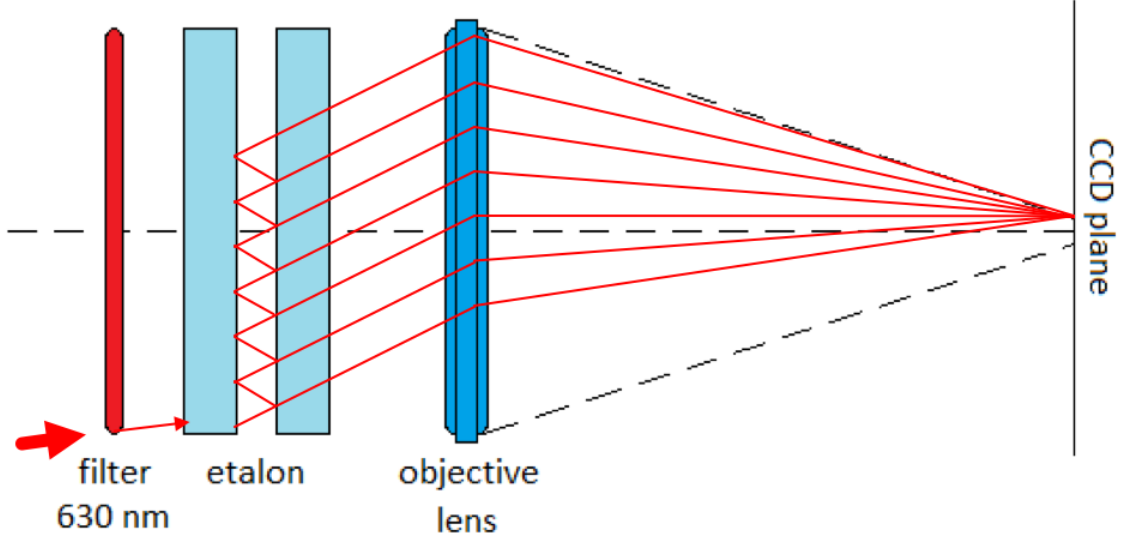


Figure. 3.2: Diagram showing the optical path of an incoming oxygen line emission going through the basic elements of a Fabry-Perot Interferometer.

For an ideal situation, this constructive interference can be analyzed as a linearly polarized electromagnetic wave going through a slab with an incidence angle  $\theta$  and an index of refraction  $n$ . This system is analyzed using the Snell's Law and the continuity boundary conditions of the tangential components of the electric and magnetic fields before and after the interfaces to get the intensity of the transmitted radiation. This is generally referred as the Airy function,  $A$ , and is given by,

$$A(\theta, \lambda) = \frac{I}{1 + \frac{4R}{(1-R)^2} \sin^2 \left( \frac{2\pi nd}{\lambda} \cos \theta \right)} \quad (3.1)$$

where  $R$ ,  $d$ ,  $\lambda$ ,  $I$  are the reflectivity of the etalon plates, etalon separation, wavelength and the intensity amplitude. The amplitude, which is one for the ideal situation, will be later modeled as an intensity quadratic fall off function to account for the radially decreasing action of the optical transmission (Harding et al., 2014; Meriwether et al., 2008).

According to 3.1, the constructive interference can be achieved by varying  $n$ ,  $d$  or  $\theta$  and they are usually referred as pressure, mechanical and spatial spectral scanning modes.

Our instruments use the spatial scanning mode and the resultant interferometric pattern are bi-dimensional concentric rings with a nonlinear displacement between them (Makela et al., 2011; Meriwether et al., 2008). Other scanning modes result into a onedimensional spectrum. The pressure scanning mode was used for several years at Arequipa (16°28' S, 71°30' W, magnetic latitude  $\sim 6.7^\circ$  S) (Biondi et al., 1999) until it was upgraded to use spatial scanning in 2005 (Meriwether et al., 2008). The mechanical scanning is being used at Huancayo (12.1° S, 75.3° W, magnetic latitude  $\sim 1.9^\circ$  S) on two of their triple cascade etalons to filter out the solar background continuum (Gerrard & Meriwether, 2011). A combination of pressure and spatial scanning modes are used to observe several points on the sky at once (Conde & Smith, 1995).

The response of the Airy function to the airglow source has been generally expressed as different convolutional operations between the source function and a Doppler-shifted Gaussian profile. The Airy function was also previously convolved with other functions to represent several optical aberrations (Hays & Roble, 1971). Other approaches also used Doppler-broadened Lorentzian profiles (Hernandez, 1966). More recently, Harding et al. (2014) modeled this response,  $S$ , as a Fredholm integral equation of the first kind between a modified Airy function,  $\tilde{A}$ , and the Gaussian spectrum of the oxygen line source,  $Y$ .

$$S(r) = \int_{-\infty}^{\infty} \tilde{A}(r, \lambda) Y(\lambda) d\lambda + B$$

where,  $r$  is the radial distance from the center of the bi-dimensional pattern and  $B$  is the CCD bias. The modified Airy function includes an intensity quadratic fall off factor and is blurred by a point-spread function to account for different deviations from the ideal Airy function (Harding et al., 2014). The oxygen line spectrum is modeled as a gaussian source. It is expressed as

$$Y(\lambda) = Y_B + Y_I \exp \left( -\frac{1}{2} \left( \frac{\lambda - \lambda_{LOS}}{\sigma_T} \right)^2 \right)$$

where  $Y_B$ ,  $Y_I$ ,  $\sigma_T$ ,  $\lambda_{LOS}$  are the background of the line emission, the intensity of the line

emission, the Doppler broadening and the Doppler shifted wavelength. The Doppler shifted wavelength is shifted in reference to the nominal frequency 630 nm and it is related to the line-of-sight velocity through the doppler shift equation.

The resultant bi-dimensional image is later collapsed into an onedimensional profile by annular summing. This transformation helps to approximate the non-linear spacing of the bidimensional interferometric pattern into a quasi-linear one-dimensional multi-fringe profile. It defines nonoverlapping annular elements, called annular channels, following a quadratic relation due to the small angle approximation applied to 3.1 (Coakley et al., 1996). For our study we use 500 annular channels (Makela et al., 2011; Meriwether et al., 2008).

Similar to previous techniques (Conde, 2002; Makela et al., 2011; Meriwether et al., 2008), we use a two-step fitting process procedure. We first estimate for instrumental parameters of the modified Airy function using images from a HeNe 632.8 nm laser. This way, since the laser has a known spectrum, their images are used to get estimates of parameters such like etalon spacing gap, reflectivity of the etalon, optical magnification constant among others. Thus, laser images are useful for calibration purposes and to monitor drift of the instrumental parameters along the night. These parameters are later used to estimate airglow parameters such like the Doppler frequency shift and broadening.

Figure 3.3 shows an example of this analysis for one interferometric image measured by Nasca FPI (14°58' S, 74°53' W, magnetic latitude  $\sim 5^\circ$  S). The bi-dimensional interferometric pattern, shown in the middle, was collapsed into an onedimensional profile using 500 annular channels as it is shown in the top panel. The best fit for the airglow source parameters is overplotted on the same box and the residual differences are shown on the bottom. This analysis was used to analyze the images from the FPIs deployed in the central region of Peru.

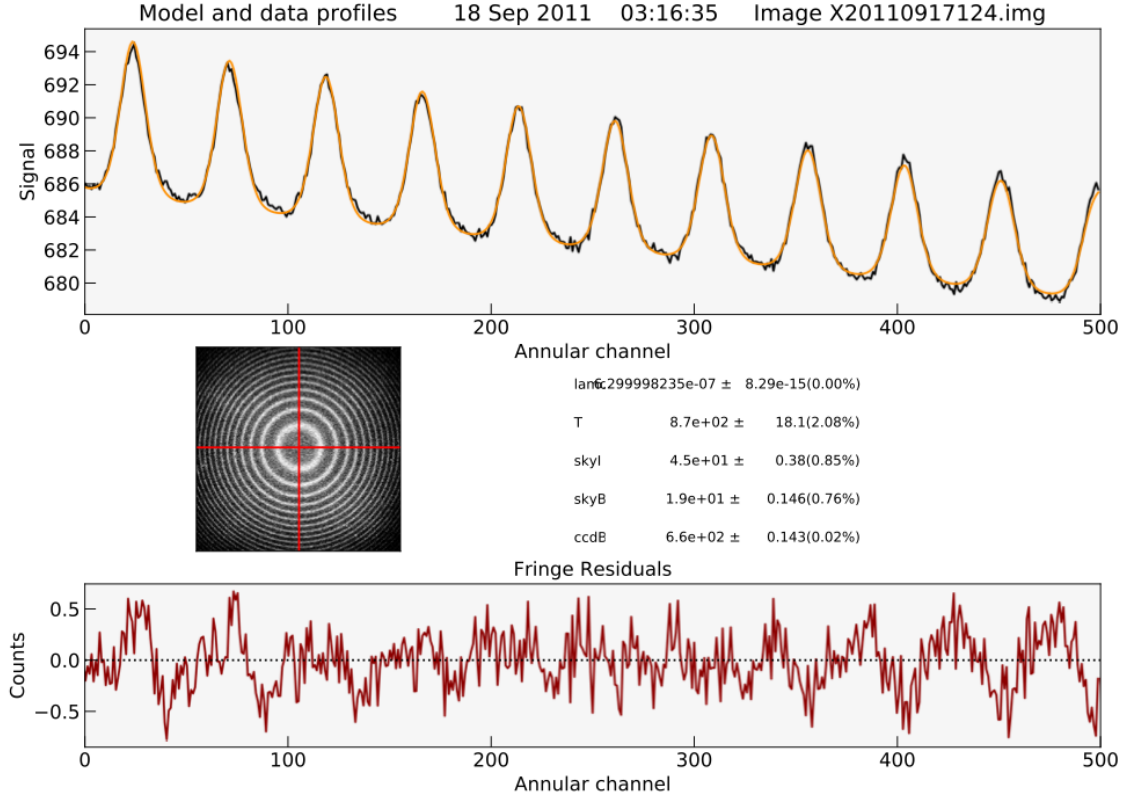


Figure. 3.3: Example output for the analysis of a 630 nm airglow image. (Top) Onedimensional multi-order fringes and the fitted airglow model. (Bottom) Fringe residuals after the best-fit procedure. (Middle) Original bidimensional multi-order fringe pattern showing the estimated center with a red cross and the estimation of the airglow source parameters.

### 3.1.3 Network of Fabry-Perot Interferometers

At equatorial latitudes, the thermospheric winds are monitored from FPI sites at Arequipa ( $16^{\circ}28'$  S,  $71^{\circ}30'$  W, magnetic latitude  $\sim 6.7^{\circ}$  S), Jicamarca ( $11^{\circ}57'$  S,  $76^{\circ}51'$  W, magnetic latitude  $\sim 2^{\circ}$  S), and Nasca ( $14^{\circ}58'$  S,  $74^{\circ}53'$  W, magnetic latitude  $\sim 5^{\circ}$  S) since 1984, 2009, 2011 respectively in a nightly basis. The recent deployments of FPIs at Jicamarca and Nasca allowed to build a network of FPI in the central region of Peru. The optical design of the Arequipa FPI was detailed by [Meriwether et al. \(2008\)](#) and the optical design of the Jicamarca and Nasca FPI is similar to the MiniME FPI design as in

Makela et al. (2009) and Meriwether et al. (2011). A basic drawing of these portable FPIs is reproduced in Figure 3.4.

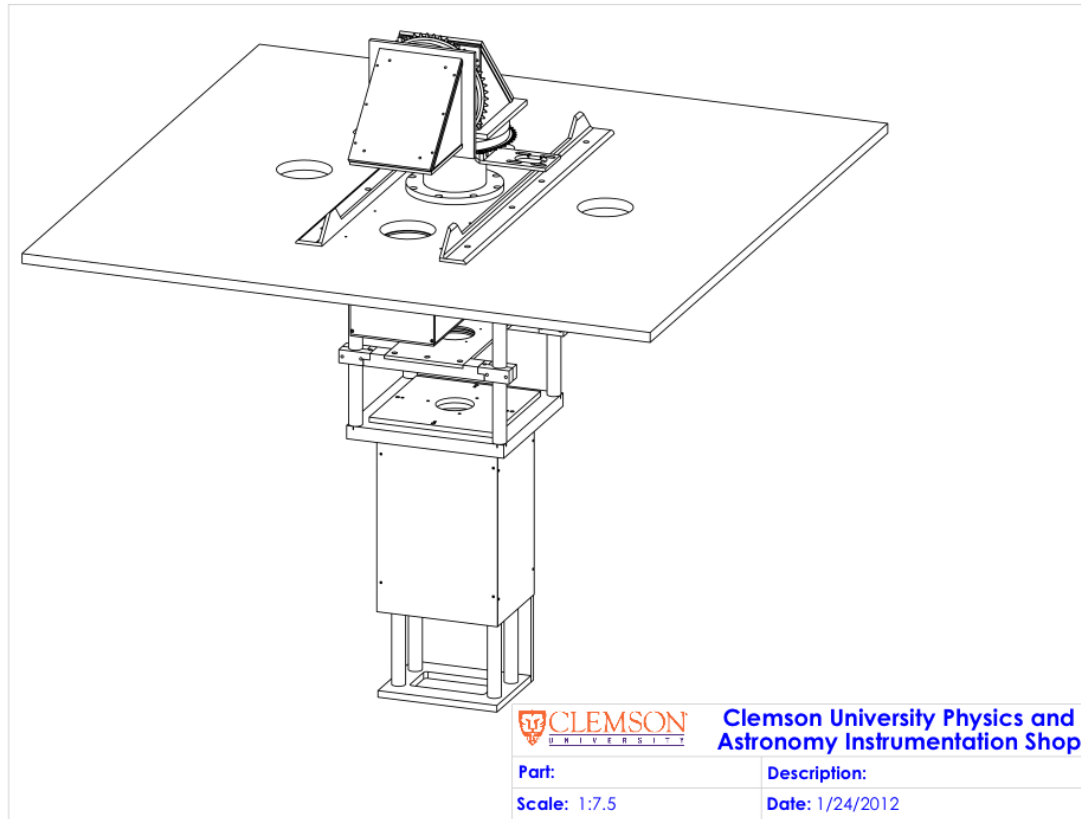


Figure. 3.4: Drawing of the optical mount of the FPIs at Jicamarca and Nasca. (Courtesy of Prof. Meriwether from Clemson University).

As seen in Figure 3.4, the optical path of each FPI starts on top with a dual axis mirror system controlled by two servo motors to point to different line-of-sights on the sky. This system can also point into a diffuse chamber to take laser calibration images. It is calibrated with the ephemerides of celestial objects and generally achieves a pointing accuracy of this system is  $\sim 0.2^\circ$  (Makela et al., 2011; Meriwether et al., 2016). They have a narrowband 630 nm filter with a half-width half-maximum of  $\sim 0.5$  nm and an etalon with



coating reflectivity of about 77.4% at 630 nm. The main optical parameters for each of the FPI is listed in Table 3.1.

Table 3.1: Technical Characteristics of the Fabry-Perot Interferometer network in Peru.

	Arequipa	Jicamarca	Nasca
Etalon Aperture	10 cm	7.5 cm	7.5 cm
Etalon Space Gap	1 cm	1.5 cm	1.5 cm
Camera CCD Size	24 $\mu\text{m}$	24 $\mu\text{m}$	13 $\mu\text{m}$
Objective Lens Focal Length	54.5 cm	35 cm	31 cm
# Interferometer Orders	2	9	11

Table 3.1 shows the technical characteristics of each of the FPI sites in Peru. The focal length of the objective lens is largest for Arequipa and smallest for Nasca and generates a larger number of interferometric orders in the latter. The etalon spacer gap is also larger for Jicamarca and Nasca than for Arequipa. This was designed to provide more interferometric orders and to avoid airglow contamination from emissions closer to 630 nm like OH contamination (Makela et al., 2011). This contamination generates a bias on the temperatures for the Arequipa FPI but does not affect the Doppler shift determination which depends only on the peak position. The exposures times of the instrument to the airglow source and to the laser were setup to fixed values. Typical values for these times were 300 sec and 30 sec respectively. However, the airglow exposure times were sometimes extended up to 10 min for less favorable conditions during December solstice months. A different approach, called dynamic integration, was used by the North American Thermosphere Ionosphere Observing Network (NATION) where each FPI of this network analyzed the collected spectra in real time to increase or decrease the integration time of the CCD camera. This approach allowed them to improve the cadence from 20 to 720 sec for typical cardinal line-of-sights (Mesquita et al., 2018).

Figure 3.5 shows an example of the interferometric fringe pattern recorded by the CCD

cameras on each FPI site for the same exposure time of 5 min. As mentioned before the setup of the optical design introduces a difference in the number of fringes and so Nasca FPI provides the most accurate estimation of Doppler shift and broadening while Arequipa shows the lowest and so this is reflected on the overall uncertainty of the estimation. It is also important to mention that Nasca is located in a remote location with very low background artificial light contamination in contrast to the other two stations.

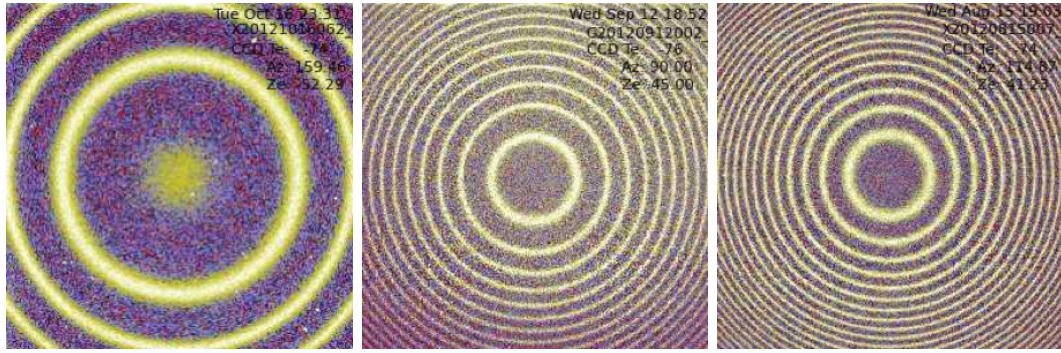


Figure. 3.5: Examples of Interferometric ring patterns for the Arequipa (left), Jicamarca (middle) and Nasca (right) FPIs.

These instruments are setup to automatically operate in a nightly basis. The pointing directions were generally cycled to provide the best sampling of the surrounding area in the central region of Peru. A laser calibration pointing is included at the beginning of each cycle to monitor the instrumental drift. The integration time was generally 5 min for a single direction, and the duration of a complete cycle depends on the pointing strategy between the FPI sites. The cycle time was generally about an hour since 2011.

Different sampling strategy have been used by the FPI network along these years. The basic operational mode is to point to cardinal pointing directions (Biondi et al., 1999; Meriwether et al., 1986). From 2011, the line-of-sight pointings were generally cycled to point to common volume directions between two closer stations along with extra pointings for the best sampling around each site (Navarro & Fejer, 2019).

### 3.1.4 Wind Velocity Estimation

The Doppler shift estimates are proportional to the bulk velocity vector of the oxygen population along the line-of-sight pointing. On the other hand, they require an absolute Doppler reference, and the etalon can drift 10-100 m/s over the night because of thermal drift which can be monitored with the calibration laser images. The absolute or zero-velocity line position is generally inferred from the vertical Doppler shift estimates under the assumption of null average vertical winds over the night. This way we use the laser and the zenith observations from 21 to 02 LT to determine an offset for the laser Doppler shift estimates. The shifted laser calibration doppler shifts are used as the best Doppler shift reference (Makela et al., 2012; Meriwether et al., 2016; Navarro & Fejer, 2019).

For a single line-of-sight, the measured Doppler shift wavelength,  $\lambda_{los}$ , is related to the line-of-sight velocity,  $v_{los}$ , through

$$v_{los} = c \left( \frac{\lambda_{los}}{630nm} - 1 \right) \quad (3.2)$$

where  $c$  is the speed of light. And measured doppler shifted velocity is the projection of the real thermospheric winds over the line-of-sight,

$$\vec{w} \cdot \hat{r}_i = v_{los} - v_{ref} \quad (3.3)$$

where  $\vec{w}$  and  $\hat{r}_j$  are the thermospheric wind and the unit vector of the  $i$ th line-of-sight pointing direction, and  $v_{ref}$  is the absolute Doppler shift which is interpolated in time from the shifted laser Doppler shifts. Therefore, for simpler operation modes like the cardinal mode, it is possible to use a simpler relationship like

$$v_h = \frac{v_{los} - v_{ref}}{\sin \alpha} \quad (3.4)$$

which shows how to get the horizontal velocity under the assumption of negligible average vertical winds. Similarly, it is possible to use several line-of-sight estimates ( $v_{los}$ ) to construct a linear system in 15-min or half-hourly cycles in order estimate the three components

of the winds under the assumption of a slow motion of the winds during the cycle time,

$$\begin{bmatrix} \sin \alpha_0 \sin \theta_0 & \sin \alpha_0 \cos \theta_0 & \cos \alpha_0 \\ & \vdots & \\ \sin \alpha_n \sin \theta_n & \sin \alpha_n \cos \theta_n & \cos \alpha_n \end{bmatrix} \begin{bmatrix} U \\ V \\ W \end{bmatrix} = \begin{bmatrix} v_{los0} - v_{ref} \\ \dots \\ v_{losn} - v_{ref} \end{bmatrix} \quad (3.5)$$

where  $\alpha$  and  $\theta$  are the zenith and azimuth angles respectively for  $n$  line-of-sights within the cycle,  $U$ ,  $V$  and  $W$  are the zonal, meridional and vertical components of the winds, and the right-side equation are the line-of-sight velocities. Of course, this method works better depending on how many line-of-sights are available. Other pointing strategies have been used as well like the common volume mode ([Makela et al., 2012](#)).

A more general approach has been developed to estimate thermospheric wind fields. [Harding et al. \(2015\)](#) showed that the smoothest wind map field can be estimated over a regional grid from a set of line-of-sight velocities. Since the calculation of the three components of the winds on a grid is a highly underdetermined problem, the optimal solution can be achieved by imposing minimum roughness of the wind field map. The roughness metric used in this regularization is expressed in terms of the discrete approximation of the curvature and gradient operators. This way the smoothest solution is found when the roughness is minimum. This is expressed by

$$\hat{u} = [A^T \Sigma^{-1} A + \lambda_0 (G^T G + \lambda_1 C^T C)]^{-1} A^T \Sigma^{-1} \bar{d}$$

where  $\lambda_0$ ,  $\lambda_1$  are the regularization constraints,  $\bar{d}$  is the line-of-sight wind vector,  $\Sigma$  is the covariance matrix and  $G$ ,  $C$  are the discrete approximation of the first and second derivatives matrices respectively; and  $\hat{u}$  is the estimated wind vector on every point of the grid. More details on this technique is found in [Harding et al. \(2015\)](#).

The database of line-of-sight estimates were used to estimate the smoothest wind field over the central region of Peru. A minimum of 8 observations was setup to enable the wind field estimation process and they were linearly interpolated in time to obtain a wind map field every 15 minutes for an 11x11 grid. Figure 3.6 shows an example of an estimated wind

map field at 250 km altitude for the 16th May 2013 around midnight  $\sim 23:45$ LT obtained from 18 line-of-sight measurements (open circles).

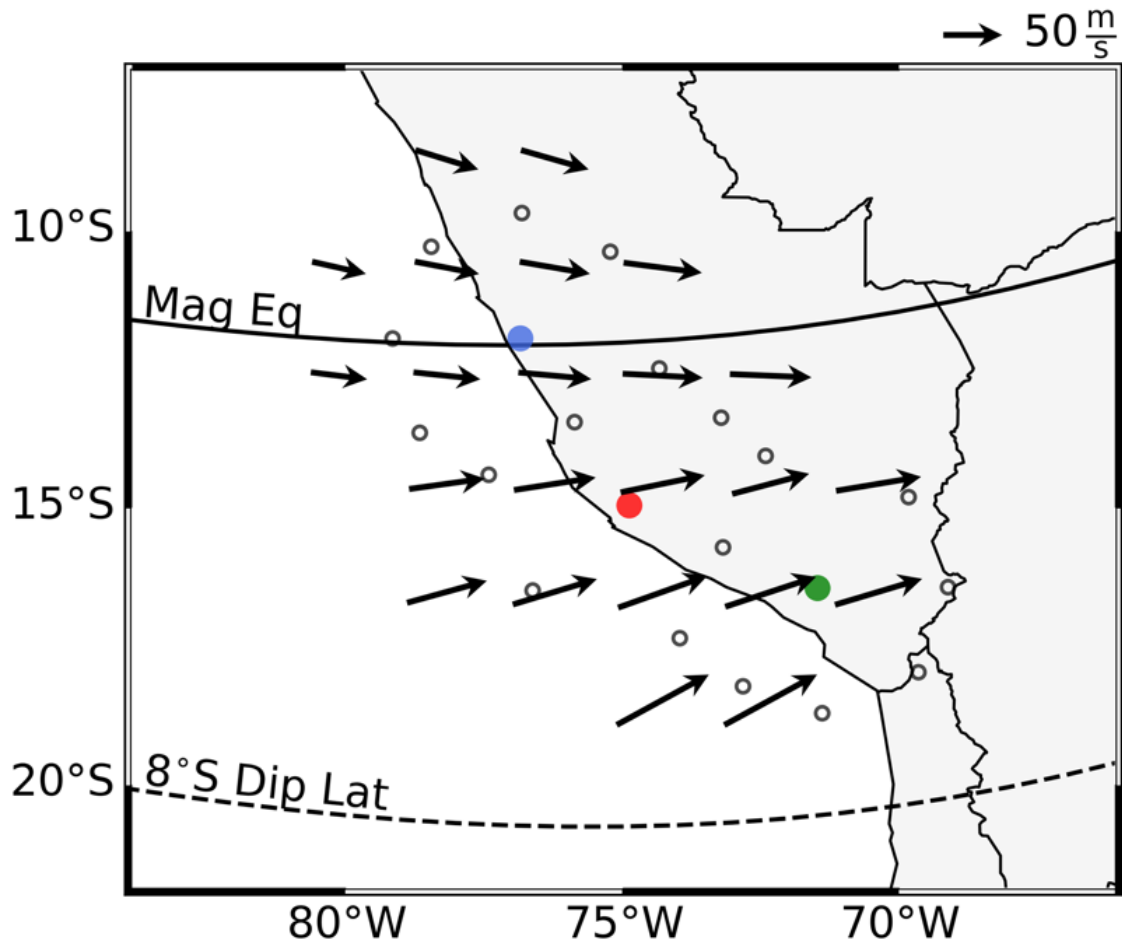


Figure. 3.6: Estimated wind field map over central Peru for 21th June 2012 around 02 LT. The filled circles show the Jicamarca (blue), Nasca (red) and Arequipa (green) FPI locations; and the open circles show the sampling points for a 250 km altitude according to predetermined line-of-sight directions. Solid and dashed curves show the magnetic equator and the 8°S dip latitude, respectively.

### 3.1.5 Database and statistics

A summary of the number of hours collected by the FPI network is shown in Table 3.2. The largest number of operation hours is Jicamarca with 22513 up to December 2017.

Table 3.2: Number of hours of data available for each FPI station and for each year.

FPI	Hours per year										Total
	before	2009	2010	2011	2012	2013	2014	2015	2016	2017	
Jicamarca	-	1058	2851	2509	3164	2674	2154	2634	2340	3130	22514
Nasca	-	-	121	2204	3217	2728	628	732	2127	2069	13826
Arequipa	6494	1175	1716	-	1448	2014	964	1933	1671	-	17415

Similarly, a monthly distribution of this dataset is shown in Figure 3.7. Periods of absence of data is noted for 2011, 2017 at Arequipa and for July 2014-June 2015 at Nasca due to technical issues. Also, lowest number of operation hours occur during December solstice months.

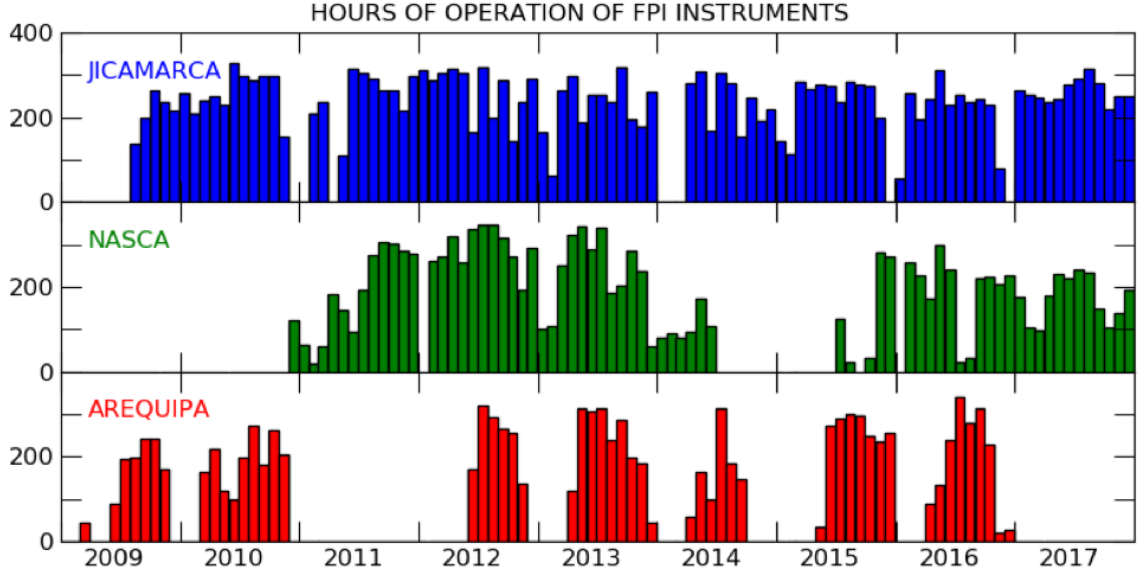


Figure. 3.7: Monthly distribution of data available for Jicamarca (top), Arequipa (middle) and Nasca (bottom) FPIs since 2009.

For the purposes of this dissertation, the images in this database were analyzed using the procedure described by [Harding et al. \(2014\)](#) as indicated in section 3.1.2, and the resultant line-of-sight wind velocities were used to estimate wind fields following [Harding et al. \(2015\)](#) under the constraints indicated in section 3.1.3. Finally, we calculated the overall average equatorial thermospheric wind velocity out of the weighted average of the wind velocities over the FPI sites for each estimated 15-min wind field,

$$\bar{w} = \frac{\sum \frac{w}{\sigma^2}}{\sum \frac{1}{\sigma^2}} \quad \sigma_{\bar{w}} = \sqrt{\frac{1}{\sum \frac{1}{\sigma^2}}} \quad (3.6)$$

where  $w$  and  $\sigma$  are the eastward (northward) wind velocity and its corresponding estimated uncertainty; and  $\bar{w}$  and  $\sigma_{\bar{w}}$  are the average eastward (northward) wind and the uncertainty of the mean respectively.

### 3.2 Jicamarca Incoherent Scatter Radar

The vertical plasma drift velocities used in this study were obtained from F-region

incoherent scatter radar observations. This technique relies on the Thomson scattering radiation by free electrons which is generally referred as incoherent scatter of weak thermal fluctuations of ionospheric plasma. The backscattered spectrum is strongly controlled by the ions and is an invertible function of plasma state parameters like number density, ion and electron temperatures, ion-neutral collision frequency, ion composition, ion drifts and the geomagnetic field (e.g., [Dougherty & Farley, 1960](#); [Farley, 1966](#); [Woodman & Hagfors, 1969](#)).

The most extensive database of incoherent scatter radar observations comes from the Jicamarca Radio Observatory (JRO) which measured the first incoherent scattered echo in April 1961 and still remains operative and scientifically active. It is located outside Lima, Peru ( $12^{\circ}$  S,  $76.9^{\circ}$  W; magnetic dip  $2^{\circ}$  N). Its antenna is formed by 18 432 dipoles occupying an area of 300 m x 300 m and organized in 64 square modules that can be controlled separately to reach a versatile beam steering. It can use 1 to 4 high-power transmitters, each one with 1.5 MW peak, and the main beam is about 1 degree wide and can be steered up to 3 degrees off zenith. More details about this radar and its history can be found in [Ochs \(1965\)](#), [Hysell et al. \(2013\)](#) and [Woodman et al. \(2019\)](#). Figure 3.8 shows a view of the Jicamarca Radio Observatory main antenna. This picture was taken near the Optical Observatory where the Fabry-Perot Interferometer is located. Note that the mountains around Jicamarca protect it from electromagnetic interference. The data acquisition and signal processing techniques used here to estimate the plasma parameters using incoherent scatter radar theory are described by [Kudeki et al. \(1999\)](#).





Figure. 3.8: View of the Jicamarca Radio Observatory. The mountains around Jicamarca protect it from electromagnetic interference (Picture taken near the Fabry-Perot Interferometer location. Courtesy of Oscar Veliz).

At Jicamarca, the Earth's magnetic field,  $\vec{B}$ , is horizontal (zero magnetic dip angle) and so the F-region plasma drift velocity perpendicular to the magnetic field,  $v_{\perp}$ , is purely dependent on the ambient electric field and has not direct influence from thermospheric winds. The relationship between these parameters is,

$$v_{\perp} = \frac{\vec{E} \times \vec{B}}{|\vec{B}|^2} \quad (3.7)$$

The Jicamarca Incoherent Scatter Radar beam is aligned perpendicular to Earth's magnetic field and to measure the vertical and zonal plasma drift velocities. Near the F-region peak, the accuracy of the typical vertical drifts and zonal drift measurements

are about 1 m/s and 15 m/s respectively during the day and somewhat larger at night (Woodman, 1971).

Such versatile radar is used under different transmitter and receiver configurations and many times in companion of other smaller systems. However, the most common experimental procedure uses half of the antenna to point  $3^\circ$  off zenith to the east and the other half to the west. This way the vertical and zonal drift velocities were obtained from the sum and difference of these radial velocities (e.g., Woodman, 1970, 1972).

For the purposes of this dissertation, we have used F-region Jicamarca vertical drifts observations from April 1968 to February 2018, and zonal plasma drifts observations starting from 1970. They were measured usually at altitudes from about 250 to 800km with a height resolution of 20-45 km and with an integration time of 5 min. Figure 3.9 shows an example of the vertical and zonal drift observations for 22-23 Jan 2014. It also shows strong plasma irregularity echoes from 19 LT to about midnight. The signal-to-noise ratio of the incoherent echoes decreases with altitude above  $\sim 500$  km and  $\sim 350$  km during day and night time respectively.

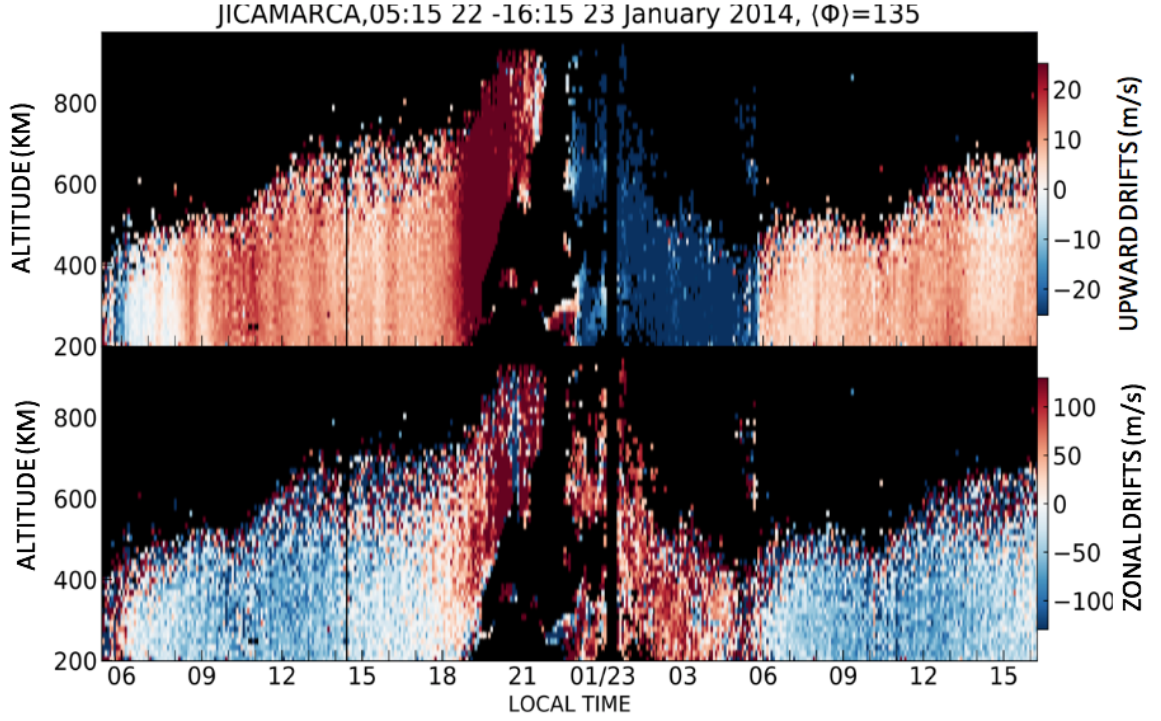


Figure. 3.9: Jicamarca vertical and zonal drifts observations from the 22 January 2014.

In general, a better signal-to-noise ratio allows observations to higher altitudes. In the case of the Jicamarca radar, this depends on the transmitter power and the operational mode but also on the plasma density. Therefore, it increases with higher solar flux and during daytime hours, and also changes with season. Other experimental procedures are able to reach higher altitudinal ranges, with the same transmitter power, by using a single beam as in [Fejer et al. \(2014\)](#). They used a single perpendicular beam with a 75 km long uncoded pulse and were able to reach up to 2000 km for Nov 2004 even at sunset with a solar flux of  $\sim 110$  sfu. This operational mode was also recently run again for April and October 2019 and we were able to reach up to about 1100 km for  $\sim 70$  sfu. Nevertheless, this radar is capable of reaching altitudes of 7000 km ([Bowles, 1963](#); [Hysell et al., 2017](#)).

Other important aspect on our database is the presence of strong echoes due to period of strong equatorial spread F as shown in Figure 3.9. These irregularities can extend largely into the altitudinal range of the observation. Their occurrence, morphology and duration

are also very variable but they generally occur more often in December solstice and around sunset and in the postmidnight sector ([Fejer et al., 1999](#)). We extended the height range of the drifts by minimizing the effects produced from these echoes, and by carefully selecting higher ranges with the highest signal-to-noise ratio.

## CHAPTER 4

### STORM-TIME THERMOSPHERIC WINDS OVER PERU <sup>1</sup>

#### 4.1 Introduction

Thermospheric winds are intrinsically important upper atmospheric parameters. Their transport of plasma along the geomagnetic field lines affect the chemical composition of the Earth's upper atmosphere, and are key drivers of ionospheric electric fields. Quiet-time thermospheric winds are driven mainly by horizontal pressure gradients of the diurnal atmospheric bulge caused by the solar atmospheric heating (e.g., [Richmond, 2011](#); [Rishbeth, 1972b](#)). The equatorial nighttime thermospheric zonal winds are closely coupled to the zonal drifts of the ambient plasma and of the equatorial plasma bubbles (e.g., [Chapagain et al., 2013](#); [Martinis et al., 2003](#); [Valladares et al., 1996](#)).

Several space-based and ground-based optical interferometers have extensively been used to monitor the dynamics of the neutral thermosphere. Fabry-Perot Interferometer observations at Arequipa, Peru ( $16^{\circ}28'$  S,  $71^{\circ}30'$  W, magnetic latitude  $\sim 6.7^{\circ}$  S) determined the local time, seasonal and solar flux dependence of the nighttime equatorial thermospheric winds during geomagnetically quiet periods (e.g., [Biondi et al., 1990, 1991, 1999](#); [Meriwether et al., 1986](#)). These observations showed that solar EUV radiation driven pressure gradients control the temporal and seasonal variations of the equatorial thermospheric winds. Recently, FPI thermospheric winds measurements have also been made in the Brazilian and African equatorial regions ([Fisher et al., 2015](#); [Makela et al., 2013](#); [Meriwether et al., 2011, 2016](#); [Tesema et al., 2017](#)).

Geomagnetically disturbed conditions lead to large departures of the dynamics of the thermosphere from its quiet-time pattern. [Richmond and Matsushita \(1975\)](#) first pointed

---

<sup>1</sup>Large parts of this chapter are comprised of the original text from the research publication Navarro, L. A., & Fejer, B. G. (2019). Storm-Time Thermospheric Winds Over Peru. *Journal of Geophysical Research: Space Physics*, 124(12), 10415-10427. <https://doi.org/10.1029/2019JA027256> with additional text and figures inside section 4.3.1. Reproduced by permission of the American Geophysical Union.

out that geomagnetic storms generate large global equatorward propagating wind perturbations extending down to equatorial latitudes. [Richmond \(1978\)](#) and [Richmond \(1979a, 1979b\)](#) showed that Joule heating is the dominant process driving global thermospheric changes capable of reaching low latitudes. The storm-time wind circulation drives ionospheric disturbance dynamo electric fields and currents ([Blanc & Richmond, 1980](#)) that can strongly affect the middle and low latitude plasma motion and density, and the occurrence of equatorial spread F ([Fejer et al., 1999](#)). National Center for Atmospheric Research Thermosphere Ionosphere Electrodynamics General Circulation Model (NCAR/TIEGCM) simulations suggest that storm driven winds can have lifetimes of up to about 8 days at equatorial regions ([C. M. Huang et al., 2005](#)).

Several studies investigated the dynamics of the middle and low latitude geomagnetic activity driven disturbance winds using Upper Atmosphere Research Satellite (UARS) Wind Imaging Interferometer (WINDII) measurements (e.g., [Emmert et al., 2001, 2002, 2004](#); [Fejer et al., 2000](#)). These studies showed that low latitude and equatorial nighttime zonal disturbance winds are westward with peak values around 03 magnetic local time, and have small seasonal dependence. [Emmert et al. \(2008\)](#) used extensive satellite and ground-based wind measurements to derive the global empirical climatological Disturbance Wind Model (DWM07). In a companion paper, [Drob et al. \(2008\)](#) presented the Horizontal Wind Model07 (HWM07), which has both a quiet-time global wind model for the background state and the DWM07. The HWM07 provides spatial, temporal and geomagnetic activity ( $A_p$ ) dependent thermospheric wind predictions. More recently, [Drob et al. \(2015\)](#) presented the HWM14, which consists of an updated quiet-time wind component and the DWM07. The combined HWM14 model also provides height, local time and latitude dependent predictions of the thermospheric winds as a function of the local  $A_p$  index.

Challenging Minisatellite Payload (CHAMP) satellite observations indicate that longitudinal averaged equatorial zonal disturbance winds are westward with small values during the day, and are largest near midnight, except during June solstice when they are largest around 03 LT ([Xiong et al., 2015](#)). These disturbances occur about 3-4 hours after the mag-

netospheric disturbances and last about 24 hours or longer, which is consistent with model results presented by [Richmond and Matsushita \(1975\)](#) and [Blanc and Richmond \(1980\)](#). CHAMP and Republic of China Satellite-1 (ROCSAT-1) satellite observations presented by [Xiong et al. \(2016\)](#) suggested that prompt penetration electric fields, due to sudden changes in the magnetospheric convection (e.g., [Fejer, 2011](#)), produce additional zonal disturbance winds that are westward in the afternoon sector and eastward in the post-midnight sector.

So far, few studies have examined the response of low latitude thermospheric winds to large geomagnetic storms. [Emery et al. \(1999\)](#) studied the thermospheric response to the November 1993 storm using TIEGCM along with the Assimilative Mapping of Ionospheric Electrodynamics (AMIE) procedure, which included data of 154 ground magnetometers and ion drift and electron precipitation measurements. These simulations showed traveling atmospheric disturbances reaching equatorial latitudes about 4 hours after the large high latitude energy depositions, and largest equatorial westward disturbances around 22 LT for all longitudes. WINDII observations during the recovery phase of the October 1998 storm showed large latitudinal variability on the daytime disturbance winds, which reversed from westward to eastward at magnetic latitudes of about  $30^\circ$ , and largest disturbance winds at F-region heights ([Fejer & Emmert, 2003](#)). FPI observations from Arequipa showed reductions in the nighttime eastward and poleward winds 24 hours after the onsets of the August 1998 and October 2000 geomagnetic storms ([Meriwether et al., 2013](#)). Most recently, [Malki et al. \(2018\)](#) reported strong zonal and meridional thermospheric winds perturbations in the westward and equatorward directions around midnight over the northern African sector ( $31.2^\circ$  S,  $7.8^\circ$  W, magnetic latitude  $\sim 23^\circ$  N) 6 hours after the onset of the 27-28 February 2014 storm. These results are consistent with predicted delays in the establishment of a steady storm-driven circulation pattern (e.g., [Richmond & Matsushita, 1975](#); [Blanc & Richmond, 1980](#)).

We used extensive observations from recently deployed FPIs in the Peruvian equatorial region sector to examine for the first time the local time and seasonal dependence of the nighttime disturbance winds. In the following sections, we will first describe our database



and determine our quiet-time baselines used to calculate the disturbance winds. Then, these baseline winds are compared with the corresponding quiet-time winds from HWM14. Next, we present our season-dependent disturbance wind patterns and compare them with results from the DWM07, which has been extensively used in storm-time wind studies (e.g., [Malki et al., 2018](#)). We also examine the dependence of the zonal disturbance winds on both local and extended levels of geomagnetic activity. Finally, we present measurements during and shortly after two geomagnetic storms showing that zonal disturbance winds are more accurately accounted for using multi-hour geomagnetic activity parameters (e.g., time-averaged Kp indices) than local disturbance parameters.

## 4.2 Measurement Technique

Equatorial thermospheric winds are routinely monitored from FPI sites at Jicamarca ( $11^{\circ}57'$  S,  $76^{\circ}51'$  W, dip latitude  $\sim 0^{\circ}$ ), Nasca ( $14^{\circ}58'$  S,  $74^{\circ}53'$  W, dip latitude  $\sim 2.5^{\circ}$  S) and Arequipa ( $16^{\circ}28'$  S,  $71^{\circ}30'$  W, dip latitude  $\sim 4^{\circ}$  S) since 2009, 2011 and 1984, respectively. These probes measure the 630 nm airglow Doppler-shifted emission line along specific line-of-sight directions. Starting in 2011, the FPI pointing directions have generally been cycled to provide the best sampling of the surrounding area in the central region of Peru. Figure 4.1 shows the locations of the FPIs and their line-of-sights. The integration time is typically about 5 min for a single direction, and the complete cycle time is about an hour. A 632.8 nm HeNe laser observation is included at the beginning of each cycle with an integration time of 30 seconds to monitor instrumental drift. The etalon clear aperture and spacer gap for both Jicamarca and Nasca FPIs are 70 mm and 1.5 cm respectively, and 100 mm and 1 cm for Arequipa FPI. The optical design of the Jicamarca and Nasca FPIs is similar to MiniME FPI in the RENOIR network (e.g., [Makela et al., 2009](#); [Meriwether et al., 2011](#)). The Arequipa FPI was described by [Meriwether et al. \(2008\)](#).

The signal recorded on every pixel of the FPI image is analyzed as the exposure of a Gaussian airglow source to the instrument transfer or Airy function. Following [Harding et al. \(2014\)](#), this signal is modeled by the Fredholm integral equation of the first kind between a modified Airy function and the Gaussian spectrum of the oxygen line source.



The modified Airy function includes an intensity quadratic fall off factor and is blurred by a point-spread function to account for different deviations from the ideal Airy function like the radially decreasing action of the optical transmission among other optical aberrations (e.g., [Meriwether et al., 2008](#)). Since the laser has a known spectrum, the images are used to estimate different parameters of the instrumental function such as the etalon spacer gap, reflectivity, and optical magnification constant. These laser images are useful for calibration purposes and for monitoring the drift of the instrumental parameters throughout the night. These parameters are later used to estimate airglow parameters such like the Doppler frequency shift and broadening. More details on this method are found in [Harding et al. \(2014\)](#).

The line-of-sight wind velocities were calculated using the procedure described by [Makela et al. \(2013\)](#) and [Meriwether et al. \(2016\)](#) where the laser calibration images from 21-02 LT are used to get the best zero Doppler shift reference under the assumption of zero average vertical wind. This is a less restrictive assumption than that of zero instantaneous vertical wind used in past ([Harding et al., 2014](#)). As pointed out by [Harding et al. \(2015\)](#), the smoothest wind field can be estimated over a regional grid from a set of line-of-sight velocities considering that each of these velocities is the projection of the thermospheric wind over that particular direction. The optimal solution of the resultant underdetermined linear system imposes minimum roughness of the wind field. The roughness metric used in this regularization is expressed in terms of the discrete approximation of the curvature and gradient operators. This way the smoothest solution is found when the roughness is minimum ([Harding et al., 2015](#)). A minimum of 8 observations was set up to enable this process and they were linearly interpolated in time to obtain a wind map field every 15 minutes on a 11x11 grid. This estimation was performed only for the horizontal wind components. Figure 4.1 shows the estimated wind map field at ~23:45LT during 16th May 2013, for an assumed emission height of 250 km, obtained from 18 line-of-sight measurements.

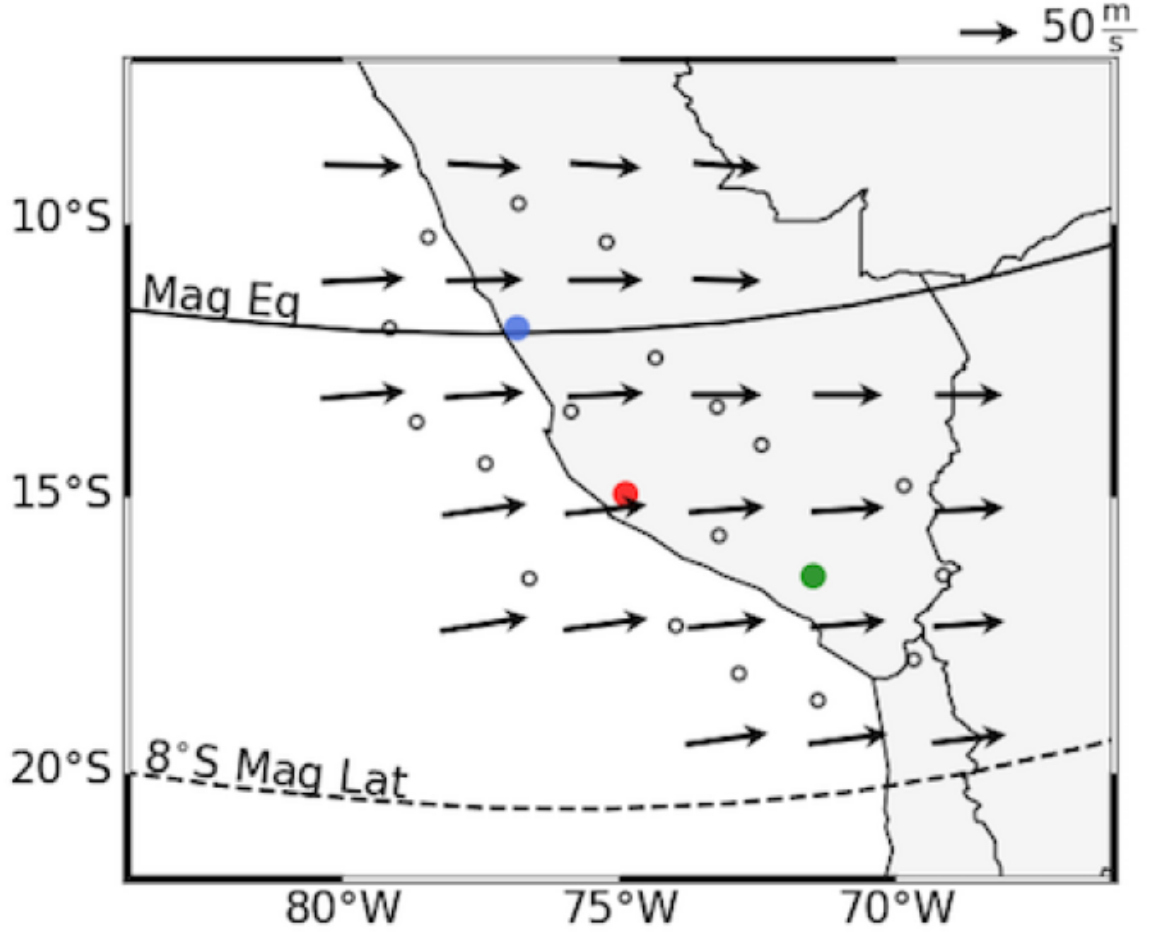


Figure. 4.1: Estimated wind field map over central Peru for 16th May 2013 around midnight ( $\sim 23:45$  LT). The filled circles show the Jicamarca (blue), Nasca (red) and Arequipa (green) FPI locations; and the open circles show the sampling points for a 250 km altitude according to predetermined line-of-sight directions. Solid and dashed curves show the magnetic equator and the 8° S magnetic latitude, respectively.

By using the wind field estimation, we found that the zonal and meridional wind velocities over the FPI sites differed by less than about 5 m/s on average. Therefore, we combined the horizontal winds over the FPI site to improve the statistical significance of our results. The overall average thermospheric wind velocities were calculated from the estimated wind velocities over each FPI site using,

$$\bar{w} = \frac{\sum \frac{w}{\sigma^2}}{\sum \frac{1}{\sigma^2}} \quad \sigma_{\bar{w}} = \sqrt{\frac{1}{\sum \frac{1}{\sigma^2}}}$$

where  $w$  and  $\sigma$  are the eastward (northward) wind velocity and its corresponding estimated uncertainty over each FPI site, and  $\bar{w}$  and  $\sigma_{\bar{w}}$  are the average eastward (northward) wind velocity and the uncertainty of the mean velocity, respectively.

Each instrument recorded a total of  $\sim 15000$  hours since 2009. However, this method requires high-quality conditions for most of the line-of-sights, and so we used 5946 hours of estimated wind fields from June 2011 to December 2017 with 15 measurements per hour on average. Since the December solstice measurements before 23 LT had generally larger errors, they were not studied. This dataset was analyzed on bimonthly bins but most of the results presented consist of 4-months seasonal averages. Table 4.1 shows the seasonal distribution of the number of hours available within this range. This database has the largest number of observations during June solstice and the smallest in December solstice, mostly due to the high presence of clouds during local summer. The December measurements were generally reliable only after about 23 LT.

Table 4.1: Seasonal Distribution of the 15-min averaged Wind Field Database.

Number of hours	Nov-Feb	Mar-Apr Sep-Oct	May-Aug
Kp $\leq$ 3	646	1930	2501
Kp $>$ 3	94	498	277

### 4.3 Results

#### 4.3.1 Quiet-time average winds

We have determined initially the best geomagnetically quiet-time criteria for the thermospheric winds. The zonal and meridional wind components were averaged in half-hourly

bins, for each season and for various Kp-based criteria varying from local quiet ( $K_p < 3$ ) to very extended quiet (all  $K_p < 3$  over 48 hours) conditions to determine the best quiet-time baseline.

Figure 4.2 shows a comparison of the quiet-time equinoctial eastward winds under different geomagnetically quiet conditions. For each case, the differences between the half-hourly averaged geomagnetic activity level,  $K_p$ , and the mean  $K_p$  was smaller than 0.1. Similarly, the half hourly-averaged decimetric solar flux index ranged from 105 to 115 solar flux units. The standard deviations of the half-hour bins are generally about 20 m/s, except at early night where they increase to about 30 m/s. It shows an increment on the magnitude of the zonal winds for more stringent criteria.

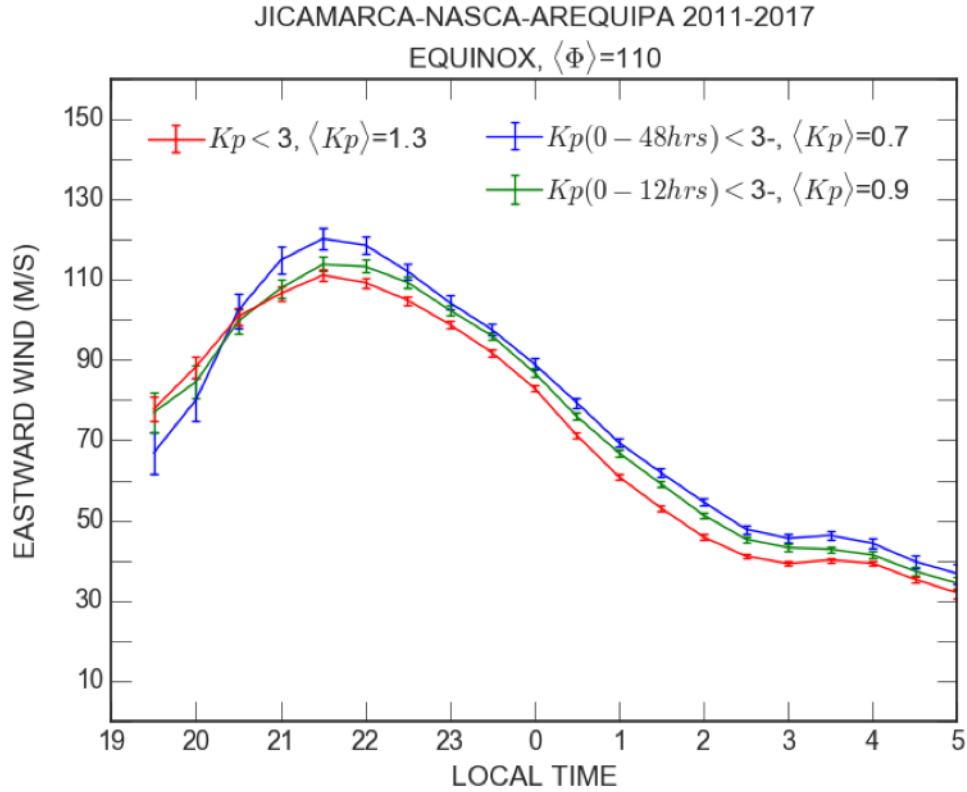


Figure. 4.2: Comparison of equatorial thermospheric eastward winds for Equinox under (red) local, (green) 12-hours and (blue) 48-hours extended quiet conditions. Error bars correspond to the standard errors of the mean.

Figure 4.2 shows that the magnitude of the zonal winds increases for more stringent quiet criteria. The maximum peak increase from 110 m/s to 120 m/s from local to 48-hours extended quiet criteria. There is a steady offset between these baselines of about 10m/s starting at 21 LT up to rest of the night. For most to the nighttime, the change in the magnitude of the zonal winds between the 12- and 48-hours extended quiet was smaller than 5 m/s. Therefore, we have chosen our reference quiet-time winds to correspond to all  $K_{ps} < 3$ — over 12 hours.

Figure 4.3 shows the bimonthly quiet-time averaged climatological wind patterns over Peru for moderately low solar flux conditions of about 110 units. It was calculated using a bimonthly sliding window every 2 weeks except during December solstice when this window was one month longer and calculated for every month due to the less data available, and as a results, it is often difficult to estimate the thermospheric winds due to the frequent occurrence of plasma irregularities(Fejer et al., 1999) and to the frequent occurrence of cloudy skies during this season (Biondi et al., 1999). In general, the standard deviations, the average Kp and the average solar flux were about 20 m/s, 0.9 and 110 units respectively except around the postmidnight sector in December solstice where the flux was a bit higher to about 130.

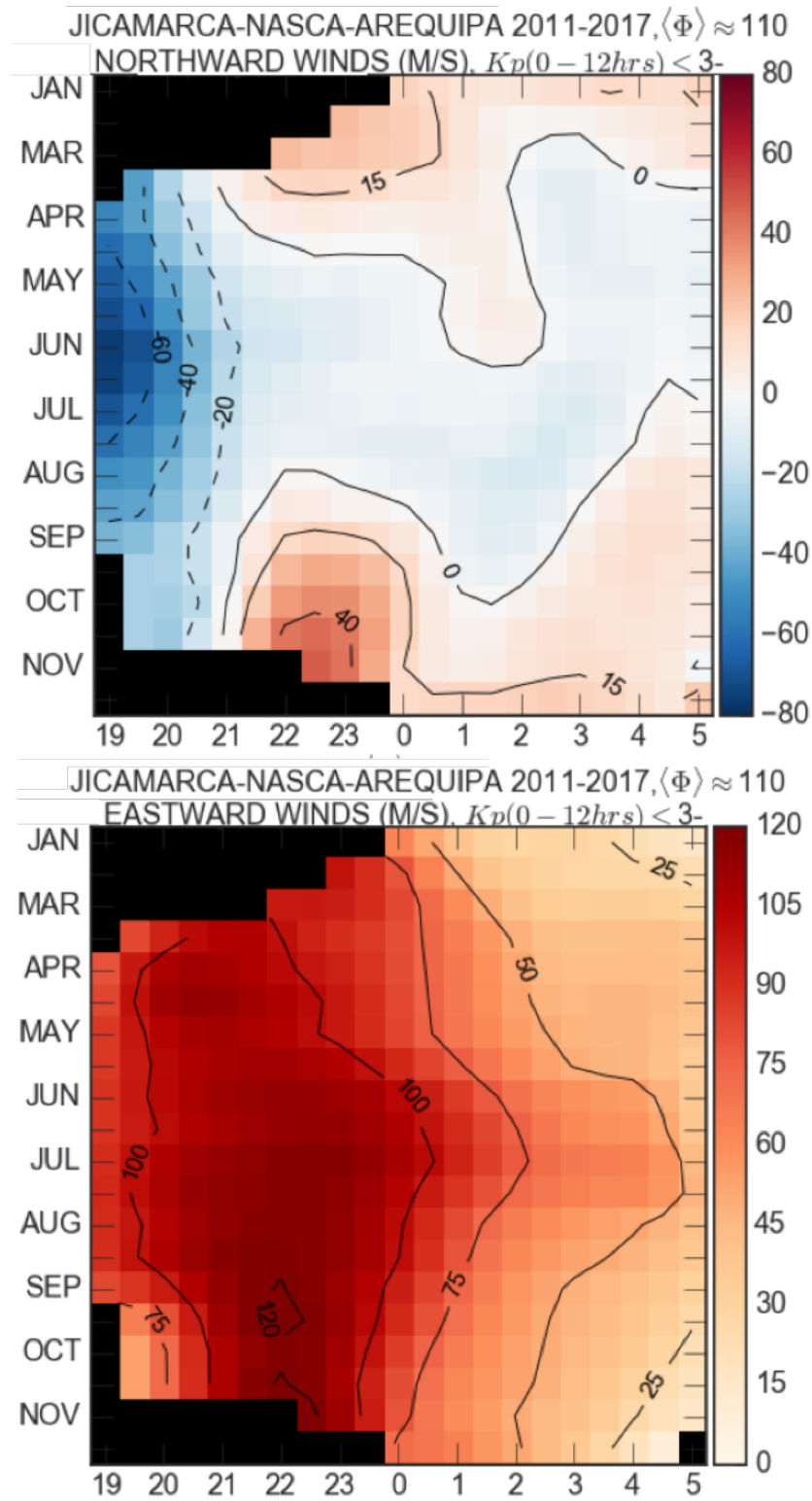


Figure. 4.3: Annual variation and local time dependence of the night-time thermospheric (top) zonal and (bottom) meridional winds for geomagnetically quiet conditions over Peru.

Figure 4.3 shows in more detail the annual variation of the night-time thermospheric winds. They are eastward all night with magnitudes and peak times that change throughout the year. These peak magnitudes are strongest around autumnal equinox and last longer around June solstice. The peak time are around 21 and 22 LT for the vernal and autumnal equinox respectively and about 21 to 23 LT around June solstice. The meridional winds are southward from Apr to Oct with decreasing magnitudes at early night. Around autumnal equinox, they reverse to northward around 21 LT, reach a peak value of about 40 m/s around 22:30 LT, and decrease to small values shortly after. The same for vernal equinox but with a peak value of about 15 m/s. Around June solstice they decrease and become small from 21 LT. There is a pronounced equinoctial asymmetry on the equinoctial winds on both components. This figure shows the baselines used on following sections to remove the quiet-time average patterns.

In this study, our quiet-time wind patterns consist of 4-month season averages except for when improving prediction on the storm cases, section 4.3.4, where the bimonthly averages were used to optimize the prediction.

Figure 4.4 shows the seasonal dependence of our half-hour averaged quiet-time zonal and meridional winds and the corresponding results from the HWM14. The average solar flux ranged from 105 to 120 solar flux units (sfu), for equinox and June solstice and from 125 to 135 for December solstice, and the average Kp ranged from 0.7 to 1.1. The standard deviations vary from about 15 to 25 m/s for the zonal winds and from about 12 to 20 m/s for meridional winds. The HWM14 winds were first evaluated at each FPI location for an altitude of 250 km and zero geomagnetic activity level ( $A_p=0$ ) every half-hour and then averaged to get an overall model prediction. The variability of the model results, calculated from the standard deviations of each half-hour bin, is shown as the shaded areas. This variability is largest during equinox and for the meridional winds.

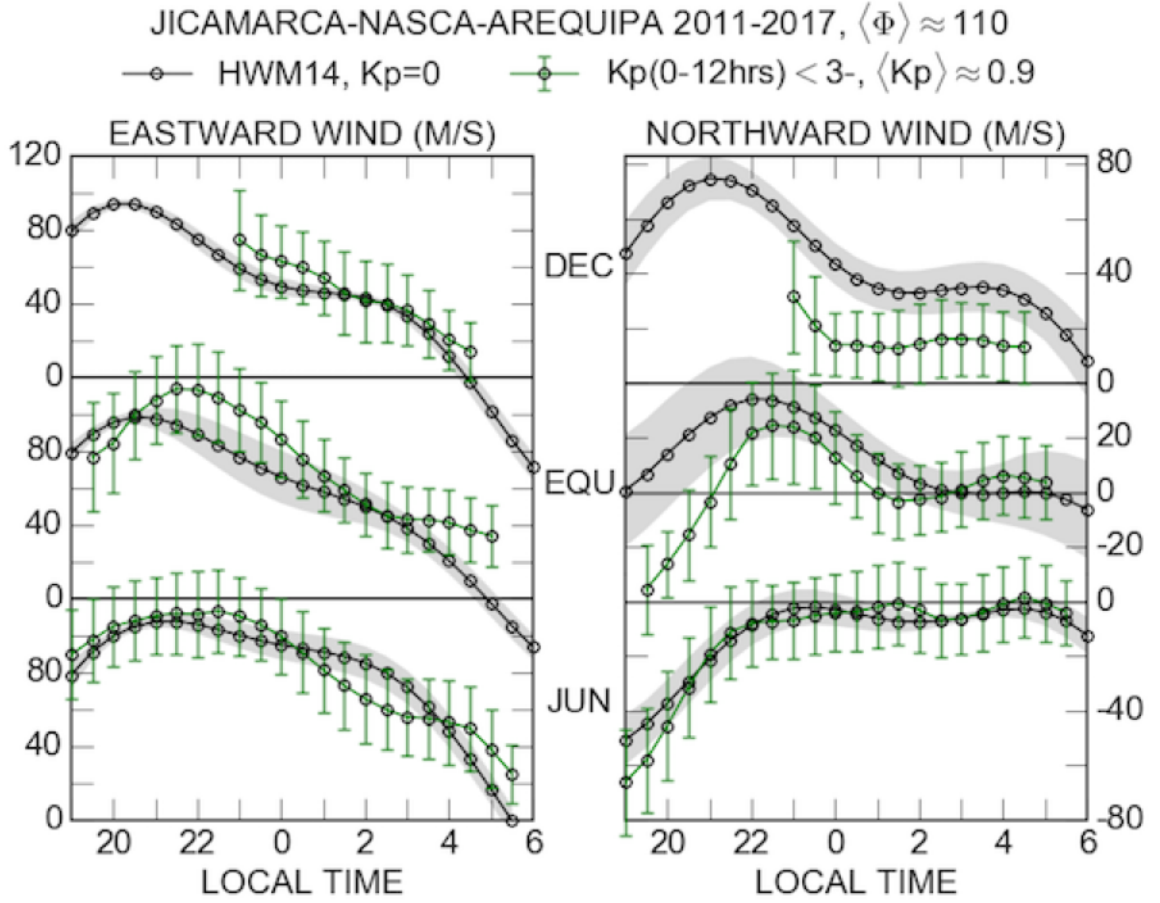


Figure. 4.4: Seasonal variation of equatorial thermospheric winds under 12-hours of extended geomagnetic quiet conditions and the corresponding quiet-time predictions from the HWM14. The error bars and shadowed regions correspond to the standard deviations.

Figure 4.4 shows that for moderately low solar flux conditions our quiet-time zonal winds are eastward with peak values of about 115 m/s at about 22 LT and decrease toward dawn. The June solstice and equinoctial nighttime meridional winds are southward in the early night with decreasing magnitudes. The equinoctial meridional winds reverse to northward at about 21 LT, have a peak value of about 25 m/s near 22.5 LT, and then decrease up to about 01 LT. They have very small magnitudes in the late-night sector. The June solstice meridional winds decrease from the early night period up to about 23



LT and have small values in the postmidnight period. The December solstice meridional winds have nearly constant northward values of about 15 m/s from about midnight to 05 LT. The average wind patterns shown in Figure 4.4 are similar to those reported in previous equatorial studies (e.g., Biondi et al., 1990, 1999; Meriwether et al., 2016). They are also in general agreement with the predictions from the HWM14, which is expected since a large database of Peruvian FPI measurements was used in the development of this model. However, there are also noticeable differences between the FPI and the model results. In particular, the model significantly underestimates the eastward winds in the premidnight sector and the early night southward winds during equinox, and also significantly overestimates the northward meridional wind during December solstice in the postmidnight sector, as seen from Figure 4.4. Some of the differences between the HWM14 and the Peruvian FPI data were already reported by Drob et al. (2015) and Meriwether et al. (2016). We will later show that the large underestimates of the quiet-time eastward winds result in significant underestimates of the disturbed zonal winds by the HWM14.

#### 4.3.2 Average disturbance winds

Middle and low latitude thermospheric winds can be severely disturbed by geomagnetic storm-driven enhanced energy and momentum input into the high latitude ionosphere. Figure 4.5 shows the local time and seasonal dependence of our thermospheric winds for  $K_p > 3$  geomagnetic conditions, and the corresponding predictions from the HWM14. In this case, the average solar flux ranged from 105 to 125 sfu for all seasons and the average geomagnetic activity levels ranged from 3.9 to 4.3. The standard deviations shown as bars vary from 10 to 30 m/s for the zonal winds and from 12 to 25 m/s for the meridional winds. The HWM14 predictions were evaluated including its disturbance component, provided by the DWM07 (Emmert et al., 2008), at each FPI location for an altitude of 250 km, for a geomagnetic activity level of  $A_p = 25$  to correspond to the same average level of geomagnetic activity as the FPI winds ( $K_p \approx 4.1$ ) and averaged to get the full HWM14 prediction.

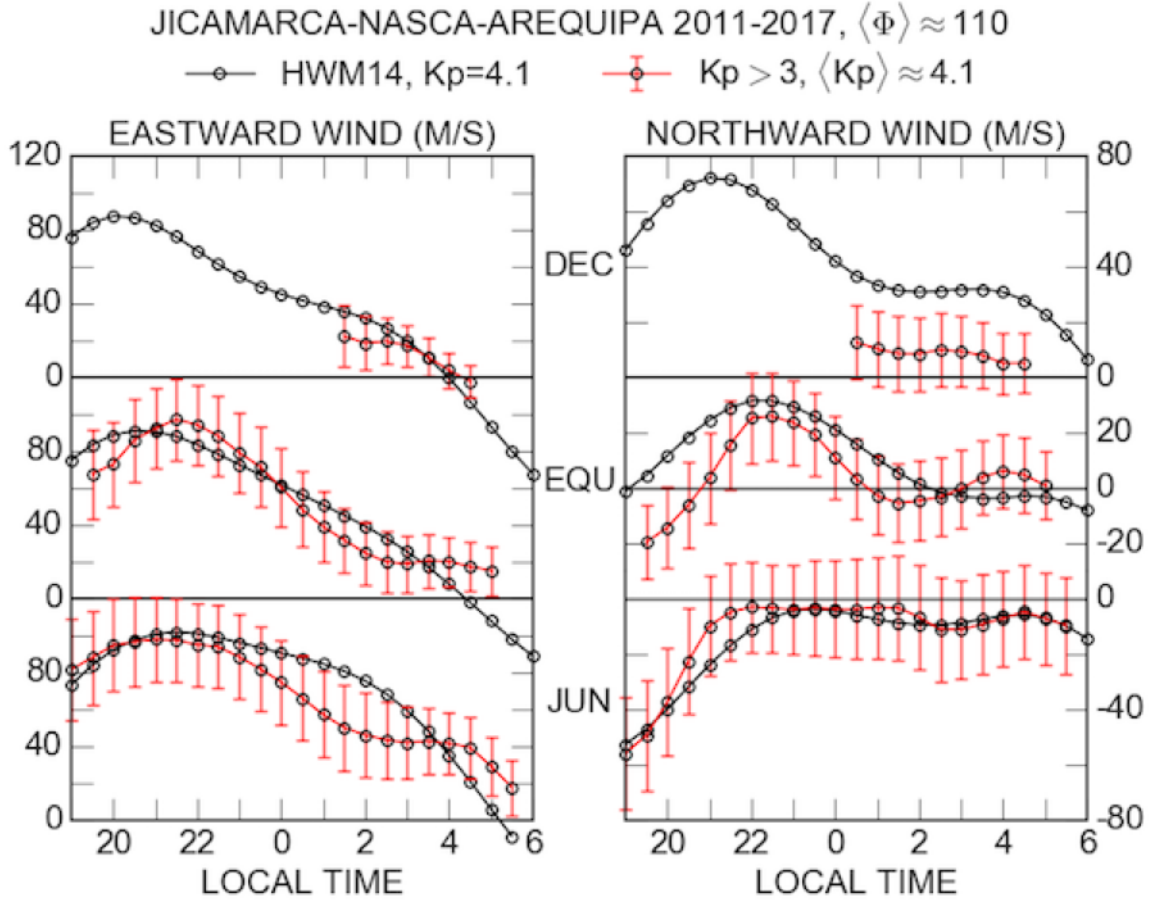


Figure. 4.5: Seasonal comparison of disturbed equatorial thermospheric winds for local geomagnetic conditions i.e.  $K_p > 3$ ; and corresponding predictions from the HWM14 evaluated for  $A_p=25$ . The error bars correspond to the standard deviations.

Figure 4.5 shows generally a much better agreement between the FPI and the HWM14 disturbed winds than between their quiet-time values. The FPI and the HWM disturbed eastward winds presented in Figure 4.5 are about 25 m/s and 10 m/s smaller than their corresponding quiet-time values shown in Figure 4.4, respectively. This difference is the result of the smaller quiet-time eastward winds predicted by the HWM14. As in the quiet-time case, the FPI and HWM meridional disturbed winds are generally in good agreement except for the equinox early night and December solstice late night periods.

Figure 4.6 compares our extended quiet-time seasonal patterns shown in Figure 4.4 and the local disturbed ( $K_p > 3$ ) seasonal averaged winds shown in Figure 4.5. As mentioned before, these patterns are half-hourly averages for the corresponding geomagnetic conditions. The standard errors of the means are about 1 m/s and 3 m/s for the extended quiet-time and local disturbed patterns respectively. Figure 4.6 indicates that the average zonal disturbance winds are nearly season-independent in the premidnight sector for equinox and June solstice and largest during equinox in the postmidnight period. The meridional disturbed winds are slightly more northward in the premidnight sector for equinox and June solstice and more southward in the postmidnight sector for December and June solstices.

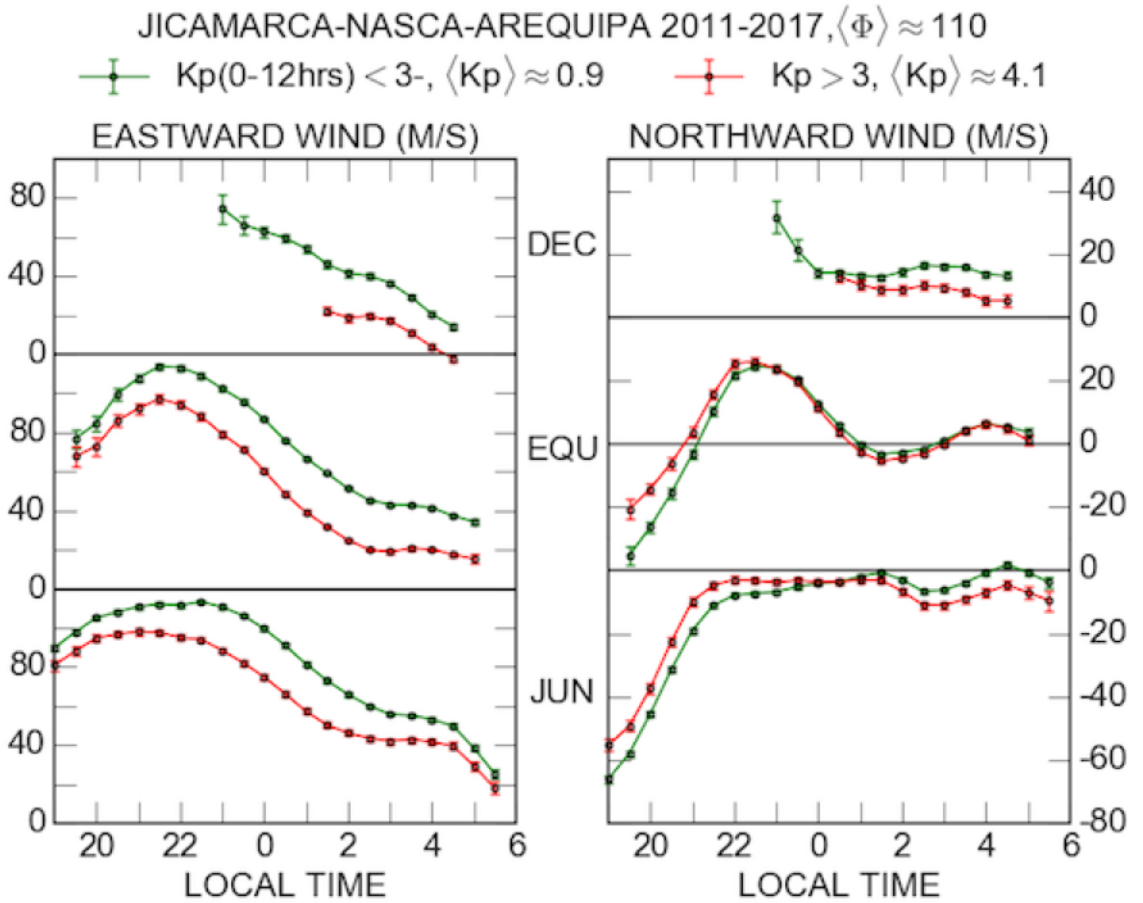


Figure. 4.6: Comparison of 12-hours extended quiet and local disturbed thermospheric winds over Peru.

Figure 4.7 shows in more detail the local time and seasonal variations of the FPI disturbance winds presented in Figure 4.6, and the corresponding results from the seasonal-independent DWM07 (Emmert et al., 2008). The corresponding 12-hours extended quiet-time seasonal baselines were removed and the resultant disturbances were averaged in local time and season. The average geomagnetic activity enhancement,  $\Delta K_p$ , ranged from 3.1 to 3.3. The standard deviations are  $\sim 15$  m/s most of the night, except in the early night period when they are about 25 m/s, and the error bars indicate the standard errors of the means, which are generally about 2 m/s. The DWM07 predictions, shown as solid black lines, were evaluated at the FPI locations for an altitude of 250 km, for a geomagnetic activity level of  $A_p=25$ , which corresponds to an enhancement of  $\Delta K_p=3.2$  over the geomagnetic quiet level of  $\langle K_p \rangle = 0.9$ , and averaged to get a single prediction from this model.

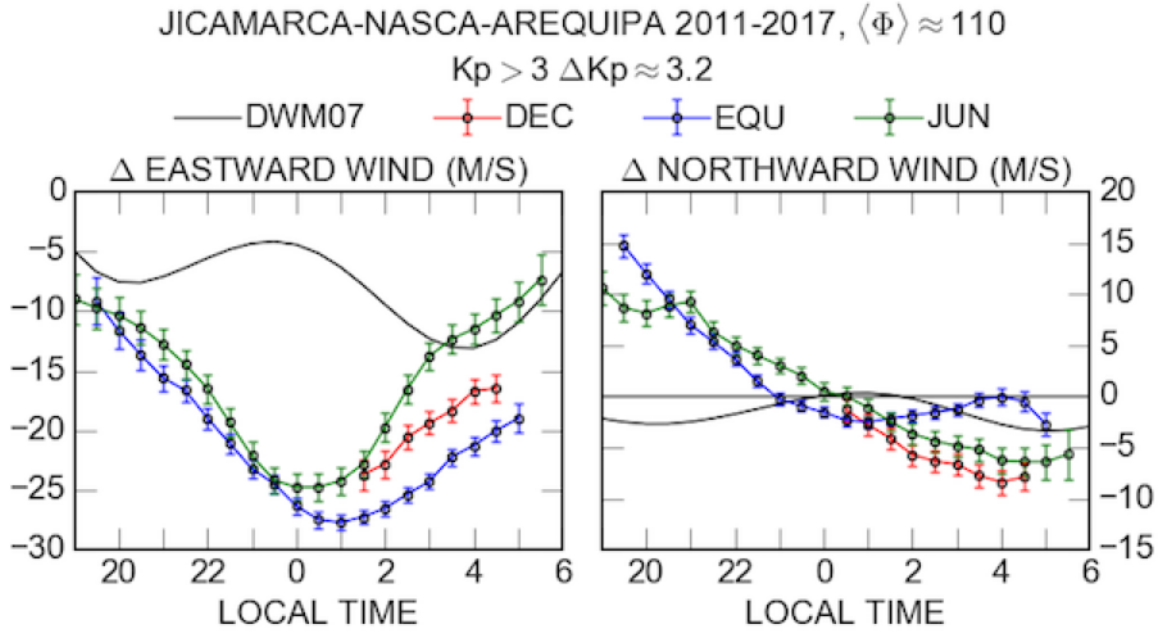


Figure. 4.7: Local time and seasonal comparisons of FPI disturbance winds ( $K_p > 3$ ) with predictions from the DWM07 for geomagnetic activity enhancement of  $\Delta K_p = 3.2$  ( $A_p \approx 25$ ). The error bars correspond to the standard errors of the means.

Figure 4.7 shows that the FPI equinoctial and June solstice zonal disturbance winds have comparable values in the premidnight sector where they increase with local time and that they reach their largest magnitudes around midnight. The postmidnight zonal disturbance winds are largest (smallest) during equinox (June solstice) and decrease toward dawn in all seasons. The DWM07 predicted zonal disturbance winds have much smaller magnitudes than the FPI disturbance winds, except in the late-night period near the time of its peak value. As noted earlier, this is partly due to the HWM14 smaller quiet-time eastward winds. The meridional disturbance winds are very small at all seasons, as already shown in Figure 4.6. The FPI equinoctial and June solstice meridional disturbance winds are northward with comparable small values in the premidnight sector and have peak values near dusk. In the postmidnight sector, they are southward with largest values during December solstice and smallest during equinox. The DWM07 meridional disturbance winds are southward with generally much smaller values than the FPI disturbance winds.

Figure 4.8 shows the equinoctial zonal disturbance winds for the midnight period as a function of local Kp and corresponding average predictions from DWM07. It shows the nearly linear Kp dependence of the disturbance winds, which is in agreement with results from previous studies (e.g., Emmert et al., 2008; Brum et al., 2012). The FPI and DWM07 average patterns show similar linear Kp dependence starting from their corresponding average quiet average values but, as pointed out earlier, they start from significantly different quiet time values.

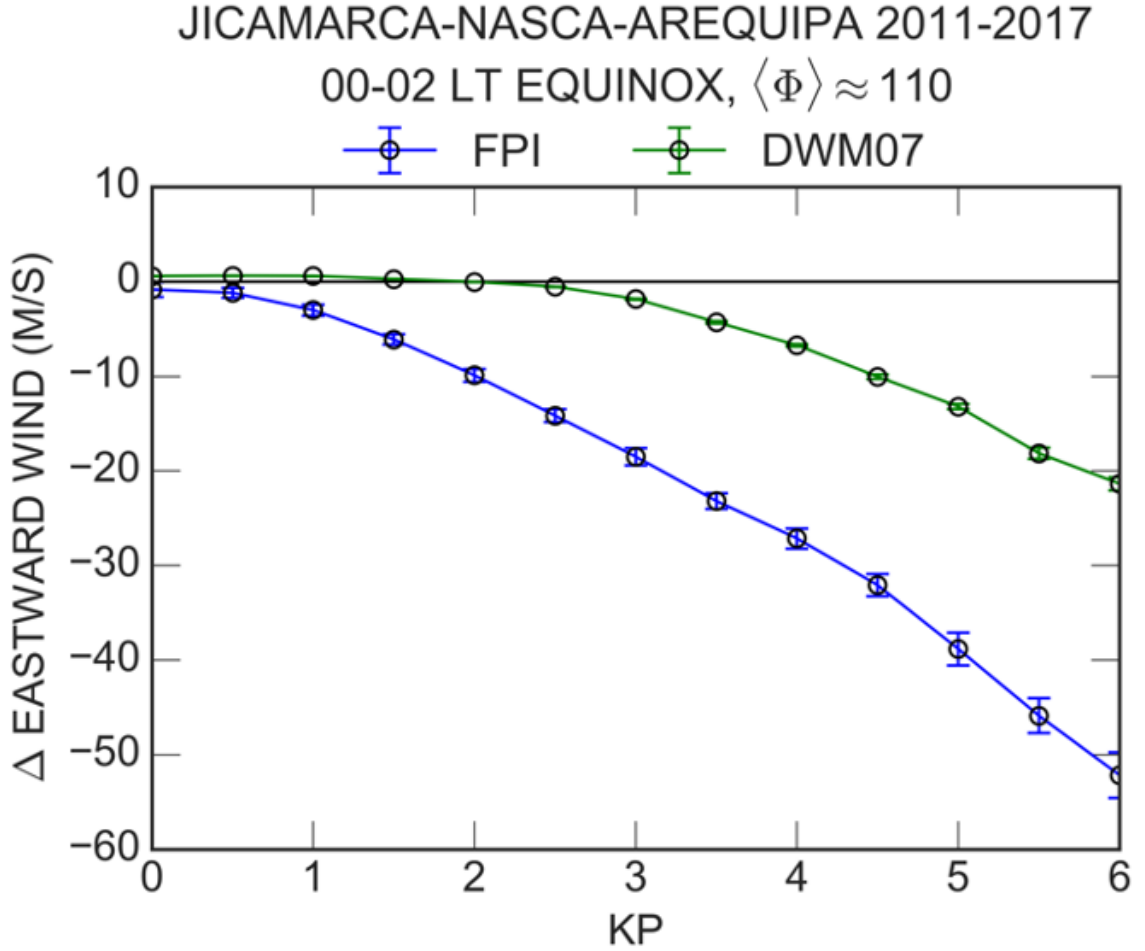


Figure. 4.8: Averaged FPI and DWM07 disturbance winds as a function of local Kp for the midnight period. The error bars correspond to the standard errors of the means

#### 4.3.3 Extended geomagnetic effects

The low latitude thermosphere and ionosphere are strongly affected for periods from few hours to few days by storm-time enhanced energy deposition into the high latitude ionosphere (e.g., [Blanc & Richmond, 1980](#); [Fuller-Rowell et al., 1996](#)). We have studied the relationships of the Peruvian FPI disturbance winds for extended periods of geomagnetic activity using up to about 12-hour averaged Kp values. The best estimates of the zonal disturbance winds were obtained using for 9-hour averaged Kp averages, but similar results were also obtained using slightly longer Kp averages. The meridional disturbances were

not improved using Kp averages. Since meridional wind disturbances can have shorter lifetimes, they can be estimated best using shorter-term disturbance parameters such as hourly AE and polar cap indices. These parameters would also improve the prediction of zonal disturbance winds by taking time delay effects into account.

Figure 4.9 shows the equinoctial zonal disturbance winds for local and 9-hours of continuously high geomagnetic activity level. These averages were calculated following the same procedure as for the seasonal disturbances shown in Figure 4.7. The averages of the local and 9-hours enhanced geomagnetic activity levels ranged from 3.4 to 3.6. As expected, Figure 4.9 indicates that extended periods of geomagnetic activity lead significant increases in the magnitude of the disturbance winds, particularly in the postmidnight period, even though the average geomagnetic activity levels are about the same. They show that for a geomagnetic activity level of  $K_p \approx 4.4$  the zonal disturbance winds around midnight and in the postmidnight sector increase by  $\sim 8$  m/s from local to 9-hours of steady disturbed conditions. Basically, same results were obtained for June solstice. The average meridional disturbance winds derived from local and extended disturbance conditions turned out to be essentially identical and, therefore, are not shown.

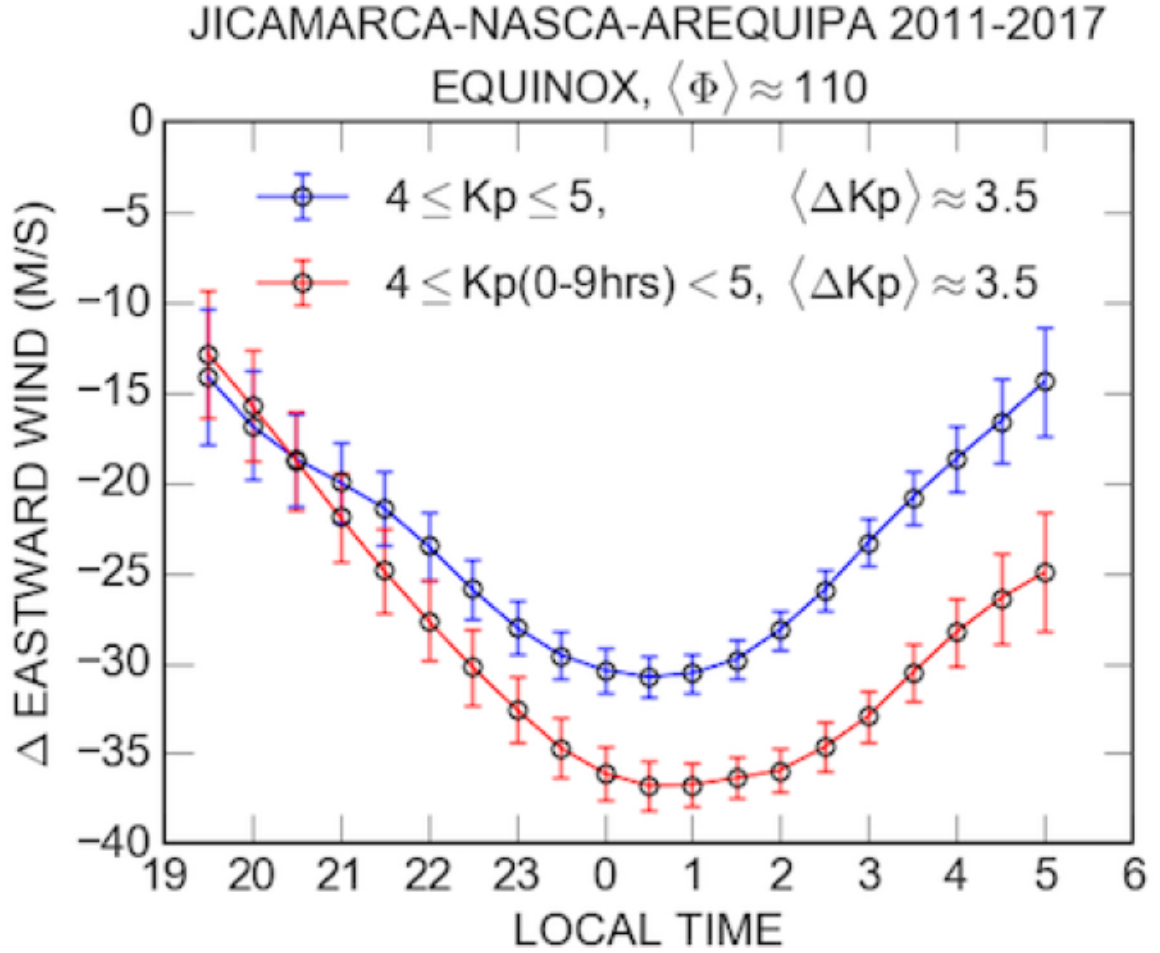


Figure. 4.9: Comparison of equinoctial disturbance eastward winds under local and extended geomagnetically active conditions. The error bars correspond to the standard errors of the means.

We have seen that the HWM14, which includes the disturbance component from the DWM07, gives reasonably good thermospheric wind estimates over Peru during geomagnetically active times even though both its quiet and disturbance components are less accurate. We will see below that these limitations become more severe during and shortly after large geomagnetic storms when the storm time winds depend strongly also on past geomagnetic activity levels. The importance of extended periods of enhanced geomagnetic activity is also evident in storm-time equatorial plasma drifts (e.g., [Fejer et al., 2005](#); [Scherliess &](#)



Fejer, 1997). In the next section, we will compare Peruvian thermospheric measured winds during and shortly after the 23-26 April 2012 and 07-10 May 2016 long-lasting geomagnetic storms with predictions from the HWM14 and from a simple empirical disturbance model.

#### 4.3.4 Case studies

Figure 4.10 shows the March-June zonal disturbance winds corresponding to 9-hours of enhanced geomagnetic activity, which was determined following the procedure described earlier. This extended disturbed wind pattern is similar to that shown in Figure 4.9 except for the slightly earlier time of the peak westward wind perturbation. We used this pattern to estimate the zonal wind disturbance winds for our two storms by linearly scaling their values to the corresponding local time dependent 9-hour Kp values. Therefore, our estimated zonal disturbance winds are given by

$$U(t, \bar{K}p(0 - 9hrs)) = U_q(t) + \frac{\Delta \bar{K}p(0 - 9hrs)}{3.1} d(t)$$

where U is the empirical zonal wind speed, t is the local time, U(t) is the corresponding 12-hour quiet-time zonal wind,  $\Delta \bar{K}p(0-9 \text{ hrs})$  is the average Kp enhancement over the last 9-hours over our quiet-time level (Kp=0.9), and d(t) is the disturbance wind shown in Figure 4.10. The predicted storm-time zonal winds are obtained by adding the disturbance winds scaled from the values shown in Figure 4.10 to the corresponding extended quiet-time values. The storm-time meridional winds were estimated using the local Kp indices.

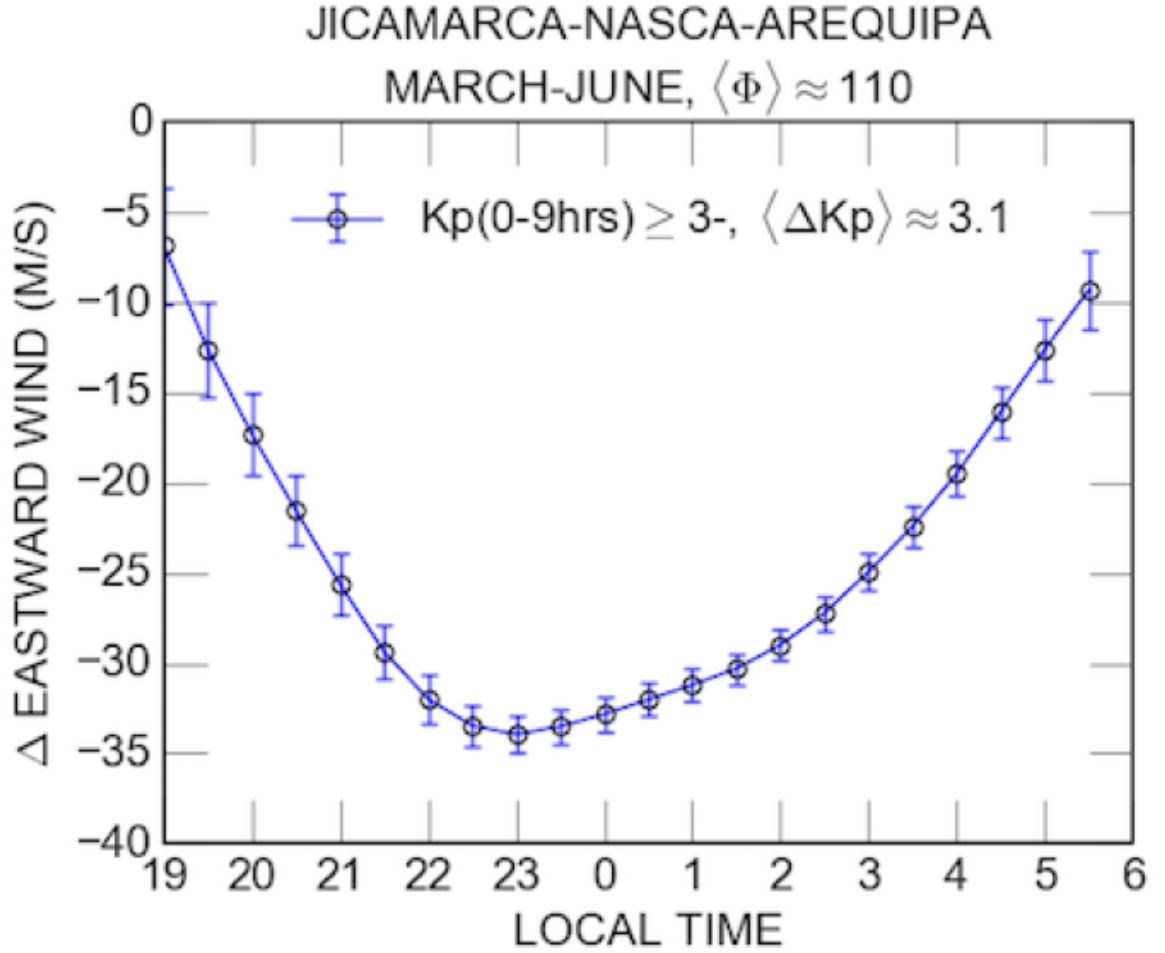


Figure. 4.10: Disturbance eastward winds of 9-hours extended geomagnetically active conditions for March-June period. Error bars correspond to the standard errors of the means.

Figures 4.11 and 4.12 show in the top panels the time evolution of the geomagnetic storm, as indicated by the Symmetric-H (SYM-H), Auroral Electrojet (AE) and Kp indices. The bottom panels show the zonal and meridional extended quiet-time reference winds, FPI measured zonal and meridional winds and the predictions from HWM14 and from our simple empirical model. Figure 4.11 shows that the main phase of the May 2016 storm lasted from  $\sim 20$  LT on the 7th to  $\sim 02:30$  LT on the 8th. This was followed by a highly active period of energy injections up to  $\sim 22$  LT on the 8th. In this period, the AE indices reached values of  $\sim 1900$  nT, and the Kp was about 6. This was followed by a long recovery

phase up to about May 10th with AE values of about 500 nT, and  $K_p \approx 2.5$ .

Figure 4.11 shows that, following a relatively large short-lived northward wind disturbance at about 00:30 LT on 8 May, the zonal wind first decreased and later reversed to westward with disturbance winds of up to about 70 m/s. On the following night, the westward disturbance winds were larger than about 60 m/s from about 22 LT to 05 LT, and there was a large southward disturbance wind near midnight. The zonal disturbance winds decreased to about 50 m/s and 30 m/s in the third night and fourth nights respectively and were largely confined to the postmidnight period. The meridional winds underwent a large short-lived postmidnight northward disturbance in the third night and essentially returned to their quiet time values in the fourth night. These short-lived interhemispheric surges are followed by the development of westward disturbances in agreement with the regulation of the meridional circulation through the development of westward disturbances (e.g., [Fuller-Rowell et al., 1994](#)).

Figure 4.11 shows that the HWM14 largely underestimates the magnitudes of the westward wind perturbations in the first night, and does not account for their occurrence in the following nights. Our simple empirical model provides significantly better estimates of the westward disturbance winds, but it underestimates their peak magnitudes in the third and fourth nights. The HWM14 and our model provide nearly identical estimates of the storm-time meridional winds, which is expected, since they are both based on the local  $K_p$  values, but they do not account for the large short-lived meridional disturbances near midnight.

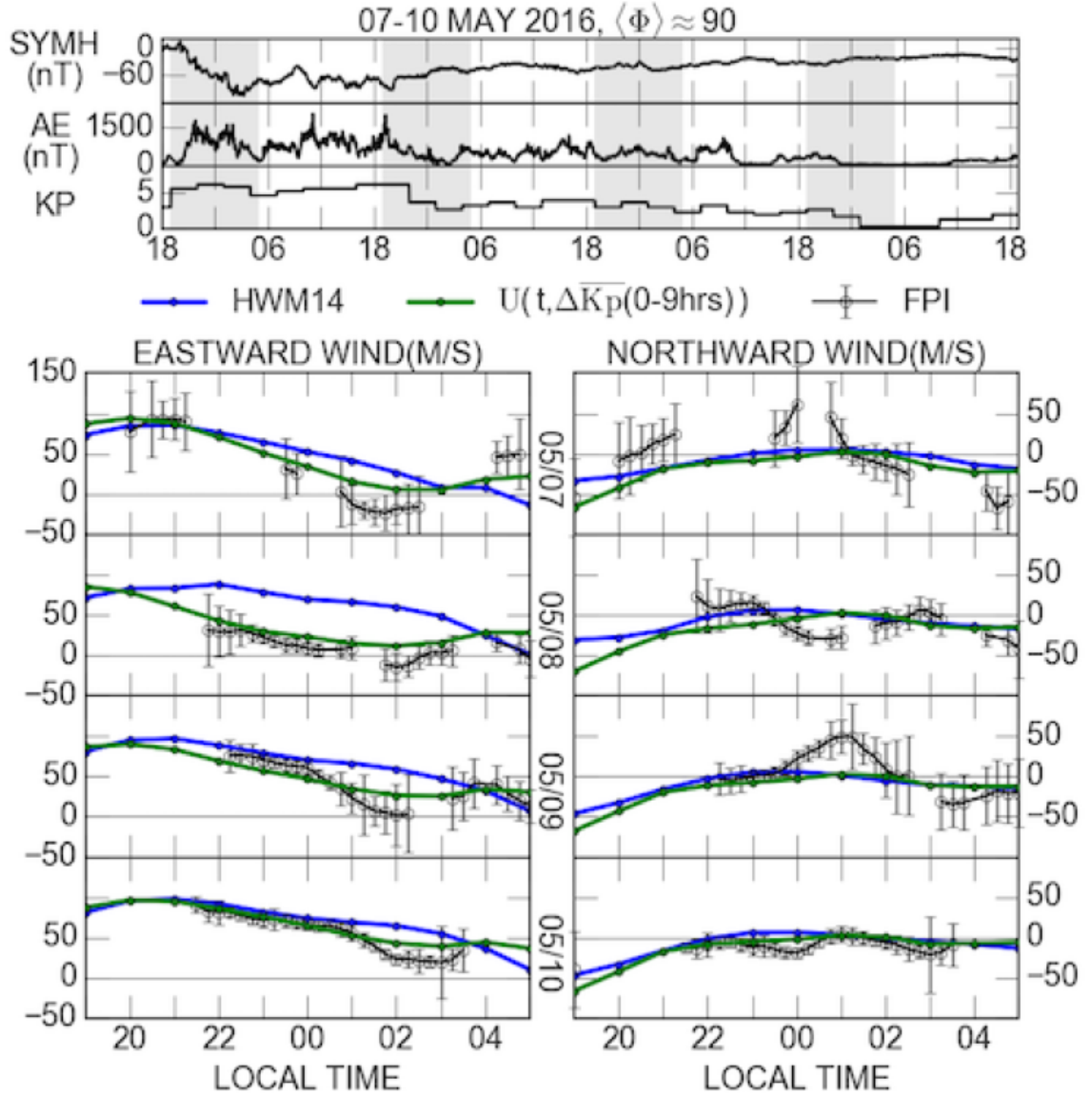


Figure. 4.11: Thermospheric wind response during the 07-10 May 2016 geomagnetic storm. (Top) Geophysical indices during the main and recovery storm phases of the geomagnetic storm. The shadowed areas indicate night-time periods. (Bottom) Eastward and northward quiet-time reference winds (black smooth lines), FPI observations (black lines with error bars), predictions from the HWM14 (blue lines) and from our empirical model (green lines). The error bars correspond to the standard deviations of the measured winds.

Figure 4.12 shows the geomagnetic indices during the April 2012 geomagnetic storm and the measured and model-estimated zonal and meridional winds. The main phase of this storm occurred from  $\sim 13$  LT to  $\sim 23$  LT on 23 April, and its recovery phase lasted for about three days. In the main phase, the peak AE was about 1500 nT and the average Kp was close to 5+. After the main phase there was a relatively short quiet-time period followed by 2 days of moderately disturbed conditions with an average AE of about 800 nT and an average Kp of  $\sim 4$ .

Figure 4.12 shows large (peak of about 50 m/s) westward wind disturbances starting in the storm main phase and extending into the following quiet-time period. In this case, the meridional winds underwent large northward and southward disturbances before and after midnight, respectively. In the second night, there were even larger (up to about 70 m/s) westward wind disturbances, particularly in premidnight period, while the meridional wind had northward disturbances increasing toward dawn. We note, however, that the premidnight measurements on the second night have much larger standard deviations due to less favorable observing conditions. The zonal wind disturbances decreased to about 30 m/s in the third night when they were confined to the postmidnight sector and essentially vanished in the fourth night. The meridional winds were slightly disturbed in the third night and also returned to their quiet values in the following night. The HWM14 predictions again underestimate the westward disturbances in the storm main phase, and do not account for their occurrence in the following nights. Our model reproduces the large westward disturbances in the storm main phase, but underestimates their values in the following nights, particularly in the second night. Again, these models do not reproduce the short-lived meridional wind disturbances.

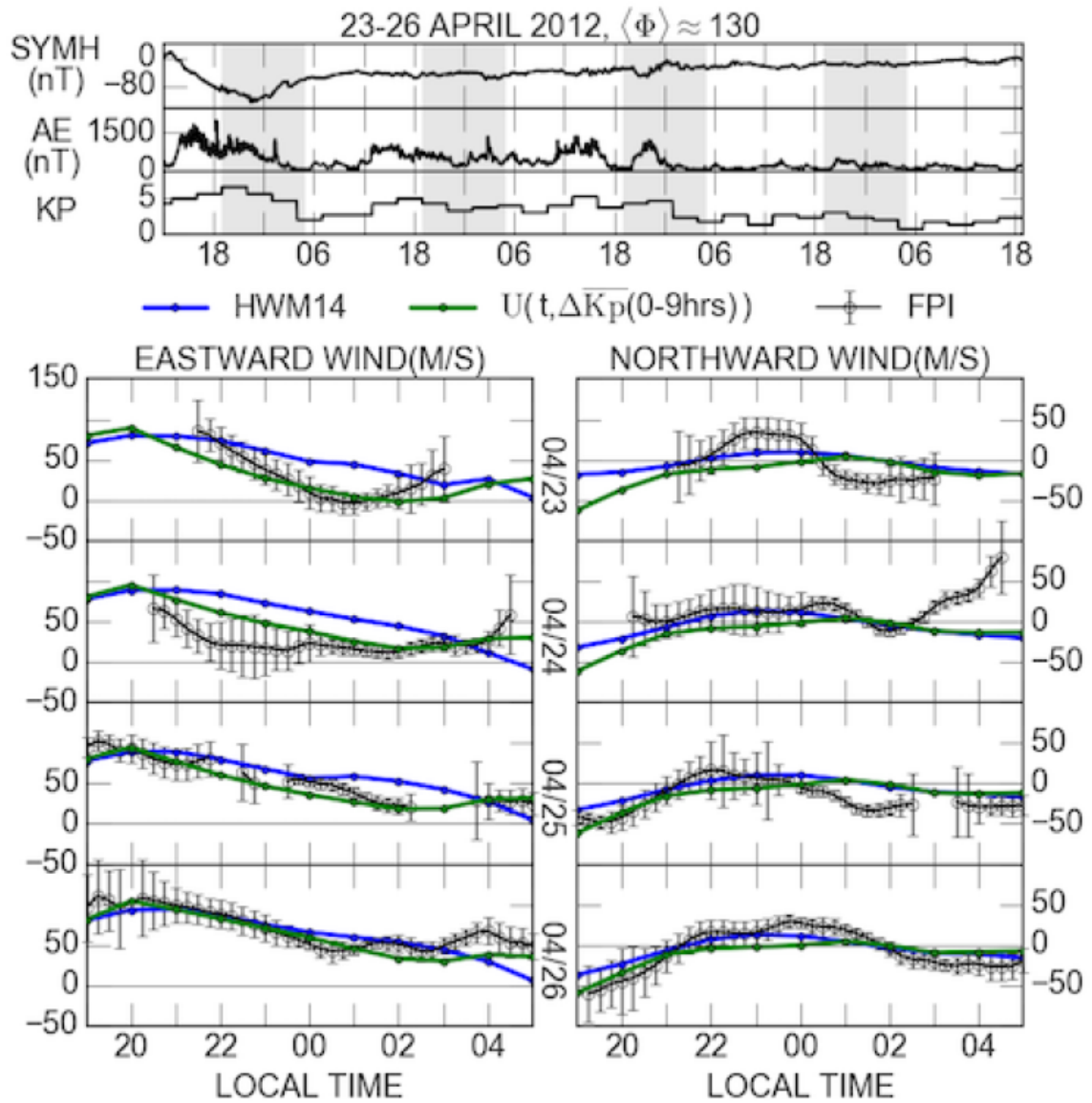


Figure. 4.12: Thermospheric wind response during the 23-26 April 2012 geomagnetic storm. (Top) Geophysical indices during the main and recovery storm phases of the geomagnetic storm. The shadowed areas indicate night-time periods. (Bottom) Eastward and northward quiet-time reference winds (black smooth lines), FPI observations (black lines with error bars), predictions from the HWM14 (blue lines) and from our empirical model (green lines). The error bars correspond to the standard deviations of the measured winds.

#### 4.4 Discussion

We have used multi-site FPI measurements in the Peruvian equatorial region and the novel data analysis technique presented by [Harding et al. \(2015\)](#) to determine for the first time the local time and seasonal dependence of the nighttime equatorial extended quiet and disturbed zonal and meridional winds, and compared them with predictions from HWM14 and DWM07. We have determined that the magnitudes of the equatorial nighttime eastward winds increase slightly from local to extended quiet conditions, and have used 12-hours extended quiet average winds as our baseline for inferring geomagnetic activity driven disturbance winds. Our extended zonal and meridional quiet-time climatologies are in good agreement with results from previous equatorial wind studies (e.g., [Biondi et al., 1990, 1999](#); [Meriwether et al., 2016](#)), and consistent with quiet-time F-region zonal plasma drifts (e.g., [Fejer et al., 1991, 2005](#)). They are also in general agreement with predictions from the HWM14, although this model tends to underestimate the Peruvian nighttime eastward winds.

We showed that the June solstice and equinoctial premidnight westward wind disturbances have comparable magnitudes and increase up to about midnight. Later, they decrease toward dawn and are largest during equinox and smallest during June solstice. The equinoctial and June solstice meridional disturbance winds are northward with comparable values in the premidnight sector and decrease monotonically from dusk to midnight where they reverse to southward. In the postmidnight sector, the southward disturbance winds increase toward dawn and have largest values during December solstice and smallest during equinox.

[Emmert et al. \(2004\)](#) presented longitudinally averaged disturbance zonal winds derived from climatological WINDII-UARS satellite measurements with peak magnitude around 03 LT, and showed that this peak moves to earlier local times with increasing geomagnetic activity. The DWM07 also predicts nighttime westward disturbance winds over Arequipa at 03 LT ([Emmert et al., 2008](#)). We note, however, that the FPI derived zonal disturbance winds over Arequipa presented in Figure 8 of the DWM07 study have larger values at

midnight than at 03 LT, consistent with our data. CHAMP satellite measurements showed strongest zonal wind disturbances around midnight during equinox and December solstice, and near 03 LT during June solstice (Xiong et al., 2015). Clearly, additional studies are needed to fully characterize the seasonal, solar cycle, and longitudinal variations of the equatorial disturbance winds.

We have seen that the DWM07 significantly underestimates, particularly near midnight, the magnitude of the nighttime zonal disturbance winds. Thermospheric wind measurements over the North African low latitude region during the 27-28 February 2014 storm showed that the DWM07 also significantly underestimated the nighttime westward disturbance winds near midnight (Malki et al., 2018). Our simple empirical model provides improved estimates of the storm-driven zonal perturbations for the two geomagnetic storms considered above. This is especially the case in the early phases of the storms. The model predictions for nights after the main phases could be improved by introducing a longer-term disturbance parameter. Fejer et al. (2005) showed that large westward postmidnight F-region disturbance dynamo drifts are also associated with time delays of about 15-24 hours after enhanced geomagnetic activity. Our database is not extensive enough for determining the possible effects of these longer-term disturbance parameters. The DWM07 and our model give reasonable estimates of the average meridional disturbance winds, but are unable to account for short-term disturbances; which are probably associated with large-scale trans-equatorial traveling atmospheric disturbances originated by energy depositions at polar regions with time delays of about 4 to 6 hours (Xiong et al., 2015; S.-R. Zhang et al., 2017; Malki et al., 2018). The use of shorter-term disturbance parameters would also improve the prediction of both zonal and meridional disturbance winds by taking time delay effects into account.

#### 4.5 Summary and conclusions

We have presented the first study of the local time and seasonal dependence of the nighttime equatorial disturbance winds over Peru. The disturbance winds are westward with largest magnitudes around midnight and strong seasonal dependence in the postmid-



night period. The equinoctial and June solstice premidnight meridional disturbance winds are northward and have comparable magnitudes. In the postmidnight sector, they are southward with larger values during December solstice and smallest during equinox. The DWM07 significantly underestimates the magnitudes of the nighttime equatorial zonal disturbance winds over Peru, particularly close to midnight. The zonal disturbance winds cannot be accurately predicted using only local disturbance parameters such as the 3-hour Kp indices. Time extended disturbance effects are particularly important during recovery phases of geomagnetic storms when significant postmidnight disturbance winds can last longer than 48 hours after storm main phases. The short-lived equatorial meridional disturbance winds cannot be accounted for with current empirical models.

## CHAPTER 5

### EQUATORIAL DISTURBANCE DYNAMO VERTICAL PLASMA DRIFTS OVER JICAMARCA <sup>1</sup>

#### 5.1 Introduction

The first theoretical description of the ionospheric disturbance dynamo process was presented by [Blanc and Richmond \(1980\)](#). They pointed out that enhanced energy deposition into the high latitude thermosphere (mostly through Joule heating) during geomagnetic storms produces significant disturbances in the thermospheric neutral wind field and conductivity distribution, which lead to large departures of the middle and low latitudes thermospheric neutral winds, ionospheric electric fields and currents from their quiet-time values.

The basic features of this mechanism consist of high latitude Joule heating driving a meridional thermospheric wind circulation and westward zonal winds that extend from high to low latitudes. These disturbance winds drive equatorward Pedersen currents that accumulate positive charges at the geomagnetic equator establishing a poleward electric field and eastward Hall currents. These currents build up polarization charges at the dawn and dusk terminators and set up a dusk-to-dawn electric field. This process gives rise to polar and equatorial anti-Sq current vortices. In the equatorial region, this process drives westward (eastward) current and F region downward (upward) plasma drift disturbances on the dayside (nightside), which reduce or reverse the quiet time drift and current patterns.

Equatorial disturbance dynamo plasma drifts and currents were the subjects of several studies. [Fejer et al. \(1983\)](#) used incoherent scatter radar vertical plasma drifts from the

---

<sup>1</sup>Most of this chapter is comprised of the original text from the research publication Navarro, L. A., Fejer, B. G., & Scherliess, L. (2019). Equatorial Disturbance Dynamo Vertical Plasma Drifts Over Jicamarca: Bimonthly and Solar Cycle Dependence. *Journal of Geophysical Research: Space Physics*, 124 (6), 4833-4841. <https://doi.org/10.1029/2019JA026729> with additional text and figures inside section 5.3. Reproduced by permission of the American Geophysical Union.

Jicamarca Radio Observatory ( $12^{\circ}$  S,  $76.9^{\circ}$  W; magnetic dip  $2^{\circ}$  N) in Peru to show that the equatorial vertical disturbance dynamo drifts were opposite to the normal quiet patterns in agreement with the Blanc-Richmond model. In this study, the time delay between the onset of high latitude energy deposition (inferred from AE indices) was consistent with the characteristic time for the establishment of a steady circulation pattern (e.g., [Richmond & Matsushita, 1975](#)). They also noted that for most storms, there is an inherent difficulty in the separation of equatorial disturbance dynamo and prompt penetration electric field (electrodynamic plasma drift) effects (e.g., [Fejer, 1997](#); [Wolf, 1995](#)).

[Mazaudier and Venkateswaran \(1990\)](#) studied the effects of the March 22, 1979 geomagnetic storm on middle and low latitude meridional winds and east/northward drifts using Saint Santin incoherent scatter radar and equatorial magnetic field measurements. They reported the generation of a meridional equatorward circulation one day after the onset of the storm, which appeared first at F-region altitudes and then descended to lower altitudes. They also observed northward electric fields from postmidnight to early afternoon. The time delay between the storm and the largest equatorial disturbances was about 15 hours. These results were also in agreement with the predictions from the Blanc-Richmond model.

[Fejer and Scherliess \(1995\)](#) used Jicamarca vertical drift observations and a binning technique to successfully separate prompt penetration and disturbance dynamo electric field effects. The derived disturbance dynamo disturbances were used to determine the time delays between geomagnetic activity enhancements, as indicated by AE indices, and the equatorial electrodynamic responses. They reported that the disturbance dynamo electric fields reach the equator 2-4 hours after the increase in high latitude magnetic activity. [Scherliess and Fejer \(1997\)](#) developed the first empirical model of equatorial disturbance dynamo vertical drifts using very extensive Jicamarca observations and AE indices. They showed that the disturbance dynamo vertical drifts are downward with small values during the day, and upward at night with largest magnitudes near sunrise. The time delays between the high latitude current enhancements and the corresponding equatorial disturbance dynamo disturbances are about 1-12 hours and 12-28 hours. The initial response is associ-

ated with fast traveling atmospheric disturbances, and the later response with changes in the thermospheric circulation and ionospheric composition (Fejer, 1997; Fejer et al., 2017; Fuller-Rowell et al., 2002).

Fejer (2002) showed that after 6 hours of enhanced geomagnetic activity, the Jicamarca disturbance dynamo downward drifts near dusk were larger during equinox than during June solstice. The postmidnight upward disturbances did not show much seasonal dependence. Jensen (2007) used global vertical drift measurements from the ROCSAT-1 satellite to show that the equinoctial downward disturbance dynamo drifts near dusk increase strongly from moderate to high solar flux conditions. Fejer et al. (2008b) used ROCSAT-1 satellite vertical drift measurements at an altitude of about 600 km to study the seasonal dependence of longitudinally averaged disturbance dynamo drifts resulting from 4 hours of enhanced geomagnetic activity. The evening downward dynamo drifts were largest during equinox and smallest during June solstice; the nighttime upward drifts were largest during December solstice and nearly identical during equinox and June solstice.

Measurements of F region height changes in the Indian equatorial region near dusk suggested that the largest disturbance dynamo vertical drifts occur about 0.5-4 hours and 16-23 hours after enhanced geomagnetic activity, and that the disturbance lifetimes decrease with increasing solar flux (Kakad et al., 2011). Storm-driven electrojet disturbances derived from magnetometer measurements in the Indian and Peruvian equatorial regions, presented by Yamazaki and Kosch (2015), showed that the disturbance dynamo effects are dominant during the recovery phase of geomagnetic storms. The disturbance dynamo currents in the Peruvian sector exhibit a semidiurnal variation, which resembles the pattern in Scherliess-Fejer empirical model (Fejer et al., 2017). The derived current disturbances increase with solar flux activity, most likely as a consequence of the increased ionospheric conductance. Pandey et al. (2018) reported that the largest disturbance dynamo effects on the equatorial electrojet over India occur during equinox and high solar activity periods.

Fejer and Emmert (2003) used incoherent scatter radar observation from Jicamarca and Arecibo and wind measurements from the Upper Atmospheric Research Satellite (UARS)

for the first detailed study of low latitude disturbance dynamo effects during the recovery of a major geomagnetic storm. These observations showed large latitudinal variability of the disturbance drifts. They also reported that although the characteristics of the measured disturbance dynamo drifts were generally consistent with climatological and theoretical patterns, their amplitudes were initially much larger than the expected values. [Xiong et al. \(2016\)](#) used CHAMP and ROCSAT-1 satellite observations to study the local time and longitudinal dependent response of the equatorial electrojet, vertical plasma drifts and zonal winds to the solar wind parameters using the 3 hours integrated merging electric fields proposed by [Newell et al. \(2007\)](#) to represent the energy input to the magnetosphere-ionosphere-thermosphere system. They showed that the nighttime disturbance dynamo drifts are upward and have the largest magnitudes in the postmidnight sector after 4.5 hours and gradually decrease to their quiet time values after 24 hours. The daytime disturbance drifts are downward and small in agreement with results from earlier studies. [R. Zhang, Liu, Le, Chen, and Kuai \(2017\)](#) examined the storm-time evolution of middle and low latitude ionosphere disturbance dynamo drifts during three long-lasting geomagnetic storms using ROCSAT-1 and C/NOFS satellite measurements. They showed that the local time dependence of the equatorial disturbance dynamo vertical drifts can be affected by the shift of the disturbance winds to later local times.

[C. M. Huang and Chen \(2008\)](#) and [C. M. Huang \(2013\)](#) used the National Center for Atmospheric Research Thermosphere Ionosphere Electrodynamics General Circulation Model NCAR/TIE GCM to study seasonal and solar cycle dependence of the equatorial disturbance dynamo vertical plasma drifts. These simulations reproduced the observed decrease of the magnitudes of the disturbance dynamo drifts with decreasing solar flux, and the occurrence of larger magnitudes during equinox than during June solstice.

In this study, we use extensive vertical plasma drifts observations from the Jicamarca Radio Observatory incoherent scatter radar to examine in more detail the bi-monthly, solar cycle and geomagnetically active condition dependence of the equatorial disturbance dynamo vertical plasma drifts. We show that these drifts have strong solar cycle and

bimonthly variations. In the following sections, we first describe our database and then present and discuss our results.

## 5.2 Data and Methodology

The vertical plasma drifts used in this study were obtained from incoherent scatter radar measurements at the Jicamarca Radio Observatory from April 1968 to February 2018. The experimental procedure was described by [Woodman \(1970\)](#). The data acquisition and signal processing techniques were described by [Kudeki et al. \(1999\)](#). The drifts were measured usually at altitudes from about 250 to 800km with a height resolution of 20-45km and with an integration time of 5 min. These measurements are available at the Jicamarca website. The values used in this study represent 15-min averages at altitudes from about 250 to 400km, where the signal to noise ratios are highest. However, during periods of strong equatorial spread F, the height range of drift was extended sometimes up to 850km to minimize the effects produced by these echoes. The error of these measurements is about 1m/s during the day and somewhat larger at night.

We used 10525 hours of drift measurements and complementary AE and decimetric solar flux indices. We have initially determined the quiet-time values that will be later removed to obtain the disturbance associated with the geomagnetic activity effects.

We used the solar cycle dependent bimonthly baselines derived by [Scherliess and Fejer \(1997\)](#) for every two weeks. Figure 5.1 shows these quiet values for bimonthly bins and binned averages which represent 30-hours of geomagnetically quiet conditions as expressed by the average of hourly AE indices smaller than 300nT. These criteria were established to suppress the short- and long-term disturbances associated with wind-driven disturbance dynamo electric fields. Their standard errors of the means of about 2 m/s correspond to an average AE of about 130 nT.

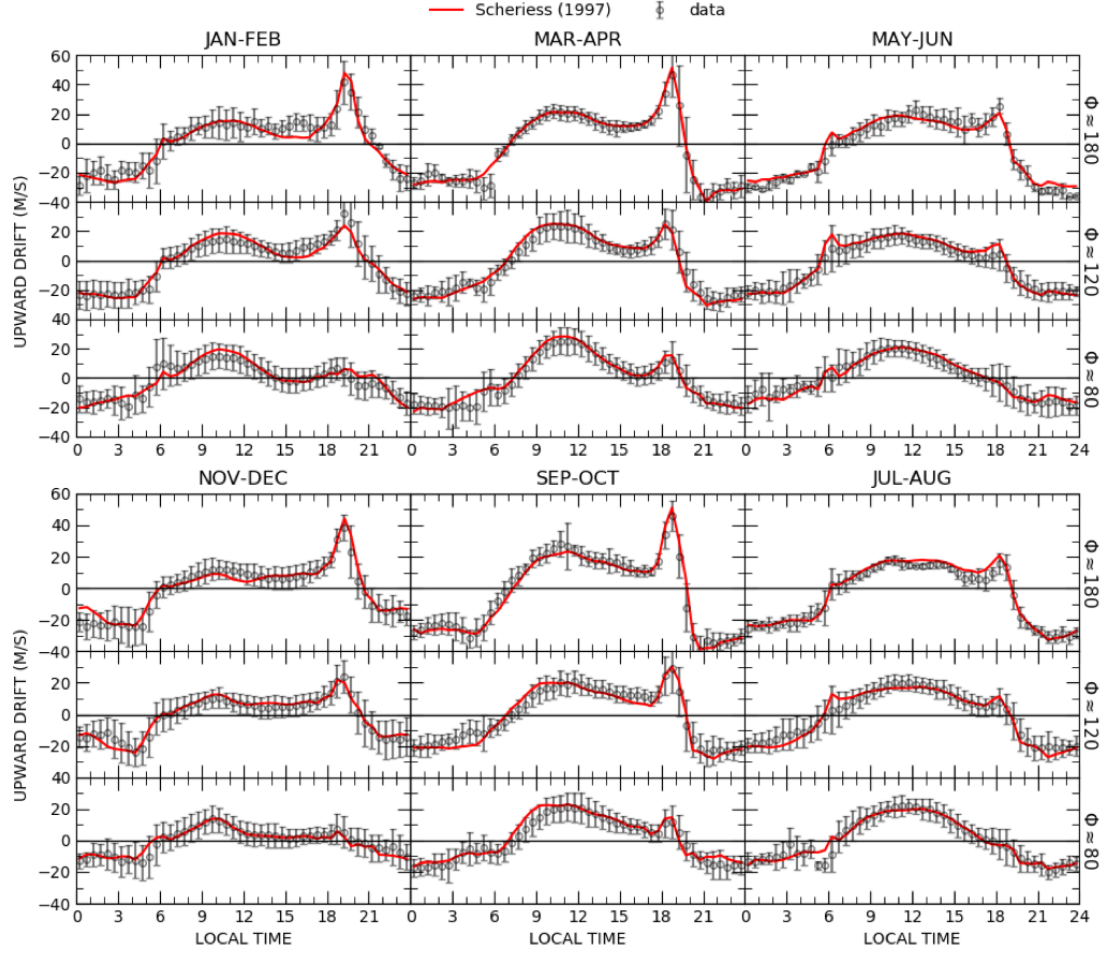


Figure. 5.1: Comparison of the bimonthly half-hourly averaged vertical drifts and predictions from [Scherliess \(1997\)](#). Errorbars correspond to standard deviations.

We have determined the disturbance dynamo vertical drifts by removing the corresponding solar cycle dependent quiet time values. These quiet values were removed from the 15-min averaged drifts. Then, we follow [Fejer and Scherliess \(1995\)](#) and [Fejer et al. \(2008b\)](#), we selected the disturbance drifts following an average increase in the last 6 hours of geomagnetic activity of at least 100 nT in AE relative to the quiet value mentioned before i.e.  $\Delta \text{AE}(0-6 \text{ hrs}) > 100 \text{ nT}$ , and minimized prompt penetration electric fields effects by excluding disturbance drifts when the hourly AE changes were larger than 250 nT i.e. when the absolute differences of both the current and the previously hourly value and the previ-

ously hourly value and the value two hours before were larger than 250 nT. We note that it is not possible to completely separate prompt penetration and disturbance dynamo electric field effects. Since these processes have opposite local time dependent polarities (e.g., [Fejer, 2011](#)), we estimate that, on the average, residual prompt penetration electric fields effects decrease the magnitudes of our inferred disturbance dynamo drifts only slightly (by about 2-3 m/s). We also tested other more stringent criteria to further minimize these magnetospheric effects with no significant differences in the results. We have deleted observations related to the solar flare events (e.g., [R. Zhang, Liu, Le, & Chen, 2017](#)).

Our database of disturbance drifts consists of 3118 hours of vertical drift observations. Table 5.1 shows the number of hours of vertical disturbance drifts in bimonthly bins. The smallest number of observations is from November-December with 374 hours, and the largest number from September-October with 700 hours. In general, they have fairly even distributions from low and high solar flux conditions. This is also the case for the disturbance levels, as measured by the time averaged AE indices, except for the July-August high solar flux period, where the average disturbance levels are smaller than during the other periods.

Table 5.1: Bimonthly Distribution of the Jicamarca Vertical Disturbance Drifts

	Jan-Feb	Mar-Apr	May-Jun	Jul-Aug	Sep-Oct	Nov-Dec
Number of hours	386	644	544	470	700	374

### 5.3 Results

Figure 5.2 shows the local time and seasonal distribution of our disturbance dynamo drifts. We note that these disturbance drifts include quiet time variability effects, which are largest during low solar flux periods (e.g., [Fejer & Scherliess, 2001](#)), since these cannot be removed by subtracting average quiet time values. The relatively small number of nighttime measurements during December solstice is mostly due to the frequent occurrence of equatorial spread over the entire nighttime period during this season (e.g., [Fejer et al., 1999](#)) and to the removal of measurements during sudden stratospheric warming events (e.g., [Fejer et](#)



al., 2011; Siddiqui et al., 2015).

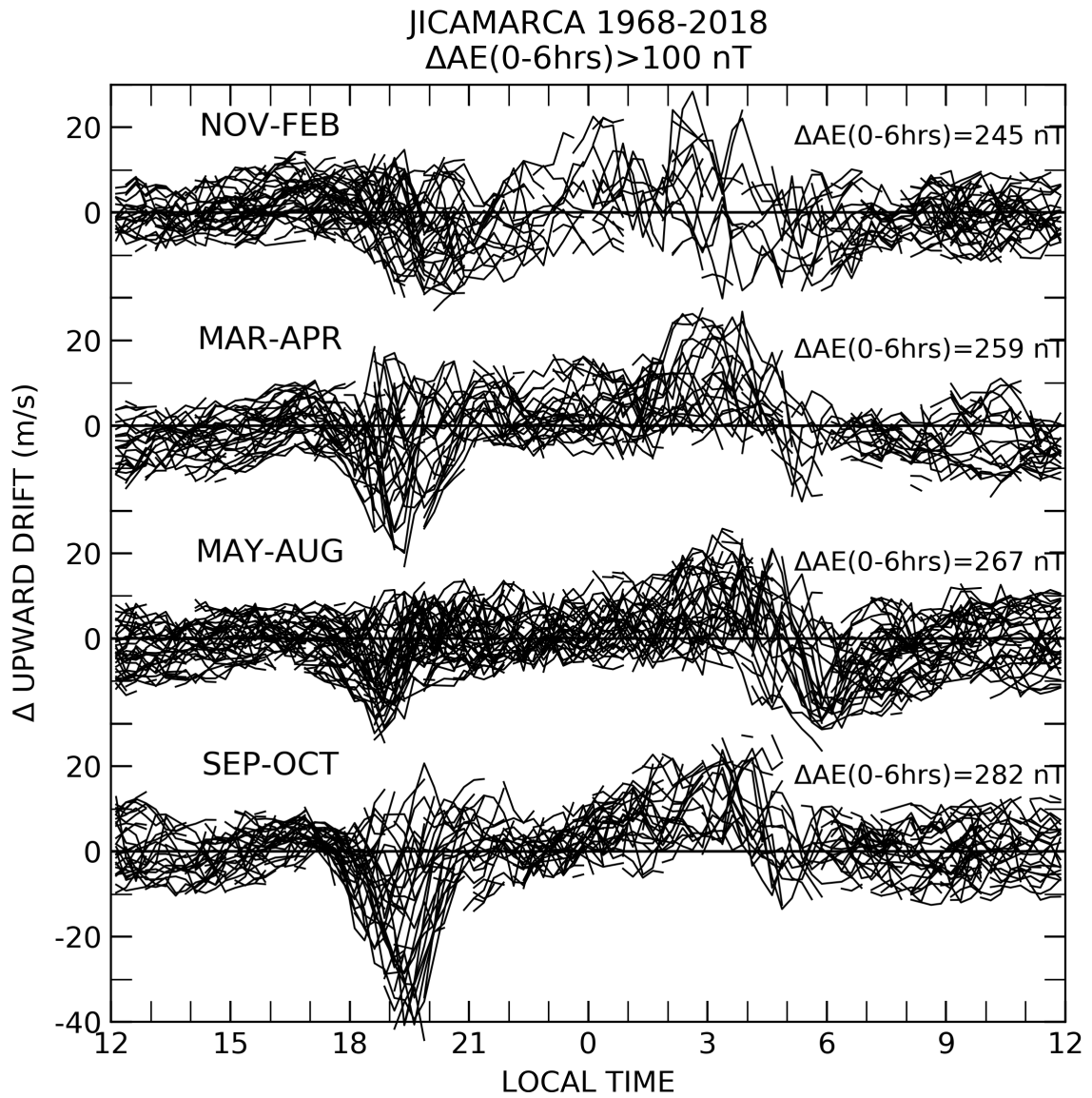


Figure. 5.2: Scatter plot of season dependent disturbance dynamo drifts after 6 hours of enhanced geomagnetic activity.

Figure 5.3 shows the bimonthly averaged disturbance vertical drifts corresponding to 6-hours of enhanced magnetic activity and to an average solar flux index of about 120 units.

For the November-December and January-February bins, we have included measurements 15 days before and after these nominal periods to overcome low statistics. The average increases in the 6-hours AE indices over our quiet time value (about 130 nT) varied from 230nT to 260nT, except for January-February, which had an average increase of about 180nT. The residuals were averaged in hourly bins, except around sunset where half-hour bins were used. The standard deviations on the average disturbance drift varied from about 3 m/s to 10 m/s, except for the December solstice nighttime data where it was up to about 15 m/s.

Figure 5.3 shows that the daytime drifts are typically downward with values of about 5 m/s from January to June, and close to zero for the rest of the year. Near dusk, the disturbance drifts are downward throughout the year with largest values during the autumnal equinox and smallest during May-June. The evening disturbance dynamo downward peak drifts, and the reversals from downward to upward drifts, occur earliest during May-June and latest during January-February. There is a clear equinoctial asymmetry in the disturbance dynamo drifts near dusk with autumnal equinoctial values about twice as large as the vernal equinoctial values. The nighttime disturbance drifts are upward throughout the year with smallest values during May-June. The magnitudes of the December solstice nighttime disturbance drifts have much larger uncertainties than during the other seasons due to poor statistics. The morning drift reversals from upward to downward occur latest during December and earliest during June solstice.

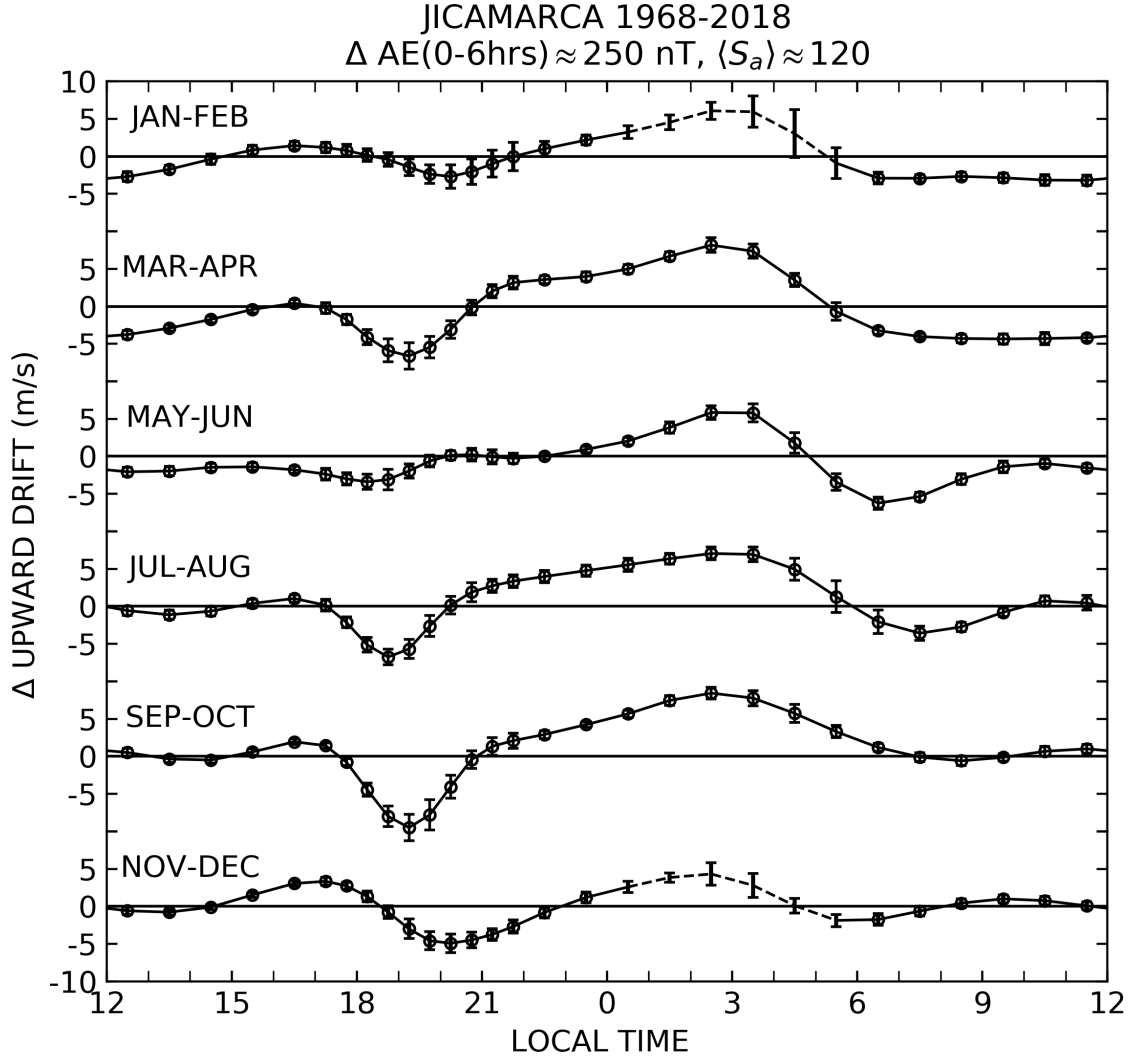


Figure. 5.3: Bimonthly averages of disturbance vertical drifts for moderate flux conditions. The error bars denote the standard errors of the means. The dotted lines denote periods of low statistics.

Figure 5.4 shows a color map of the annual variation of the disturbance dynamo drifts for moderate solar flux conditions. It is an extension of the results shown in Figure 5.3 using a sliding bimonthly window every two weeks. This window was one month longer

for December solstice when less data was available and, as a result, it is often difficult to estimate accurately the disturbance drifts due to the frequent occurrence of plasma irregularities and strong sudden stratospheric warming events. In this case, the average disturbance increases over the quiet value (about 130nT) ranged from 200nT to 290nT, except from mid November to mid February when they ranged from about 170nT to 190nT. The average solar flux conditions ranged from 110 to 130 solar flux units. The overall standard deviations are comparable to those reported in Figure 5.2 (i.e., between about 5 and 10 m/s and somewhat larger, especially at night, during December solstice).

Figure 5.4 shows in more detail the strong annual variation of the equatorial disturbance dynamo vertical drifts. The magnitude and peak times of the downward drifts near dusk, in particular, change strongly throughout the year. These peak drifts are largest around the autumnal equinox and smallest around June solstice. There is also a pronounced asymmetry on the equinoctial drifts near sunset where the downward disturbance drifts are larger during the autumnal equinox than during the vernal equinox. The same is true for the late night upward drifts. In addition, the postmidnight upward disturbance drifts extend further into the dayside during the autumnal equinox than during the vernal equinox. The daytime and nighttime disturbance drifts are smallest during May-June, except near sunrise. There is also an apparent annual variation on the morning disturbance drifts, which are generally downward from December to July, and close to zero for the rest of the year. Except for June solstice, the late afternoon drifts are upward with largest values around December solstice.

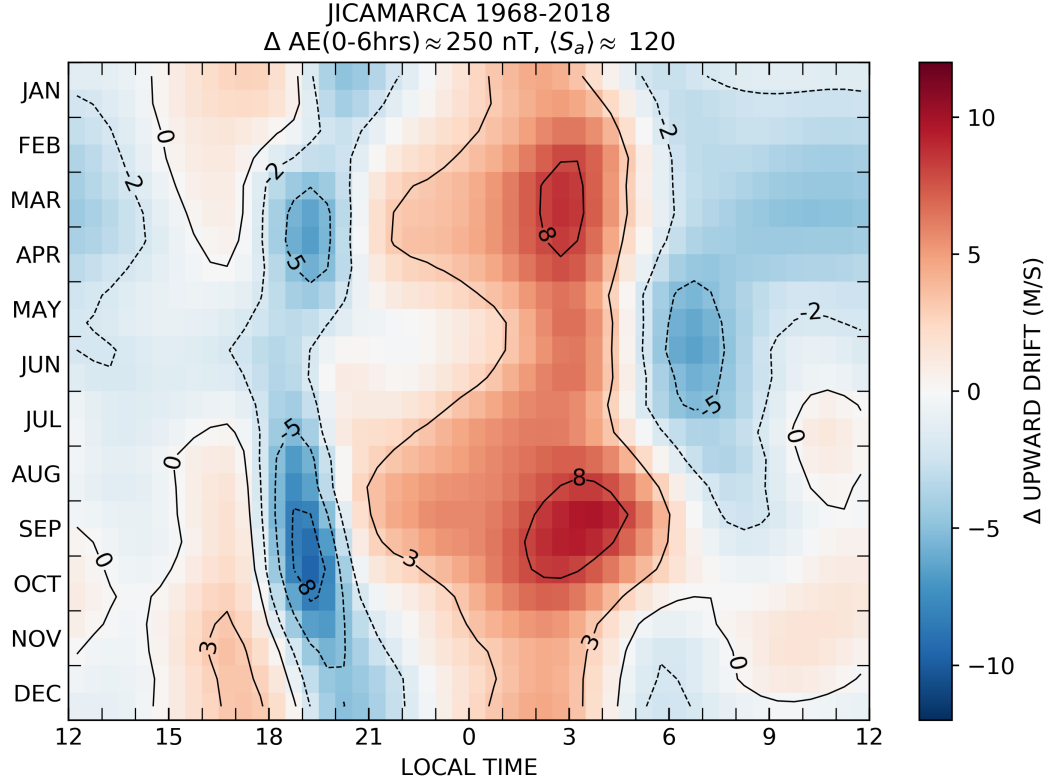


Figure. 5.4: Annual variation and local time dependence of disturbance vertical drifts for moderate flux conditions.

The equatorial disturbance dynamo drifts vary strongly with the level of energy deposition into the high latitude ionosphere, as measured by the time-averaged AE indices, and with solar flux. Figure 5.5 illustrates the annual and local time dependent increases of the disturbance dynamo drift magnitudes for an increase in the time-averaged AE indices by about 270 nT for moderate solar flux conditions. In this case again, we combined the results from November to February in order to obtain statistically more meaningful results. Figure 5.5 shows that increased geomagnetic activity leads to large increases in the magnitudes of the disturbance drifts near dusk and in the late night sector, with no significant effects on the daytime drifts. The downward disturbance drifts near dusk increase strongly during the equinoctial months and very weakly between May and August. The rate of increase of

the nighttime upward disturbance drifts is largest near 03 LT and does not change much throughout the year.

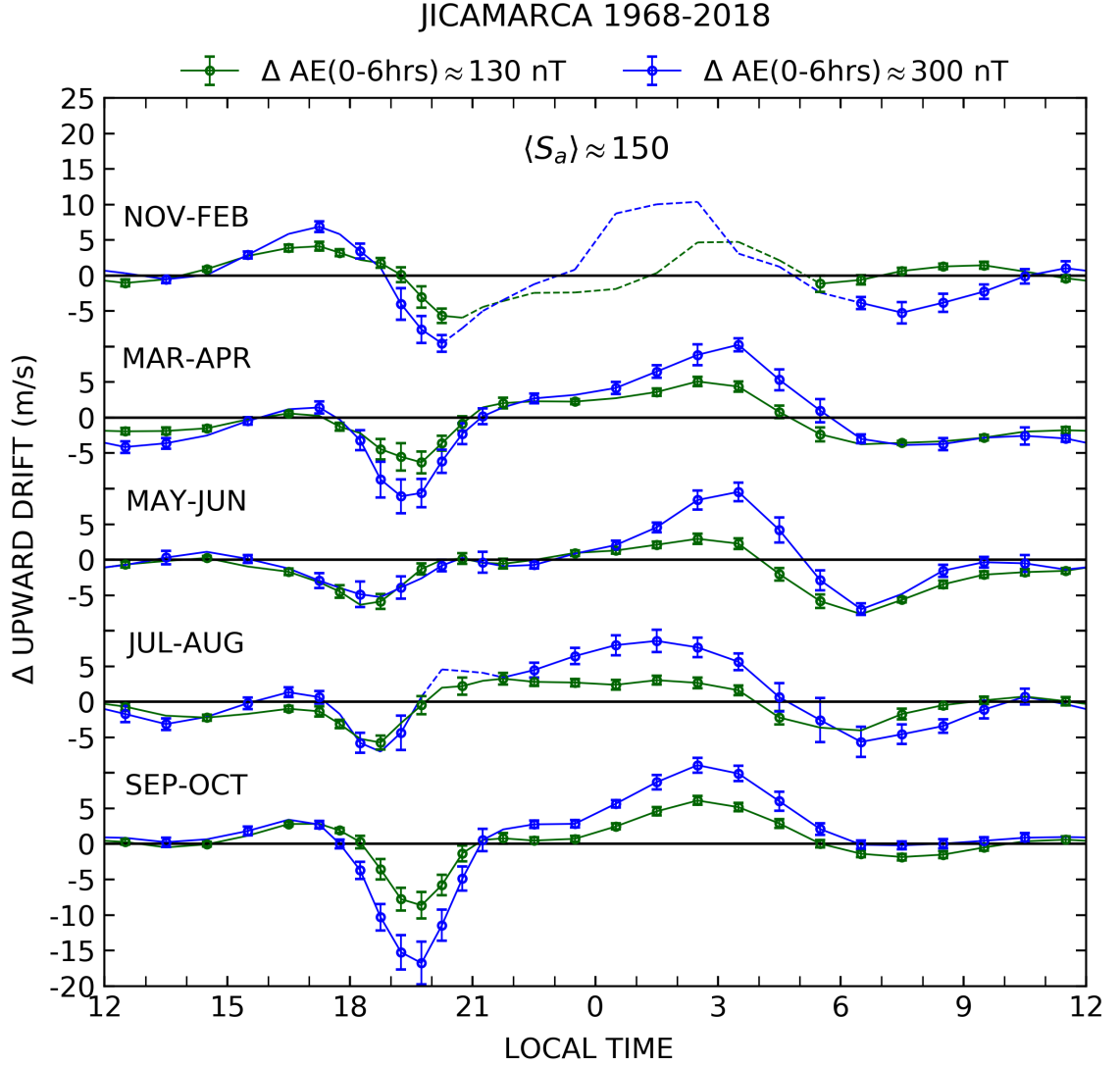


Figure. 5.5: Annual variation of the disturbance dynamo vertical drifts for low (green) and high (blue) magnetically active conditions. The scatter bars denote the standard errors of the means. The dotted lines indicate periods of low statistics.

Figure 5.6 shows the annual variation of the disturbance drifts with solar flux. We

used three solar flux levels only near dusk where they vary most strongly with solar flux, and have omitted the high solar flux results for July-August since they are not statistically significant due the small number of observations. These average disturbance drift patterns were obtained by binning the data in variable overlapping solar flux ranges. The resulting average values ranged from 90 to 100 s.f.u. and 175 to 185 s.f.u. for low and high solar flux conditions respectively, except for November-February high solar conditions when this value was 150 s.f.u. The 6-hour average increase in the AE indices ranged from about 240 nT to 250nT for low solar flux conditions, and from about 260 nT to 270 nT for medium and high solar conditions respectively, except for Nov-Dec where the average increase was about 200nT. The standard deviations were generally about 5 m/s for the daytime and premidnight sectors, and about 8 m/s for the rest of the day. These standard deviations were smallest for May-June and largest for November-December.

Figure 5.6 shows that the strongest solar cycle effects on the disturbance dynamo drifts occur near sunset. In this local time sector, the downward disturbance drifts increase with solar flux during all seasons and have largest increases during equinox. The high solar flux evening peak disturbance drifts in Figure 5.6 are largest and smallest during September-October and May-June with values of about -20 m/s and -5 m/s, respectively. The evening peak of the disturbance drifts also shift to later local times from low to high solar flux periods. The low solar flux disturbance drifts near sunset are typically smaller than about -5 m/s for all seasons, and have largest magnitudes during the autumnal equinox. The nighttime upward disturbance drifts generally do not change much with solar flux. The solar flux dependence of the December solstice nighttime drift cannot be determined from our limited data. The morning westward drifts generally decrease weakly with increasing solar flux, particularly during June solstice, and the late afternoon drift becomes increasingly eastward prior to turning downward.

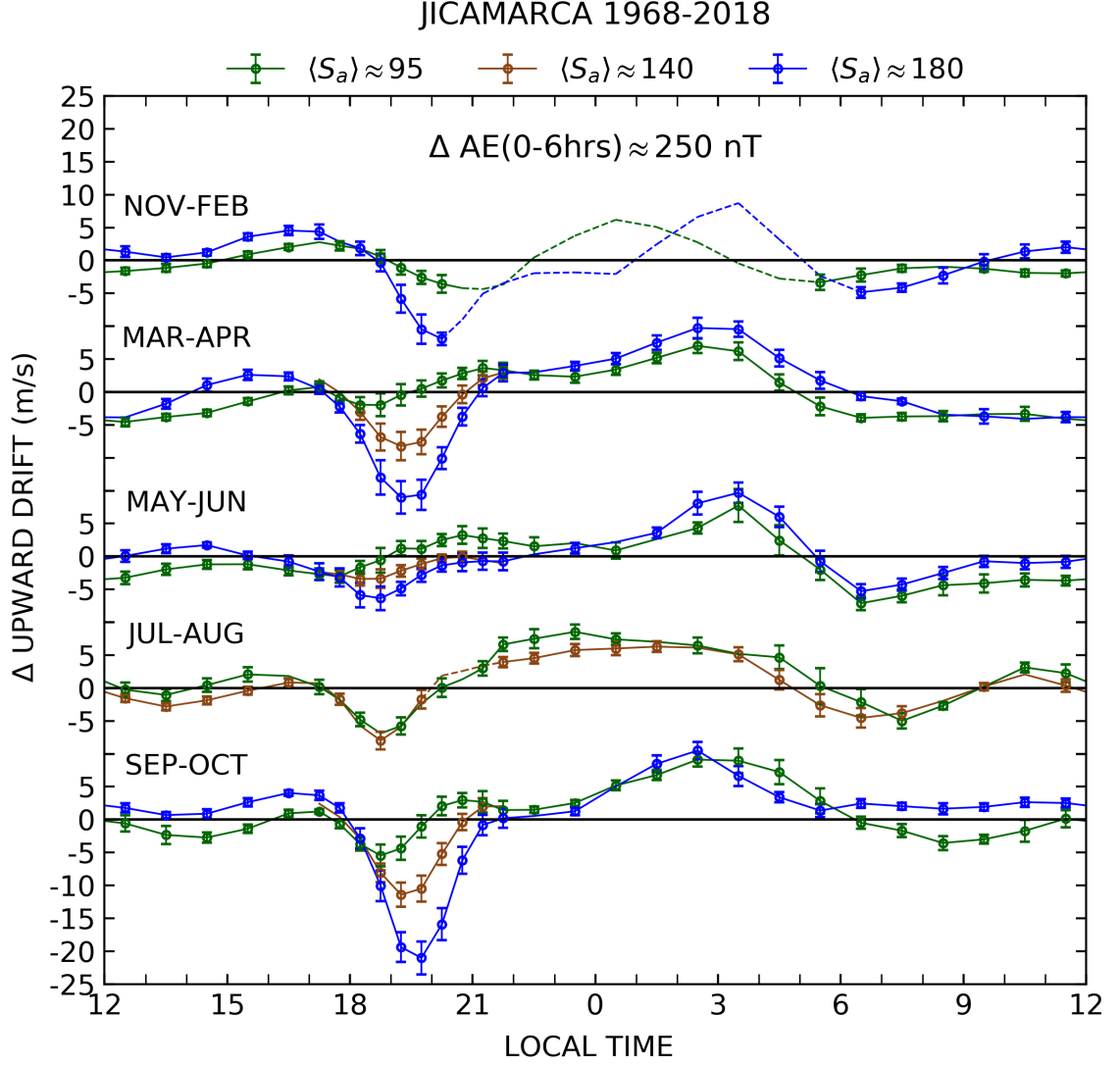


Figure. 5.6: Annual variation of disturbance dynamo vertical drifts for low (green) and high (blue) solar flux conditions. The scatter bars denote the standard errors of the means. The dotted lines indicate periods of low statistics.

#### 5.4 Discussion

We have determined the bi-monthly variation of the Jicamarca disturbance dynamo vertical drifts and their dependence on solar flux following a 6-hours AE increase of 250 nT. For moderate solar flux conditions, the daytime disturbance drifts are smaller than about



5 m/s and generally downward, except in the late afternoon sector. Near dusk, they are downward with largest and smallest magnitudes during the autumnal equinox and May-June, respectively. The early night drift reversal times from downward to upward occur earliest during May-June and latest during January-February. The nighttime disturbance drifts are upward with largest magnitudes (about 8 m/s) close to sunrise and vary weakly with season, except for slightly smaller values during May-June. The disturbance drifts reverse from upward to downward near dawn.

Our disturbance drift patterns are in good agreement with the patterns from the Blanc-Richmond numerical and the season independent Scherliess-Fejer empirical model. The seasonal variations of the disturbance drifts presented above are consistent with the results from previous (less detailed) empirical (e.g., [Fejer, 2002](#); [Fejer et al., 2008b](#)) and numerical simulation studies (e.g., [C. M. Huang & Chen, 2008](#); [C. M. Huang, 2013](#)). However, our results show a much stronger variation of the disturbance dynamo drift throughout the year, with solar flux and geomagnetic conditions than reported previously. In particular, our data indicate very weak low solar flux disturbance dynamo effects near dusk between about March and June.

The disturbance dynamo drifts vary most strongly with solar flux near dusk, but this dependence changes significantly throughout the year. In this local time sector, an increase in the solar flux index from about 90 to 180 s.f.u. results in an increase of the peak downward drift from 5 to 20 m/s during for September-October, but only from about 3 to 5 m/s during May-June. Although our average disturbance drifts are less accurate during December solstice, they also indicate a strong increase of the peak downward drift with solar flux. Similar annual variation is found for increased geomagnetic activity, but with no shift to later local times.

The evening disturbance dynamo drifts have larger values during the autumnal equinox than during the vernal equinox, particularly during low solar flux conditions. [Scherliess \(1997\)](#) showed that there is a similar equinoctial asymmetry on the Jicamarca quiet time evening upward prereversal velocities with larger values during the autumnal equinox. [Ren](#)

[et al. \(2011\)](#) used ROCSAT-1 satellite data to describe the longitudinal variation of this equinoctial asymmetry under quiet time conditions, which was attributed to the action of asymmetries on different thermospheric parameters, especially in the eastward winds and in the tides related to them.

The morning and early afternoon disturbance dynamo drifts, which are predominantly downward during low solar flux periods, decrease and even turn slightly eastward during high solar flux conditions. The nighttime upward disturbance drifts do not change much from low to high solar flux periods, but they increase strongly with geomagnetic activity close to dawn. These drifts also do not change much with season, except perhaps for the early night period. The relatively large late night upward disturbance dynamo drift and the decrease of the nighttime quiet-time ambient downward vertical drifts with solar flux, makes the disturbance dynamo drifts an increasingly important driving mechanism for equatorial spread F during low solar flux geomagnetic active periods (e.g., [Fejer et al., 1999](#)). The same is the case near dusk during July-August (e.g., [Rodrigues et al., 2018](#)).

The physical processes responsible for the strong dependence of the equatorial disturbance dynamo on season and solar flux have not been studied in detail. Simulations studies presented by [C. M. Huang et al. \(2005\)](#), [C. M. Huang and Chen \(2008\)](#) and [C. M. Huang \(2013\)](#) suggest that the disturbance dynamo electric fields are largely controlled by the same main parameters (e.g., thermospheric winds and ionospheric conductances) that are responsible for the quiet time drifts. [C. M. Huang \(2013\)](#) pointed out that an asymmetric energy deposition at high latitudes may also play an important role, even during equinox, but these effects have not been studied using numerical simulations.

## 5.5 Summary and conclusions

We have presented the first detailed study of the bi-monthly, solar cycle and enhanced geomagnetic conditions dependence of the disturbance dynamo vertical drifts over Jicamarca. Our results indicate that the equatorial disturbance dynamo drifts can have much stronger seasonal and solar cycle variations than previously reported. The daytime vertical disturbance dynamo drifts have small magnitudes and an apparent annual dependence, with

largest downward disturbances around March-April. Near dusk, the disturbance drifts are downward and show pronounced equinoctial asymmetry with larger values during the autumnal than during the vernal equinox. These drifts increase strongly with both solar flux and enhanced geomagnetic activity but shift to later local times with increasing solar flux only. They reach much larger magnitudes than predicted by the Scherliess-Fejer empirical disturbance drift model, particularly during equinox solar maximum periods. Nighttime disturbance dynamo drifts are upward with large magnitudes in the postmidnight sector, have no significant solar cycle or seasonal dependence, except during the early night period.

## CHAPTER 6

### STORM-TIME COUPLING OF EQUATORIAL ZONAL PLASMA DRIFTS AND NEUTRAL WINDS

#### 6.1 Introduction

In this chapter we will compare the thermospheric zonal winds and ionospheric zonal drifts with a stronger emphasis on storm-time conditions. We will start briefly describing our zonal drifts database. Later, we will compare the climatologically averaged zonal drifts and winds for quiet- and storm-time conditions. We will finally show storm-time coupling between drifts and winds under large disturbance dynamo effects and, for the first time, under the action of penetration electric fields for two storm cases.

The ionospheric plasma and the thermospheric winds have an intimate relationship. They feedback each other dynamics through different processes like collisions and polarization electric fields (Rishbeth & Garriot, 1969; Kelley, 2009). Many of these coupled dynamics and electrodynamics during quiet time conditions have been extensively studied theoretically and empirically and, therefore, are fairly well understood (Rishbeth, 1971b, 1971a; Heelis, 2004; Kelley, 2009). However, few storm-time studies have studied their coupled dynamics during equatorial disturbance dynamo and prompt-penetration electric field events (Fejer & Emmert, 2003; Santos et al., 2016). The generation mechanism of these disturbances and their effects have been described separately in chapters 3, and 4 and 5 respectively. In this chapter, we will focus on climatological and storm cases studies of their coupled dynamics.

The night-time equatorial zonal plasma drifts and neutral winds coupling is strongly related to the development of polarization electric fields, which also depends on the ionospheric conductivity conditions. The F-region zonal plasma drifts are primarily driven by F-region neutral winds and their magnitudes are dependent on the E- and F-region Peder-

son conductivities. At early night, these conductivities are comparable near solar minimum preventing the full buildup of the F-region polarization electric fields leading to significantly smaller zonal plasma drifts than the corresponding zonal neutral winds. For the postmidnight hours, the descent of the F-region peak produces an increment of the E- to F- region conductivity ratio which improves the coupling between the winds and drifts especially during summer and equinoxes. Similarly, this coupling improves for higher solar flux conditions which increments this conductivity ratio (Biondi et al., 1988; Fejer, 1993).

Several studies have used equatorial plasma drifts and neutral winds from radars and optical instrumentation in Peru. Biondi et al. (1988) used Arequipa FPI and Jicamarca ISR observations and showed stronger coupling at late night and that the correlations of their motions is related to the decay of the E-region conductivity leading to the F-region wind dynamo to control over the F-region ionospheric drift. Chapagain et al. (2013) used FPI winds from Jicamarca and Nasca along with zonal drifts from the Jicamarca ISR and found that there was a general agreement between them of  $\sim 60\%$  and  $\sim 80\%$  of total of events at early night and in the postmidnight sector, respectively. They also found that the nighttime zonal winds are generally stronger than the drifts in the premidnight sector; later the winds and drifts have comparable magnitudes. In the postmidnight sector, the zonal drifts were larger than the zonal winds in about 15% of total of events. Valladares et al. (2002) also found a general good agreement between Arequipa FPI zonal winds and the scintillation drifts from Ancon, Peru, except for low flux conditions when the drifts were larger than the winds for about 10 m/s. Coley et al. (1994) suggested that vertical shear in the equatorial zonal neutral wind below 250 km would generate additional polarization electric fields to allow the zonal drifts to exceed the winds above 250 km. Other campaign and simulation studies also reached to similar conclusions (e.g., Basu et al., 1991, 1996).

Fejer (1993) presented a climatological study of nighttime low-latitude plasma drift and neutral wind coupling using F-region zonal plasma drifts from the Arecibo Incoherent Scatter Radar and DE-2 satellite and FPI zonal winds observations. This study reported a better agreement between zonal drifts and winds for higher solar flux and local summer

conditions, which was explained as due to the increased F-region conductivity over the E-region conductivity. The observed zonal disturbance drifts were strongest around midnight. [Fejer and Scherliess \(1998\)](#) used longitudinally averaged DE-2 satellite zonal drifts observations to study the prompt-penetration zonal plasma drifts at low latitudes and found that sudden increases in convection lead to predominantly westward perturbation drifts, which decrease equatorward and have largest amplitudes in the dusk-midnight.

[Fejer et al. \(2005\)](#) presented the most comprehensive climatological study of the storm-time effects of the zonal drifts using Jicamarca radar observations. They found that the zonal drifts disturbances were strongest around midnight and increase strongly for solar flux near Equinox and December solstice, and showed basically no effects around June solstice. They found that these disturbances have two main time scales corresponding to 3-15 hours and to 15-24 hours. These time scale effects were dominant around midnight and in the postmidnight sector, respectively. [C.-S. Huang and Roddy \(2016\)](#) used observations from the Communication/Navigation Outage Forecasting System (CNOFS) satellite to study the motion of equatorial plasma bubbles (EPB) which is controlled by ambient zonal drifts and winds. Their results showed similar nighttime westward disturbances than in [Fejer et al. \(2005\)](#).

[Fejer and Emmert \(2003\)](#) used Jicamarca and Arecibo vertical plasma drifts and UARS wind measurements during the 19–21 October 1998 major geomagnetic storm for the first detailed study of low latitude disturbance dynamo effects. These observations showed initially large and short-lived vertical drift and wind perturbations due to prompt penetration electric fields triggered first by a sudden increase in the solar wind dynamic pressure and later, as the geomagnetic storm progressed, longer-lived disturbances by disturbance dynamo electric field effects. They also showed that for an increase in the polar cap potential, the low latitude zonal disturbance drifts are eastward and poleward during the day, westward and poleward at night, and equatorward near dawn. These polarities are opposite for a sudden decrease of the polar cap potential. These results agree with those from [Fejer and Scherliess \(1998\)](#). The observed eastward disturbance drifts and winds were similar during

daytime, and had large variability of the zonal disturbance drifts at night.

[Santos et al. \(2016\)](#) studied the disturbance zonal and vertical plasma drifts over Jicarica for the April 1997 and June 2008 storms. They found eastward prompt penetration electric fields on the vertical drifts and simultaneous large westward drifts with an apparent anticorrelation at night time. They suggested that the anticorrelated oscillations are driven by an enhanced nighttime E region ionization produced by energetic particles precipitation during the main phases of these storms. [Xiong et al. \(2016\)](#) used longitudinally averaged equatorial zonal disturbance drifts and winds from the CHAMP and ROCSAT-1 and suggested that prompt penetration electric fields, due to sudden changes in the magnetospheric convection (e.g., [Fejer, 2011](#)), produce zonal disturbance winds that are westward in the afternoon sector and eastward in the post-midnight sector. They also found that these and the corresponding effects on the vertical drifts are anti correlated.

Recently, [S.-R. Zhang et al. \(2017\)](#) found oscillations in the zonal electric field along with oscillations in the meridional winds over Arecibo during the 2015 St. Patrick's Day storm and suggested that they are related to storm time polarization electric field generated by large scale traveling atmospheric disturbances (TAD). In the same line, [K. Zhang et al. \(2019\)](#) used Coupled Magnetosphere Ionosphere-Thermosphere simulations to study periodic oscillations in the thermospheric meridional winds during IMF Bz temporal variations. They found that the oscillations in the thermosphere can react almost simultaneously at all latitudes and also shown a long-term disturbance on these winds due to TADs at all latitudes.

Other coupling aspect is the effect of the F-region layer height motion over the oxygen line emission due to disturbance electric fields during geomagnetic storms. The motion of the F-region layer height affects the concentration of the constituents necessary for the dissociative recombination that mainly controls the thermospheric 630 nm oxygen line production. [Chakrabarty et al. \(2005, 2010\)](#) showed that the OI 630 nm airglow emission is anti-correlated to the F-region layer height due to the effects of prompt-penetration electric fields over the equatorial Indian sector. They found fluctuations on their airglow intensity

measurements varying in the opposite directions to the motions of the F-region layer height. [Chakrabarty et al. \(2015\)](#) also presented evidence of oxygen airglow intensity effects for different types of electric field disturbances of magnetospheric origin. Similarly, [Vineeth et al. \(2019\)](#) used a multi-photometer to study the response of several nighttime airglow emissions during prompt penetration electric fields events. They found that a downward (upward) motion of the F-region peak during westward (eastward) disturbance electric fields produce an enhancement (depletion) in the intensity of these emission emissions. These variations were stronger for the 630nm oxygen emission line and are in agreement with [Chakrabarty et al. \(2005, 2010, 2015\)](#).

## 6.2 Data and Methodology

The FPI wind measurements and their database were already described in sections [3.1.5](#) and [4.2](#). The zonal plasma drifts were obtained from Jicamarca incoherent scatter radar observations from August 1970 to February 2018. These drifts represent 15-min averages at altitudes from about 250 to 500 km, where the signal to noise ratio is highest. The cleaning procedure was similar to that explained in [3.2](#) and [5.2](#). Since 1994, the uncertainties of the zonal drifts were generally about 5 m/s during daytime and about 15 m/s at night as a result of an improved data analysis technique described by [Kudeki et al. \(1999\)](#). The uncertainties of the earlier measurements were about twice as large.

Our zonal drift database consists of 9193 hours of observations. Table [6.1](#) shows the number of hours of these observations in 4-months seasonal bins. The smallest number of observations is from May-August period with 2386 hours. In general, the data distribution is fairly evenly distributed for quiet time conditions except around sunset and for solar flux units higher than 200 units. This is particularly the case for December solstice. The data is sparser for geomagnetically active nighttime conditions due to the effect of spread-F.



Table 6.1: Seasonal Distribution of the 15-min averaged Jicamarca Zonal Drifts.

Number of hours	Nov-Feb	Mar-Apr Sep-Oct	May-Aug
$K_p \leq 3$	2804	2400	1936
$K_p > 3$	681	922	450

### 6.3 Results

We first compared the zonal components of the nighttime quiet-time equatorial thermospheric winds and ionospheric plasma drifts. Figure 6.1 shows the seasonally averaged quiet-time zonal plasma drifts and neutral winds for moderately solar flux conditions. The standard deviations are generally about 20 m/s for both winds and drifts. In general, these results show a good agreement between both parameters. The early night neutral winds are larger than the plasma drifts from March through October; after  $\sim 22$  LT the winds and drifts have comparable magnitudes, except during December solstice when the wind magnitudes are smaller. As pointed out earlier our wind database during this season is sparse particularly for higher solar fluxes.

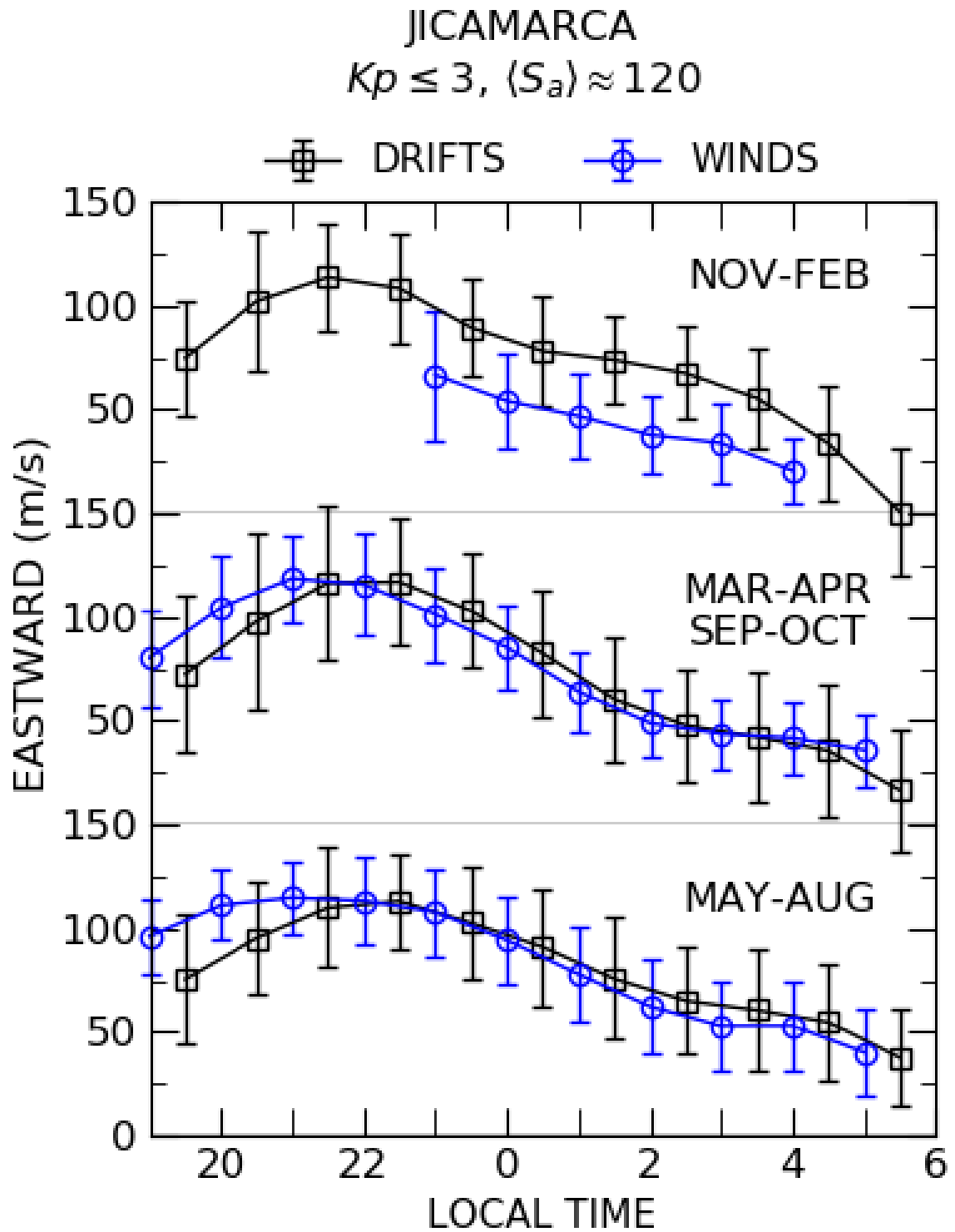


Figure. 6.1: Quiet-time zonal plasma drifts and nighttime thermospheric winds. The error bars correspond to standard deviations.

The disturbance winds used in this chapter were derived using the procedure described earlier. The perturbation zonal drifts were derived by using a similar procedure which consisted in removing solar flux and seasonal dependent quiet-time ( $K_p \leq 3$ ) half-hourly averages for three different solar flux conditions. These quiet-time averages, which are similar to the ones presented by [Fejer et al. \(2005\)](#), are shown in Figure 2.10 in chapter 2. The zonal drift residuals were averaged in hourly bins and are presented in Figure 6.2. Their standard deviations on the average disturbance drifts are about 8 m/s at nighttime.

Figure 6.2 compares the disturbance zonal drifts and disturbance zonal winds (see chapter 4) corresponding to an average increase in the geomagnetic activity of about  $\Delta K_p \approx 3.2$  and for moderate solar flux conditions. The nighttime wind and drift disturbances are westward, strongest around midnight, and are in better agreement in the postmidnight sector.

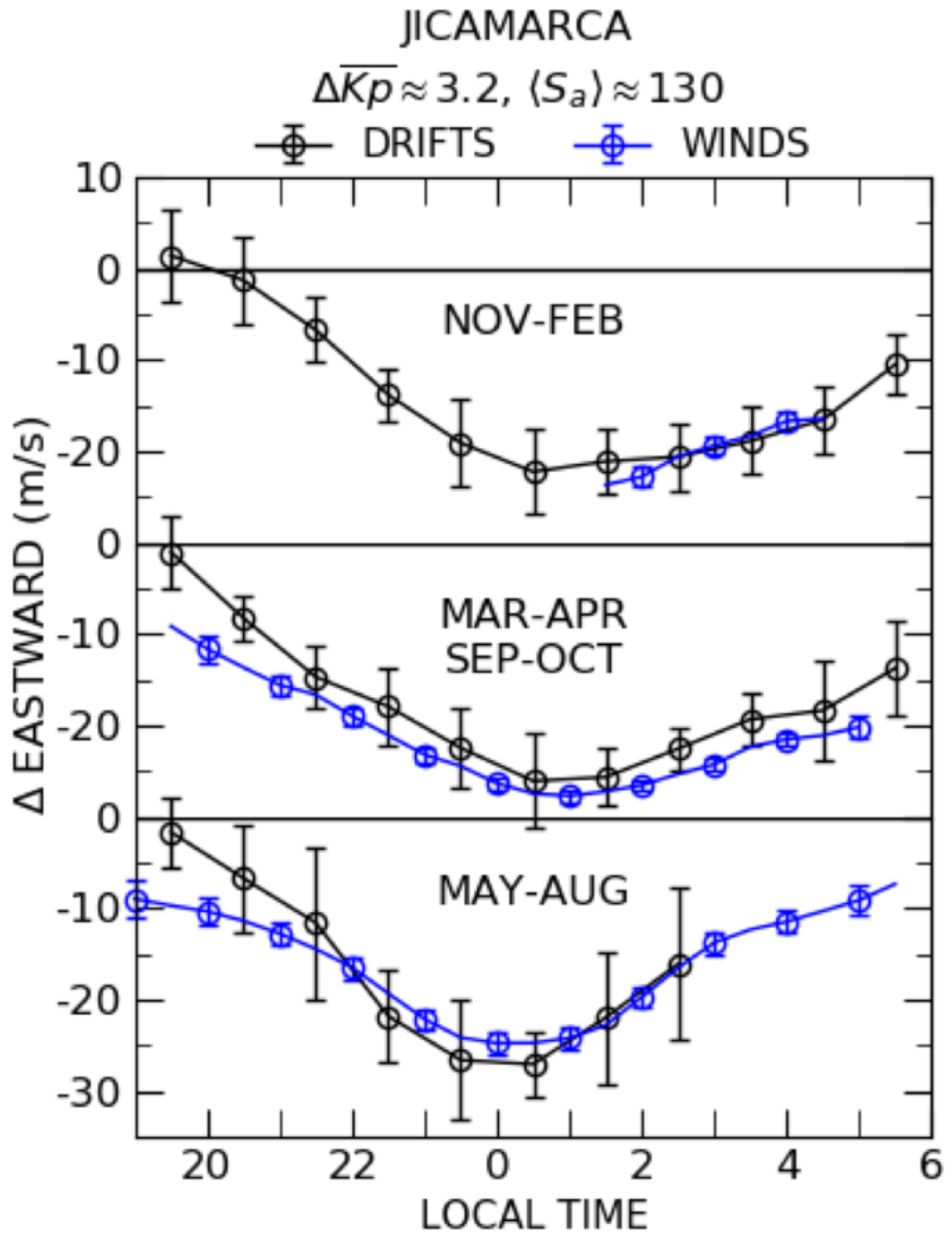


Figure. 6.2: Seasonal comparison of the disturbance zonal drifts and winds. The scatter bars denote the standard errors of the means.

We evaluated the coupled dynamics and electrodynamics of the zonal plasma drifts and neutral winds for two large and long-lasting geomagnetic storms during the 06-09 September 2017 and 25-28 August 2015. We compared these parameters to illustrate the coupled storm-time effects during disturbance dynamo electric fields and disturbance winds, and also during prompt penetration electric field events. For these comparisons we used half-hourly zonal plasma drifts to match the resolution of the zonal winds. The zonal wind observations were calculated from the corresponding line-of-sights of the Nasca and Jicamarca FPIs.

Figure 6.3 shows the time evolution of the ionospheric zonal plasma drifts and the thermospheric zonal neutral winds during the 06-09 September 2017 storm. This geomagnetic storm started with a sudden increment of the SymH index around 19 LT 06 September that lasted for about 4 hours. This increase seems to be initially related to an increase in the solar wind dynamic pressure (not shown). The average AE and Kp were about 250 nT and 3+ respectively during this period. Later, the storm main phase occurred from  $\sim$ 16 LT to  $\sim$ 21 LT 07 September and its recovery phase lasted for about 3 days. During the main phase, the AE peak was about 2000 nT and the average Kp was about 7+. After the main phase there was a relatively low quiet-time period followed by 2 days of moderately disturbed conditions with an average AE of about 1000 nT and an average Kp of 5+.

Figure 6.3 shows oscillations on both zonal plasma drifts and neutral winds from  $\sim$ 19 LT 06 September to  $\sim$ 04 LT 07 September. These oscillations have a periodicity of about an hour, mostly during the period of an increase in the solar wind dynamic pressure. During the first part of the second night, the development of strong spread-F irregularities precluded zonal drifts observations, while near midnight there were strong westward disturbance dynamo drifts and westward disturbance winds that reached magnitudes of about 50 m/s. The effects of the disturbance dynamo still persisted in the third night when they occurred from 18 LT 08 September to 06 LT 09 September with nearly steady westward disturbance drifts and winds of about 50 m/s. The zonal drifts and winds largely recovered to their quiet values in the premidnight sector of the fourth night, while in the postmidnight period

they exhibited eastward perturbations. The eastward wind perturbations were particularly strong near dawn.

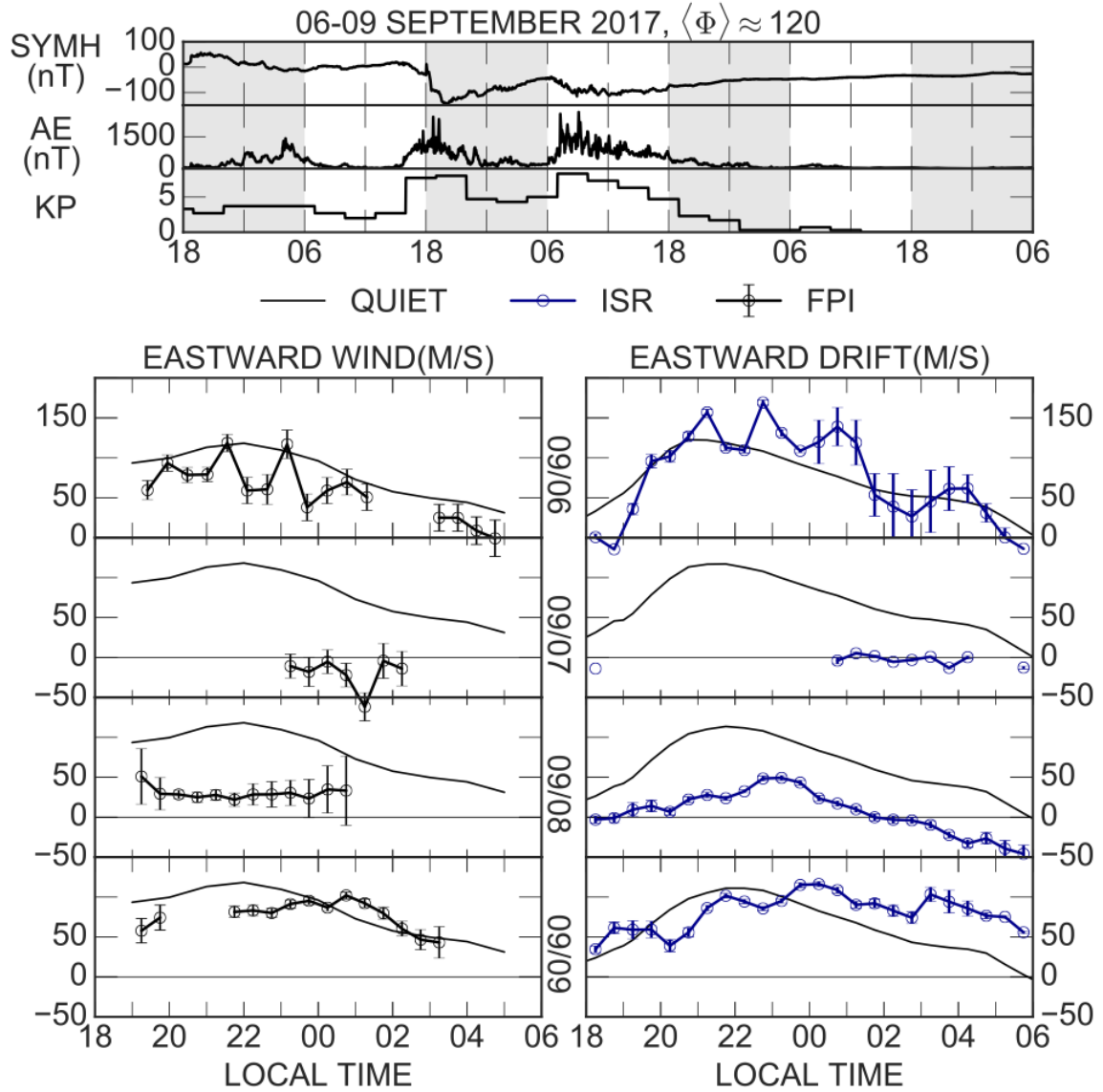


Figure. 6.3: Time evolution of equatorial zonal plasma drifts and neutral winds for the 06-09 September 2017 storm. (Top) Geomagnetic indices showing the evolution of the geomagnetic storm. (Bottom) Zonal plasma drifts and neutral winds for each corresponding night.

Figure 6.4 shows another a closer comparison of the coupling between the zonal thermospheric winds and ionospheric drifts during the September 2017. During the first night, the oscillations on both components seems to be correlated and in good agreement. They show a delay of about 15 minutes appearing first in the zonal drifts, and have about the same periodicity of one hour. These oscillations are also shown in the thermospheric meridional winds and seems to be anticorrelated to the zonal winds (not shown). During the period of strong and long-lasting disturbance dynamo effects in the nights of the 07-08 and 08-09 September, both zonal components of neutral winds and plasma drifts show to be highly coupled and in very good agreement. They also show to be in good agreement during the slow recovery of the fourth night, and in particular during the postmidnight period where both of them showed stronger eastward velocities.

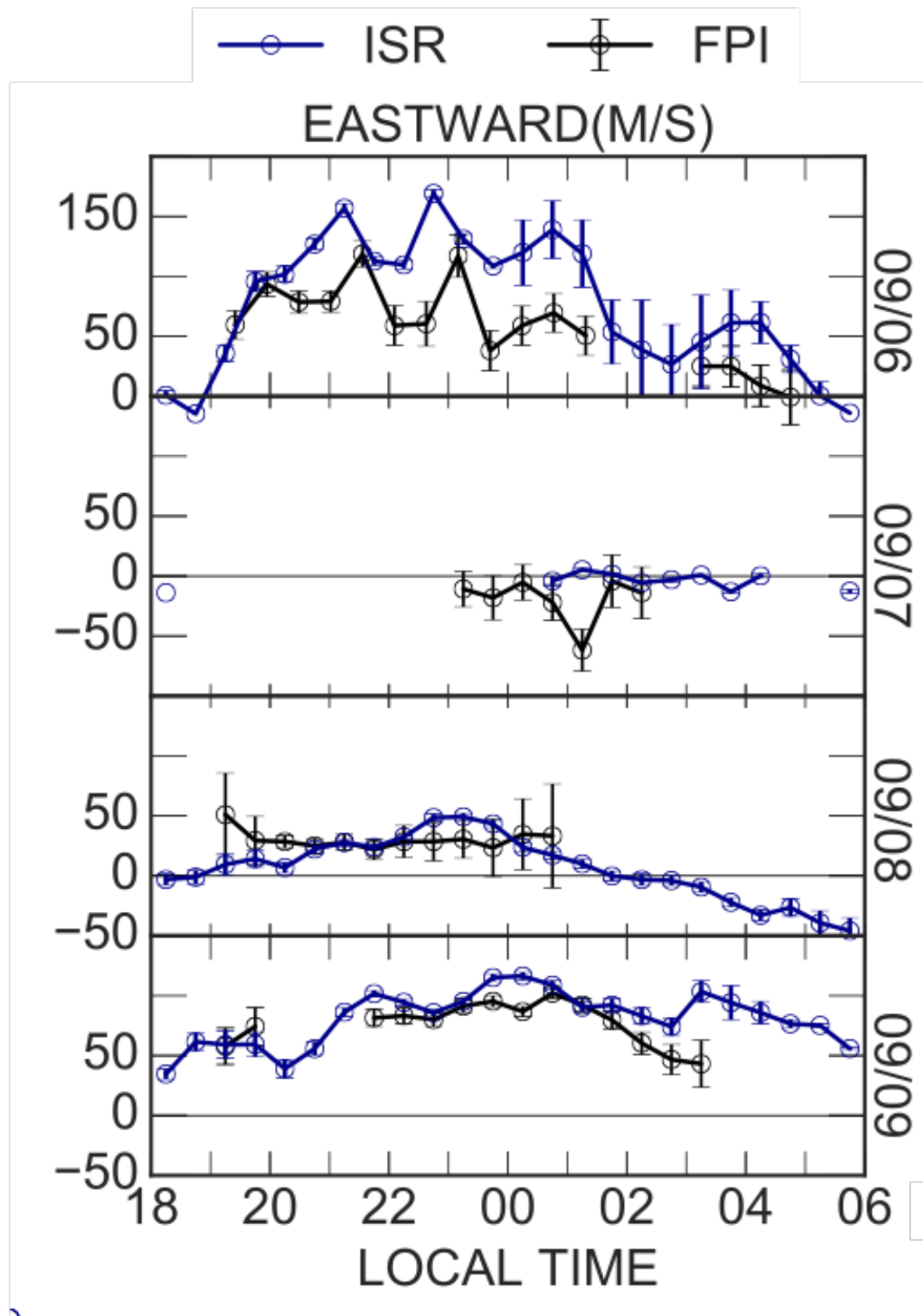


Figure. 6.4: Comparison of thermospheric winds and ionospheric drifts during the September 2017 storm.



Figure 6.5 shows the corresponding observations as in Figure 6.3 but for the geomagnetic storm of 25-28 August 2015. During this storm, there was a long main phase that started about the 00 LT 26 August and reached to a minimum -100 nT around 00 LT 27 August and again around 15 LT of the same day. The recovery phase of this storm lasted for about two days afterwards. In the first night both components showed a good agreement and closely follow their quiet-time averages. During the nights of 26-27 and 27-28 August there were typical signatures of strong disturbance dynamo zonal drifts and winds. The disturbed thermospheric zonal winds closely agreed with the ionospheric drifts for both nights. These disturbances started around midnight on the second night and grew to about 70 m/s westward around 03 LT 27 August for both components. In the following night (28 August), they were about 70 m/s westward for the zonal winds and about 100 m/s westward the zonal drifts around midnight, and about the same in the postmidnight sector. In the fourth night, the zonal winds closely returned to their quiet-time values.

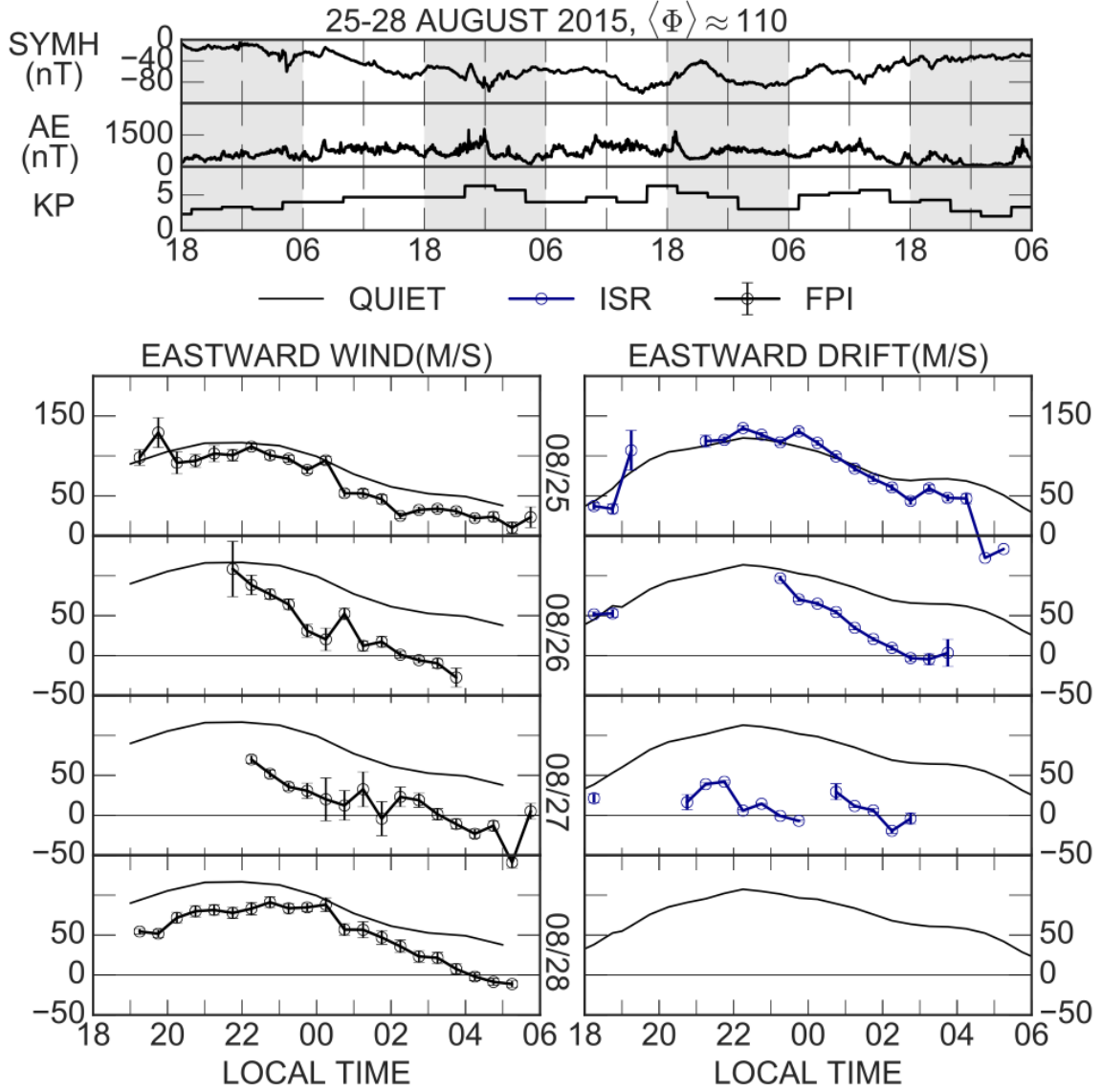


Figure. 6.5: Time evolution of equatorial zonal plasma drifts and neutral winds for the 25-28 August 2015 storm. (Top) Geomagnetic indices showing the evolution of the geomagnetic storm. (Bottom) Zonal plasma drifts and neutral winds for each corresponding night.

#### 6.4 Discussion

We have evaluated in detail, for the first time, the coupling of equatorial zonal disturbance winds and drifts during both geomagnetic quiet and disturbed times. Our baseline

average quiet-time patterns agree with results from previous plasma drift and thermospheric wind studies (e.g., [Biondi et al., 1988](#); [Fejer et al., 2005](#); [Chapagain et al., 2013](#); [Navarro & Fejer, 2019](#)).

We have shown that, except near dusk, highly coupled the quiet-time dynamics and electrodynamics of these observables during different seasons. This strong coupling occurs even though the neutral winds are geographically local (mostly from altitudes of about 250 km) observables influenced by thermospheric tides, heat sources and its local ionosphere, and the plasma drifts result from magnetic field-line ionospheric conductivity dependent integrated effects.

We showed the good agreement between the seasonal quiet-time average patterns of zonal drifts and winds for moderate solar flux conditions in agreement with previous studies (e.g., [Biondi et al., 1988](#); [Chapagain et al., 2013](#)). Early night neutral winds are larger than plasma drifts from March through October most likely due to the gradual buildup of the polarization electric field which drives the zonal drifts, and to the somewhat comparable E and F region conductivities, which drives this polarization electric field ([Chapagain et al., 2013](#); [Fejer et al., 1983](#)). After 22 LT, there is a general agreement in their magnitudes and, in particular, in the postmidnight sector when the descent of the F-layer peak produces a stronger E- to F-region conductivity ratio. The stronger drift velocities in the December solstice postmidnight sector might be related to the moderate solar flux conditions (e.g., [Valladares et al., 2002](#)) but also could be related to additional polarization electric fields generated by altitudinal gradients in the zonal neutral winds (e.g., [Coley et al., 1994](#)). In general, the agreement between equatorial zonal drifts and winds gets closer with the increase of the solar flux ([Fejer et al., 1983](#)).

We also showed, for the first time, the close seasonal agreement of the equatorial zonal disturbance drifts and winds. The seasonal dependence of the equatorial disturbance drifts is also shown for the first time and agrees with previous studies (e.g., [Fejer et al., 2005](#); [C.-S. Huang & Roddy, 2016](#)). Both disturbance average patterns have about the same local time and seasonal dependence. They are westward throughout the night with peak

magnitudes around midnight and stronger magnitudes in the postmidnight sector. They are also strongest in Equinox in agreement with previous studies (e.g., [Fejer et al., 2005](#); [Navarro & Fejer, 2019](#)). In general, the magnitudes of both components are comparable except perhaps at early night probably due to the smaller E- to F-region conductivity ratio during that period.

Our storm case studies showed highly coupled dynamics and electrodynamics not only during large and long-lasting disturbance dynamo electric fields and disturbance winds, but also, and for the first time, during short-lived prompt penetration electric field events. Large and long-lasting disturbances show a strong coupling with similar local time variation. They are stronger around and after midnight, and can last longer than 36 hours. The basic mechanism of these long-lasting disturbance drifts can be mostly explained by the schematic presented in [Mazaudier and Venkateswaran \(1990\)](#). However, this mechanism does not account for effects coming from below, effects due to motions of the F-region layer, and ion-drag effects. The strong coupling between zonal drifts and winds suggests that both parameters have similar two main time scale effects as found by [Fejer et al. \(2005\)](#). This might serve to explain the disagreement between UARS-WINDII and FPI equatorial disturbance wind observations reported by [Navarro and Fejer \(2019\)](#). Clearly more observations and studies are needed to fully understand these complex phenomena.

We showed short-term correlated oscillations in the zonal neutral winds and plasma drifts. They were due to prompt penetration electric fields events probably initially driven by an increase in the solar wind dynamic pressure as reported in previous storm studies (e.g., [Fejer & Emmert, 2003](#)). They are delayed about 15 minutes appearing first in the zonal drifts, and have about the same periodicity of one hour. The wind oscillations seemed to be driven by the ion drag action of the drifts, as suggested by previous studies ([Joshi et al., 2015](#)) and theoretical predictions ([K. Zhang et al., 2019](#)). The uncertainty of the winds was slightly increased during the effect of the prompt penetration events most likely due to the vertical motion of the oxygen line intensity during this period ([Chakrabarty et al., 2005, 2010, 2015](#); [Vineeth et al., 2019](#)). Nevertheless, the vertical motion of the oxygen

emission layer was not severe most likely as a consequence of the weak magnitude of the penetration electric fields which enabled its remote observation. It is important to mention that these observations are particularly difficult to obtain not only because of the frequent generation of spread-F irregularities, but also due to the decrease of the airglow intensity during rapid changes of the F-region peak height driven by disturbances of magnetospheric origin. Clearly, additional studies are needed to fully understand the specific observing conditions, the contributions from the different disturbance processes and the ion-drag effects on the thermospheric winds due to prompt penetration electric fields.

## 6.5 Summary and Conclusions

We have presented the highly coupled equatorial dynamics and electrodynamics of the zonal thermospheric neutral winds and ionospheric plasma drifts for different seasons and geomagnetic activity conditions under moderate solar flux conditions. Our results show strong coupling between these parameters, in particular during the postmidnight sector. We have shown, for the first time, the strong seasonal agreement of the zonal disturbance drifts and winds. They are westward throughout the night with strongest magnitudes around midnight and during equinox. We have also shown the highly coupled dynamics and electrodynamics during the effect of large and long-lasting disturbance dynamo electric fields and disturbance winds, and, for the first time, during prompt penetration electric fields. We reported correlated oscillations on the zonal drifts and winds of about one hour that are delayed by 15 minutes appearing first on the drifts. However, our database does not provide us with many such penetration drag events given the inherent difficulty of having both instruments operating under these particular conditions.

## CHAPTER 7

### SUMMARY AND FUTURE WORK

In this chapter we will summarize our major conclusions and will present suggestions for future work.

#### 7.1 Summary and Conclusions

We have presented a comprehensive study of the equatorial thermospheric neutral winds and ionospheric electric fields (plasma drifts) due to geomagnetic disturbances using observations from the Jicamarca Incoherent Scatter Radar and from a network of Fabry-Perot Interferometers recently deployed in the central region of Peru respectively. We have discussed the seasonal climatology of the disturbance winds and have presented their extended geomagnetic effects to significantly improve their empirical predictions during large storms; the geomagnetic activity and solar flux dependence of the annual variation of the disturbance dynamo vertical plasma drifts; and, finally, the coupling of the zonal plasma drifts and neutral winds climatologically and during the effects of prompt penetration electric fields and disturbance dynamo electric fields for specific storm cases.

##### 7.1.1 On the disturbance winds

The major emphasis in this work, however, was the determination of the characteristics of the thermospheric neutral winds during geomagnetically active conditions. We have used multi-site FPI measurements to estimate thermospheric wind maps over the Peruvian equatorial region, and to determine for the first time the local time and seasonal dependence of the nighttime equatorial extended quiet and disturbed zonal and meridional winds. We have determined that the equatorial nighttime winds increase slightly eastward from local to extended quiet conditions, and have used 12-hours extended quiet average winds as our baseline for inferring geomagnetic activity driven disturbance winds. Our resultant

wind database is considerable reduced during December solstice, this is partly due to less favorable observing conditions but also to the large rise of the F-region peak height that is longest during this season ([Davila, 1994](#)).

We showed that the night-time disturbance winds are westward with strongest magnitudes around midnight. They have comparable magnitudes before midnight, increase westward to about midnight and decrease towards dawn; and are largest during equinox and smallest during June solstice. The equinoctial and June solstice meridional disturbance winds are comparable and northward in the premidnight sector and decrease from dusk to midnight where they reverse to southward. In the postmidnight sector, the southward disturbance winds increase towards dawn and have largest values during December solstice and smallest during equinox. We have also seen that the DWM07 significantly underestimates, particularly near midnight, the magnitude of the nighttime zonal disturbance winds.

We showed that empirical predictions of equatorial thermospheric winds during large storms can be significantly improved by introducing extended geomagnetic activity effects. We presented a simple linear model that uses 9-hours extended geomagnetic activity effects to take into account previous geomagnetic activity that produces a steady meridional circulation, in particular, during the recovery phase of the storm similar to [Scherliess and Fejer \(1997\)](#) for the plasma drifts. Nevertheless, the model predictions could be improved by introducing longer-term disturbance parameters similar to [Fejer et al. \(2005\)](#) where longer terms of 15-24 hours after enhanced geomagnetic activity was found for the equatorial zonal plasma drifts. However, our current database does not allow us to perform such quest. Similarly, short-lived disturbances were observed in the meridional winds probably due to trans-equatorial traveling atmospheric disturbances. The use of shorter-term disturbance parameters would also improve the prediction of both zonal and meridional disturbance winds by taking time delay effects into account.

### 7.1.2 On the disturbance dynamo vertical drifts

We have determined the solar flux and geomagnetic activity dependence of the annual variation of the Jicamarca disturbance dynamo vertical drifts following 6-hours of enhanced

geomagnetic activity given by a 6-hours AE increase of 250 nT. For moderate solar flux conditions, the daytime disturbance drifts are smaller than about 5 m/s and generally downward, except in the late afternoon sector. Near dusk, they are downward with largest and smallest magnitudes during the autumnal equinox and May-June, respectively. The early night drift reversal times from downward to upward occur earliest during May-June and latest during January-February. The nighttime disturbance drifts are upward with largest magnitudes close to sunrise and vary weakly with season, except for slightly smaller values during May-June. The disturbance drifts reverse from upward to downward near dawn.

We have shown that the disturbance dynamo drifts vary most strongly with solar flux near dusk, but this dependence changes significantly throughout the year. In this local time sector, an increase in the solar flux index from about 90 to 180 s.f.u. results in an increase of the peak downward drift from 5 to 20 m/s during for September-October, but only from about 3 to 5 m/s during May-June. Although our average disturbance drifts are less accurate during December solstice, they also indicate a strong increase of the peak downward drift with solar flux. Similar annual variation is found for increased geomagnetic activity, but with no shift to later local times.

The evening disturbance dynamo drifts have larger values during the autumnal equinox than during the vernal equinox, particularly during low solar flux conditions. The morning and early afternoon disturbance dynamo drifts, which are predominantly downward during low solar flux periods, decrease and even turn slightly eastward during high solar flux conditions. The nighttime upward disturbance drifts do not change much from low to high solar flux periods, but they increase strongly with geomagnetic activity close to dawn. These drifts also do not change much with season, except perhaps for the early night period. The relatively large late night upward disturbance dynamo drift and the decrease of the nighttime quiet-time ambient downward vertical drifts with solar flux, makes the disturbance dynamo drifts an increasingly important driving mechanism for equatorial spread F during low solar flux geomagnetic active periods. The same is the case near dusk during July-August.



### 7.1.3 On the storm-time coupling of zonal plasma drifts and neutral winds

We have shown preliminary results on the coupling of the zonal winds and zonal drifts during quiet- and storm-time conditions, and will have shown their coupled dynamics under strong disturbance dynamo electric fields and also for the first time under prompt penetration electric fields.

We have seen that both components have a good agreement during quiet and storm time conditions and in particular in the postmidnight sector. This agreement improves for higher solar flux conditions due to the increase in conductivities that generates stronger polarization electric fields at nighttime. The coupling during postmidnight improves due to the descent of the F-region height peak (Fejer, 1993). We have also shown that both climatological averages zonal drifts and winds have maximum around midnight and have a better in the postmidnight sector

For the storm cases that we have evaluated, both plasma drifts and winds undergo strong disturbances on different time scales due to disturbance dynamo and to prompt penetration of magnetospheric electric fields. The oscillations observed in the latter disturbances, are seen on both zonal and meridional wind components, and the zonal wind components seems to be correlated with the same oscillations in the zonal drifts. These oscillations have a periodicity of about 1 hour and both zonal drifts and winds show a good agreement and also a delay on the winds of about 15 mins respect to the drifts. During periods of long-lasting disturbances most likely due to disturbance dynamo effects and wind-driven disturbances at high latitudes on the drifts and winds respectively, they show a highly coupled dynamics with similar local time dependence.

## 7.2 Suggestions for Future Work

We have seen in this work, although the basic physical dynamics and electrodynamics of the thermosphere and ionosphere is fairly well understood, there are still questions regarding the large variability during large geomagnetic storms that is observed in the incoming observations. This is even more difficult to address given the limited storm-time observations of accurate plasma drifts and neutral winds. This is partly due to the reduced number of

available measurements, in particular of the electric fields during nighttime, but also to the motion of the F-layer peak height that can decrease the oxygen airglow intensity and so the accuracy of the neutral winds observations, if we assume favorable observing conditions of clear skies for these instruments. On this last regard, the inclusion of cloud sensors is also advisable. More high-resolution imaging observations are needed to constantly monitor the equatorial latitudes in order to gain better insight that can help us to predict related phenomena like the generation of spread-F irregularities. On this regard, the recently launched mission Ionospheric Connection Explorer (ICON) host on board not only an ion drift meter but also a Michelson Interferometer. These capabilities allow us to observe both plasma drifts and neutral winds simultaneously to test several of the observations that we have found on this dissertation.

The vertical drifts database is the largest database available to perform storm studies and we have found dependencies on solar flux and geomagnetic activity for the annual variation of disturbance dynamo electric fields. However, more studies are needed to include solar wind parametrization, for example, a possible importance of the IMF  $B_y$  at the equator. Similarly, several other aspects can be explored regarding the storm-time neutral winds. Our database was not large enough to include the solar flux dependence of the disturbance winds. Future studies can also include a better parametrization for the meridional winds which could be done using Polar Cap index, or PC index, to study the interhemispheric TADs.

Similarly, empirical modelling of the disturbances presented in this dissertation could be explored in more detail. The disturbance dynamo electric fields have been studied using only 6-hours of geomagnetically active conditions but longer-terms are also needed to fully characterize these disturbances. Similarly, the disturbance winds have been studied using only 9-hours of geomagnetically active conditions, and longer terms of these parametrization could be explored. However, more observations or including other datasets are needed to fulfill this requirement.

These observations have shown that the thermosphere and the ionosphere are closely

coupled. However, more studies are needed to understand the role of the vertical shear of the neutral winds and of the solar flux dependence for when the zonal drifts appear a bit stronger. More coordinated efforts are needed to overcome these questions. Moreover, during large storms, these observations have revealed strong coupling effects during geomagnetically active conditions, in particular during prompt penetration electric fields for the first time. At the same time, they have opened several questions regarding the time scales and the dependencies of these effects in solar flux, local time and season. Future studies could also focus on the F-layer peak altitude range under which these effects could be seen by the ground- or spaced-based instrumentation.

Finally, it is important to mention that the studies of geomagnetic storms at the magnetic equator are very limited without having electric fields measurements at other latitudes. Moreover, the update of the different empirical models that many times are used as inputs for other theoretical models or for other space weather applications is also desirable given the databases available and, in special, with the ICON mission on flight.

## REFERENCES

- Abreu, V. J., Schmitt, G. A., Hays, P. B., & Dachev, T. P. (1982). Volume emission rate profiles of the 6300-Å tropical nightglow obtained from the AE-E satellite: Latitudinal and seasonal variations. *Journal of Geophysical Research: Space Physics*, 87(A8), 6346–6352. <https://doi.org/10.1029/JA087iA08p06346>
- Alken, P. (2009). A quiet time empirical model of equatorial vertical plasma drift in the Peruvian sector based on 150 km echoes. *Journal of Geophysical Research: Space Physics*, 114(A2). <https://doi.org/10.1029/2008JA013751>
- Anderson, D. N., & Roble, R. G. (1974). The effect of vertical  $E \times B$  ionospheric drifts on F region neutral winds in the low-latitude thermosphere. *Journal of Geophysical Research (1896-1977)*, 79(34), 5231–5236. <https://doi.org/10.1029/JA079i034p05231>
- Bartels, J., Heck, N. H., & Johnston, H. F. (1939). The three-hour-range index measuring geomagnetic activity. *Terrestrial Magnetism and Atmospheric Electricity*, 44(4), 411–454. <https://doi.org/10.1029/TE044i004p00411>
- Basu, S., Basu, S., Kuoeki, E., Zengingonul, H. P., Biondi, M. A., & Meriwether, J. W. (1991). Zonal irregularity drifts and neutral winds measured near the magnetic equator in Peru. *Journal of Atmospheric and Terrestrial Physics*, 53(8), 743 – 755. [https://doi.org/10.1016/0021-9169\(91\)90125-Q](https://doi.org/10.1016/0021-9169(91)90125-Q)
- Basu, S., Kudeki, E., Basu, S., Valladares, C. E., Weber, E. J., Zengingonul, H. P., et al. (1996). Scintillations, plasma drifts, and neutral winds in the equatorial ionosphere after sunset. *Journal of Geophysical Research: Space Physics*, 101(A12), 26795–26809. <https://doi.org/10.1029/96JA00760>
- Biondi, M. A., Meriwether, J. W., Fejer, B., & Woodman, R. (1988). Measurements of the dynamics and coupling of the equatorial thermosphere and the F-region ionosphere in Peru. *Journal of Atmospheric and Terrestrial Physics*, 50(10), 937–942. [https://doi.org/10.1016/0021-9169\(88\)90081-5](https://doi.org/10.1016/0021-9169(88)90081-5)
- Biondi, M. A., Meriwether, J. W., Fejer, B. G., & Gonzalez, S. A. (1990). Seasonal variations in the equatorial thermospheric wind measured at Arequipa, Peru. *Journal of Geophysical Research*, 95(A8), 12,243–12,250. <https://doi.org/10.1029/JA095iA08p12243>
- Biondi, M. A., Meriwether, J. W., Fejer, B. G., Gonzalez, S. A., & Hallenbeck, D. C. (1991). Equatorial thermospheric wind changes during the solar cycle: Measurements at Arequipa, Peru, from 1983 to 1990. *Journal of Geophysical Research*, 96(A9), 15,917–15,930. <https://doi.org/10.1029/91JA01645>
- Biondi, M. A., Sazykin, S. Y., Fejer, B. G., Meriwether, J. W., & Fesen, C. G. (1999). Equatorial and low latitude thermospheric winds: Measured quiet time variations with

- season and solar flux from 1980 to 1990. *Journal of Geophysical Research*, 104(A8), 17,091-17,106. <https://doi.org/10.1029/1999JA900174>
- Blanc, M., & Richmond, A. D. (1980). The ionospheric disturbance dynamo. *Journal of Geophysical Research*, 85(A4), 1669-1686. <https://doi.org/10.1029/JA085iA04p01669>
- Bowles, K. L. (1963). Measuring Plasma Density of the Magnetosphere. *Science*, 139(3553), 389-391. <https://doi.org/10.1126/science.139.3553.389>
- Brum, C. G. M., Tepley, C. A., Fentzke, J. T., Robles, E., dos Santos, P. T., & Gonzalez, S. A. (2012). Long-term changes in the thermospheric neutral winds over Arecibo: Climatology based on over three decades of Fabry-Perot observations. *Journal of Geophysical Research*, 117(A2). <https://doi.org/10.1029/2011JA016458>
- Chakrabarty, D., Rout, D., Sekar, R., Narayanan, R., Reeves, G. D., Pant, T. K., et al. (2015). Three different types of electric field disturbances affecting equatorial ionosphere during a long-duration prompt penetration event. *Journal of Geophysical Research: Space Physics*, 120(6), 4993-5008. <https://doi.org/10.1002/2014JA020759>
- Chakrabarty, D., Sekar, R., Narayanan, R., Devasia, C. V., & Pathan, B. M. (2005). Evidence for the interplanetary electric field effect on the oi 630.0 nm air-glow over low latitude. *Journal of Geophysical Research: Space Physics*, 110(A11). <https://doi.org/10.1029/2005JA011221>
- Chakrabarty, D., Sekar, R., Sastri, J. H., Pathan, B. M., Reeves, G. D., Yumoto, K., et al. (2010). Evidence for oi 630.0 nm dayglow variations over low latitudes during onset of a substorm. *Journal of Geophysical Research: Space Physics*, 115(A10). <https://doi.org/10.1029/2010JA015643>
- Chapagain, N. P., Fisher, D. J., Meriwether, J. W., Chau, J. L., & Makela, J. J. (2013). Comparison of zonal neutral winds with equatorial plasma bubble and plasma drift velocities. *Journal of Geophysical Research: Space Physics*, 118(4), 1802-1812. <https://doi.org/10.1002/jgra.50238>
- Coakley, M. M., Roesler, F. L., Reynolds, R. J., & Nossal, S. (1996). Fabry-Perot CCD annular-summing spectroscopy: study and implementation for aeronomy applications. *Applied Optics*, 35(33), 6479-6493. <https://doi.org/10.1364/AO.35.006479>
- Coley, W. R., Heelis, R. A., & Spencer, N. W. (1994). Comparison of low-latitude ion and neutral zonal drifts using DE 2 data. *Journal of Geophysical Research: Space Physics*, 99(A1), 341-348. <https://doi.org/10.1029/93JA02205>
- Coley, W. R., McClure, J. P., & Hanson, W. B. (1990). Equatorial fountain effect and dynamo drift signatures from AE-E observations. *Journal of Geophysical Research: Space Physics*, 95(A12), 21285-21290. <https://doi.org/10.1029/JA095iA12p21285>
- Coley, W. R., Stoneback, R. A., Heelis, R. A., & Hairston, M. R. (2014). Topside equatorial zonal ion velocities measured by c/nofs during rising solar activity. *Ann. Geophys.*, 32(2), 69-75. <https://doi.org/10.5194/angeo-32-69-2014>

- Conde, M. (2002). Deriving wavelength spectra from fringe images from a fixed-gap single-etalon Fabry–Perot spectrometer. *Applied Optics*, 41(14), 2672–2678. <https://doi.org/10.1364/AO.41.002672>
- Conde, M., & Smith, R. W. (1995). Mapping thermospheric winds in the auroral zone. *Geophysical Research Letters*, 22(22), 3019–3022. <https://doi.org/10.1029/95GL02437>
- Covington, A. E. (1947). Microwave sky noise. *Terrestrial Magnetism and Atmospheric Electricity*, 52(3), 339–341. <https://doi.org/10.1029/TE052i003p00339>
- Davila, R. C. (1994). A Study of Magnetic Activity Effects on the Thermospheric Winds in the Low Latitude Ionosphere, (Master thesis). Utah State University. Retrieved from Digital Commons (<https://digitalcommons.usu.edu/etd/6808>).
- Davis, T. N., & Sugiura, M. (1966). Auroral electrojet activity index *ae* and its universal time variations. *Journal of Geophysical Research (1896-1977)*, 71(3), 785–801. <https://doi.org/10.1029/JZ071i003p00785>
- Dougherty, J. P., & Farley, D. T. (1960). A theory of incoherent scattering of radio waves by a plasma. *Proceedings of the Royal Society of London. Series A. Mathematical and Physical Sciences*, 259(1296), 79–99. <https://doi.org/10.1098/rspa.1960.0212>
- Drob, D. P., Emmert, J. T., Crowley, G., Picone, J. M., Shepherd, G. G., Skinner, W., et al. (2008). An empirical model of the Earth’s horizontal wind fields: HWM07. *Journal of Geophysical Research*, 113(A12). <https://doi.org/10.1029/2008JA013668>
- Drob, D. P., Emmert, J. T., Meriwether, J. W., Makela, J. J., Doornbos, E., Conde, M., et al. (2015). An update to the Horizontal Wind Model (HWM): The quiet time thermosphere. *Earth and Space Science*, 2(7), 301–319. <https://doi.org/10.1002/2014EA000089>
- Earle, G. D., Davidson, R. L., Heelis, R. A., Coley, W. R., Weimer, D. R., Makela, J. J., et al. (2013). Low latitude thermospheric responses to magnetic storms. *Journal of Geophysical Research: Space Physics*, 118(6), 3866–3876. <https://doi.org/10.1002/jgra.50212>
- Emery, B., Lathuillere, C., Richards, P., Roble, R., Buonsanto, M., Knipp, D., et al. (1999). Time dependent thermospheric neutral response to the 2–11 November 1993 storm period. *Journal of Atmospheric and Solar-Terrestrial Physics*, 61(3), 329 – 350. [https://doi.org/10.1016/S1364-6826\(98\)00137-0](https://doi.org/10.1016/S1364-6826(98)00137-0)
- Emmert, J. T., Drob, D. P., Shepherd, G. G., Hernandez, G., Jarvis, M. J., Meriwether, J. W., et al. (2008). DWM07 global empirical model of upper thermospheric storm-induced disturbance winds. *Journal of Geophysical Research: Space Physics*, 113(A11). <https://doi.org/10.1029/2008JA013541>
- Emmert, J. T., Fejer, B. G., Fesen, C. G., Shepherd, G. G., & Solheim, B. H. (2001). Climatology of middle- and low-latitude daytime F region disturbance neutral winds measured by Wind Imaging Interferometer (WINDII). *Journal of Geophysical Research: Space Physics*, 106(A11), 24,701–24,712. <https://doi.org/10.1029/2000JA000372>

Emmert, J. T., Fejer, B. G., Shepherd, G. G., & Solheim, B. H. (2002). Altitude dependence of middle and low-latitude daytime thermospheric disturbance winds measured by WINDII. *Journal of Geophysical Research*, 107(A12), SIA 19-1-SIA 19-15. <https://doi.org/10.1029/2002JA009646>

Emmert, J. T., Fejer, B. G., Shepherd, G. G., & Solheim, B. H. (2004). Average nighttime F region disturbance neutral winds measured by UARS WINDII: Initial results. *Geophysical Research Letters*, 31(22). <https://doi.org/10.1029/2004GL021611>

Emmert, J. T., Hernandez, G., Jarvis, M. J., Niciejewski, R. J., Sipler, D. P., & Vernerstrom, S. (2006). Climatologies of nighttime upper thermospheric winds measured by ground-based Fabry-Perot interferometers during geomagnetically quiet conditions: 2. high-latitude circulation and interplanetary magnetic field dependence. *Journal of Geophysical Research: Space Physics*, 111(A12). <https://doi.org/10.1029/2006JA011949>

Fang, T.-W., Anderson, D., Fuller-Rowell, T., Akmaev, R., Codrescu, M., Millward, G., et al. (2014). Comparative Studies of Theoretical Models in the Equatorial Ionosphere. In *Modeling the ionosphere-thermosphere system* (pp. 133-144). American Geophysical Union (AGU). <https://doi.org/10.1002/9781118704417.ch12>

Farley, D. T. (1966). A theory of incoherent scattering of radio waves by a plasma: 4. The effect of unequal ion and electron temperatures. *Journal of Geophysical Research (1896-1977)*, 71(17), 4091-4098. <https://doi.org/10.1029/JZ071i017p04091>

Farley, D. T., Bonelli, E., Fejer, B. G., & Larsen, M. F. (1986). The prereversal enhancement of the zonal electric field in the equatorial ionosphere. *Journal of Geophysical Research: Space Physics*, 91(A12), 13723-13728. <https://doi.org/10.1029/JA091iA12p13723>

Farley, D. T., Ierick, H. M., & Fejer, B. G. (1981). Radar interferometry: A new technique for studying plasma turbulence in the ionosphere. *Journal of Geophysical Research: Space Physics*, 86(A3), 1467-1472. <https://doi.org/10.1029/JA086iA03p01467>

Fejer, B. G. (1981). The equatorial ionospheric electric fields. A review. *Journal of Atmospheric and Terrestrial Physics*, 43(5), 377-386. [https://doi.org/10.1016/0021-9169\(81\)90101-X](https://doi.org/10.1016/0021-9169(81)90101-X)

Fejer, B. G. (1993). F region plasma drifts over arecibo: Solar cycle, seasonal, and magnetic activity effects. *Journal of Geophysical Research: Space Physics*, 98(A8), 13645-13652. <https://doi.org/10.1029/93JA00953>

Fejer, B. G. (1997). The electrodynamics of the low-latitude ionosphere: Recent results and future challenges. *Journal of Atmospheric and Solar-Terrestrial Physics*, 59(13), 1465 - 1482. [https://doi.org/10.1016/S1364-6826\(96\)00149-6](https://doi.org/10.1016/S1364-6826(96)00149-6)

Fejer, B. G. (2002). Low latitude storm time ionospheric electrodynamics. *Journal of Atmospheric and Solar-Terrestrial Physics*, 64(12), 1401 - 1408. [https://doi.org/10.1016/S1364-6826\(02\)00103-7](https://doi.org/10.1016/S1364-6826(02)00103-7)

- Fejer, B. G. (2011). Low Latitude Ionospheric Electrodynamics. *Space Science Reviews*, 158(1), 145–166. <https://doi.org/10.1007/s11214-010-9690-7>
- Fejer, B. G., Blanc, M., & Richmond, A. D. (2017). Post-Storm Middle and Low-Latitude Ionospheric Electric Fields Effects. *Space Science Reviews*, 206(1), 407–429. <https://doi.org/10.1007/s11214-016-0320-x>
- Fejer, B. G., de Paula, E. R., González, S. A., & Woodman, R. F. (1991). Average vertical and zonal F region plasma drifts over Jicamarca. *Journal of Geophysical Research*, 96(A8), 13,901–13,906. <https://doi.org/10.1029/91JA01171>
- Fejer, B. G., & Emmert, J. T. (2003). Low-latitude ionospheric disturbance electric field effects during the recovery phase of the 19–21 October 1998 magnetic storm. *Journal of Geophysical Research*, 108(A12). <https://doi.org/10.1029/2003JA010190>
- Fejer, B. G., Emmert, J. T., Shepherd, G. G., & Solheim, B. H. (2000). Average daytime F region disturbance neutral winds measured by UARS: Initial results. *Geophysical Research Letters*, 27(13), 1859–1862. <https://doi.org/10.1029/2000GL003787>
- Fejer, B. G., Emmert, J. T., & Sipler, D. P. (2002). Climatology and storm time dependence of nighttime thermospheric neutral winds over Millstone Hill. *Journal of Geophysical Research: Space Physics*, 107(A5), SIA 3-1–SIA 3-9. <https://doi.org/10.1029/2001JA000300>
- Fejer, B. G., Farley, D. T., Woodman, R. F., & Calderon, C. (1979). Dependence of equatorial F region vertical drifts on season and solar cycle. *Journal of Geophysical Research: Space Physics*, 84(A10), 5792–5796. <https://doi.org/10.1029/JA084iA10p05792>
- Fejer, B. G., Gonzales, C. A., Farley, D. T., Kelley, M. C., & Woodman, R. F. (1979). Equatorial electric fields during magnetically disturbed conditions 1. The effect of the interplanetary magnetic field. *Journal of Geophysical Research: Space Physics*, 84(A10), 5797–5802. <https://doi.org/10.1029/JA084iA10p05797>
- Fejer, B. G., Hui, D., Chau, J. L., & Kudeki, E. (2014). Altitudinal dependence of evening equatorial F region vertical plasma drifts. *Journal of Geophysical Research: Space Physics*, 119(7), 5877–5890. <https://doi.org/10.1002/2014JA019949>
- Fejer, B. G., Jensen, J. W., Kikuchi, T., Abdu, M. A., & Chau, J. L. (2007). Equatorial ionospheric electric fields during the november 2004 magnetic storm. *Journal of Geophysical Research: Space Physics*, 112(A10). <https://doi.org/10.1029/2007JA012376>
- Fejer, B. G., Jensen, J. W., & Su, S.-Y. (2008a). Quiet time equatorial F region vertical plasma drift model derived from ROCSAT-1 observations. *Journal of Geophysical Research: Space Physics*, 113(A5). <https://doi.org/10.1029/2007JA012801>
- Fejer, B. G., Jensen, J. W., & Su, S.-Y. (2008b). Seasonal and longitudinal dependence of equatorial disturbance vertical plasma drifts. *Geophysical Research Letters*, 35(20). <https://doi.org/10.1029/2008GL035584>



- Fejer, B. G., & Kelley, M. C. (1980). Ionospheric irregularities. *Reviews of Geophysics*, 18(2), 401-454. <https://doi.org/10.1029/RG018i002p00401>
- Fejer, B. G., Kudeki, E., & Farley, D. T. (1985). Equatorial F region zonal plasma drifts. *Journal of Geophysical Research: Space Physics*, 90(A12), 12249-12255. <https://doi.org/10.1029/JA090iA12p12249>
- Fejer, B. G., Larsen, M. F., & Farley, D. T. (1983). Equatorial disturbance dynamo electric fields. *Geophysical Research Letters*, 10(7), 537-540. <https://doi.org/10.1029/GL010i007p00537>
- Fejer, B. G., & Scherliess, L. (1995). Time dependent response of equatorial ionospheric electric fields to magnetospheric disturbances. *Geophysical Research Letters*, 22(7), 851-854. <https://doi.org/10.1029/95GL00390>
- Fejer, B. G., & Scherliess, L. (1997). Empirical models of storm time equatorial zonal electric fields. *Journal of Geophysical Research: Space Physics*, 102(A11), 24047-24056. <https://doi.org/10.1029/97JA02164>
- Fejer, B. G., & Scherliess, L. (1998). Mid- and low-latitude prompt-penetration ionospheric zonal plasma drifts. *Geophysical Research Letters*, 25(16), 3071-3074. <https://doi.org/10.1029/98GL02325>
- Fejer, B. G., & Scherliess, L. (2001). On the variability of equatorial F-region vertical plasma drifts. *Journal of Atmospheric and Solar-Terrestrial Physics*, 63(9), 893 - 897. [https://doi.org/10.1016/S1364-6826\(00\)00198-X](https://doi.org/10.1016/S1364-6826(00)00198-X)
- Fejer, B. G., Scherliess, L., & de Paula, E. R. (1999). Effects of the vertical plasma drift velocity on the generation and evolution of equatorial spread F. *Journal of Geophysical Research*, 104(A9), 19859-19869. <https://doi.org/10.1029/1999JA900271>
- Fejer, B. G., Souza, J. R., Santos, A. S., & Costa Pereira, A. E. (2005). Climatology of F region zonal plasma drifts over Jicamarca. *Journal of Geophysical Research*, 110(A12). <https://doi.org/10.1029/2005JA011324>
- Fejer, B. G., Spiro, R. W., Wolf, R. A., & Foster, J. C. (1990). Latitudinal variation of perturbation electric fields during magnetically disturbed periods-1986 SUNDIAL observations and model results. In *Annales geophysicae* (Vol. 8, pp. 441-454).
- Fejer, B. G., Tracy, B. D., Olson, M. E., & Chau, J. L. (2011). Enhanced lunar semidiurnal equatorial vertical plasma drifts during sudden stratospheric warmings. *Geophysical Research Letters*, 38(21). <https://doi.org/10.1029/2011GL049788>
- Fejer, B. G., Tracy, B. D., & Pfaff, R. F. (2013). Equatorial zonal plasma drifts measured by the c/nofs satellite during the 2008-2011 solar minimum. *Journal of Geophysical Research: Space Physics*, 118(6), 3891-3897. <https://doi.org/10.1002/jgra.50382>
- Fesen, C. G., Hysell, D. L., Meriwether, J. M., Mendillo, M., Fejer, B. G., Roble, R. G., et al. (2002). Modeling the low-latitude thermosphere and iono-

sphere. *Journal of Atmospheric and Solar-Terrestrial Physics*, 64(12), 1337–1349. [https://doi.org/https://doi.org/10.1016/S1364-6826\(02\)00098-6](https://doi.org/https://doi.org/10.1016/S1364-6826(02)00098-6)

Fisher, D. J., Makela, J. J., Meriwether, J. W., Buriti, R. A., Benkhaldoun, Z., Kaab, M., et al. (2015). Climatologies of nighttime thermospheric winds and temperatures from Fabry-Perot interferometer measurements: From solar minimum to solar maximum. *Journal of Geophysical Research: Space Physics*, 120(8), 6679–6693. <https://doi.org/10.1002/2015JA021170>

Fuller-Rowell, T. J., Codrescu, M. V., Moffett, R. J., & Quegan, S. (1994). Response of the thermosphere and ionosphere to geomagnetic storms. *Journal of Geophysical Research: Space Physics*, 99(A3), 3893–3914. <https://doi.org/10.1029/93JA02015>

Fuller-Rowell, T. J., Codrescu, M. V., Rishbeth, H., Moffett, R. J., & Quegan, S. (1996). On the seasonal response of the thermosphere and ionosphere to geomagnetic storms. *Journal of Geophysical Research*, 101(A2), 2343–2353. <https://doi.org/10.1029/95JA01614>

Fuller-Rowell, T. J., Codrescu, M. V., Roble, R. G., & Richmond, A. D. (2013). How Does the Thermosphere and Ionosphere React to a Geomagnetic Storm? In *Magnetic storms* (pp. 203–225). American Geophysical Union (AGU). <https://doi.org/10.1029/GM098p0203>

Fuller-Rowell, T. J., Millward, G. H., Richmond, A. D., & Codrescu, M. V. (2002). Storm-time changes in the upper atmosphere at low latitudes. *Journal of Atmospheric and Solar-Terrestrial Physics*, 64(12), 1383–1391. [https://doi.org/10.1016/S1364-6826\(02\)00101-3](https://doi.org/10.1016/S1364-6826(02)00101-3)

Fuller-Rowell, T. J., Richmond, A. D., & Maruyama, N. (2013). Global Modeling of Storm-Time Thermospheric Dynamics and Electrodynamics. In *Midlatitude ionospheric dynamics and disturbances* (pp. 187–200). American Geophysical Union (AGU). <https://doi.org/10.1029/181GM18>

Gerrard, A. J., & Meriwether, J. W. (2011). Initial daytime and nighttime SOFDI observations of thermospheric winds from Fabry-Perot Doppler shift measurements of the 630-nm OI line-shape profile. *Ann. Geophys.*, 29(9), 1529–1536. <https://doi.org/10.5194/angeo-29-1529-2011>

Gonzalez, W. D., Joselyn, J. A., Kamide, Y., Kroehl, H. W., Rostoker, G., Tsurutani, B. T., et al. (1994). What is a geomagnetic storm? *Journal of Geophysical Research: Space Physics*, 99(A4), 5771–5792. <https://doi.org/10.1029/93JA02867>

Harding, B. J., Gehrels, T. W., & Makela, J. J. (2014). Nonlinear regression method for estimating neutral wind and temperature from Fabry-Perot interferometer data. *Applied Optics*, 53(4), 666–673. <https://doi.org/10.1364/AO.53.000666>

Harding, B. J., Makela, J. J., & Meriwether, J. W. (2015). Estimation of mesoscale thermospheric wind structure using a network of interferometers. *Journal of Geophysical Research: Space Physics*, 120(5), 3928–3940. <https://doi.org/10.1002/2015JA021025>

Häusler, K., & Lühr, H. (2011). Longitudinal Variations of the Thermospheric Zonal Wind

Induced by Nonmigrating Tides as Observed by CHAMP. In M. A. Abdu & D. Pancheva (Eds.), *Aeronomy of the earth's atmosphere and ionosphere* (pp. 339–348). Dordrecht: Springer Netherlands. [https://doi.org/10.1007/978-94-007-0326-1\\_25](https://doi.org/10.1007/978-94-007-0326-1_25)

Hays, P. B., & Roble, R. G. (1971). A Technique for Recovering Doppler Line Profiles from Fabry-Perot Interferometer Fringes of Very Low Intensity. *Applied Optics*, 10(1), 193–200. <https://doi.org/10.1364/AO.10.000193>

Hedin, A. E., Biondi, M. A., Burnside, R. G., Hernandez, G., Johnson, R. M., Killeen, T. L., et al. (1991). Revised global model of thermosphere winds using satellite and ground-based observations. *Journal of Geophysical Research: Space Physics*, 96(A5), 7657–7688. <https://doi.org/10.1029/91JA00251>

Hedin, A. E., Fleming, E. L., Manson, A. H., Schmidlin, F. J., Avery, S. K., Clark, R. R., et al. (1996). Empirical wind model for the upper, middle and lower atmosphere. *Journal of Atmospheric and Terrestrial Physics*, 58(13), 1421–1447. [https://doi.org/10.1016/0021-9169\(95\)00122-0](https://doi.org/10.1016/0021-9169(95)00122-0)

Hedin, A. E., Spencer, N. W., & Killeen, T. L. (1988). Empirical global model of upper thermosphere winds based on Atmosphere and Dynamics Explorer satellite data. *Journal of Geophysical Research: Space Physics*, 93(A9), 9959–9978. <https://doi.org/10.1029/JA093iA09p09959>

Heelis, R. (2004). Electrodynamics in the low and middle latitude ionosphere: a tutorial. *Journal of Atmospheric and Solar-Terrestrial Physics*, 66(10), 825 - 838. <https://doi.org/10.1016/j.jastp.2004.01.034>

Hernandez, G. (1966). Analytical Description of a Fabry–Perot Photoelectric Spectrometer. *Applied Optics*, 5(11), 1745–1748. <https://doi.org/10.1364/AO.5.001745>

Hernandez, G. (1971). The signature profiles of O(1S) In the airglow. *Planetary and Space Science*, 19(5), 467–476. [https://doi.org/10.1016/0032-0633\(71\)90162-0](https://doi.org/10.1016/0032-0633(71)90162-0)

Hernandez, G. (1988). *Fabry-perot interferometers*. Cambridge University Press.

Huang, C. M. (2013). Disturbance dynamo electric fields in response to geomagnetic storms occurring at different universal times. *Journal of Geophysical Research: Space Physics*, 118(1), 496–501. <https://doi.org/10.1029/2012JA018118>

Huang, C. M., & Chen, M. Q. (2008). Formation of maximum electric potential at the geomagnetic equator by the disturbance dynamo. *Journal of Geophysical Research: Space Physics*, 113(A3). <https://doi.org/10.1029/2007JA012843>

Huang, C. M., Richmond, A. D., & Chen, M.-Q. (2005). Theoretical effects of geomagnetic activity on low-latitude ionospheric electric fields. *Journal of Geophysical Research*, 110(A5). <https://doi.org/10.1029/2004JA010994>

Huang, C.-S., & Roddy, P. A. (2016). Effects of solar and geomagnetic activities on the zonal drift of equatorial plasma bubbles. *Journal of Geophysical Research: Space Physics*,

121(1), 628-637. <https://doi.org/10.1002/2015JA021900>

Hui, D., & Fejer, B. G. (2015). Daytime plasma drifts in the equatorial lower ionosphere. *Journal of Geophysical Research: Space Physics*, 120(11), 9738–9747. <https://doi.org/10.1002/2015JA021838>

Hysell, D. L., Chau, J. L., & Milla, M. A. (2013). The Jicamarca phased-array radar. In *2013 IEEE International Symposium on Phased Array Systems and Technology* (pp. 669-675). <https://doi.org/10.1109/ARRAY.2013.6731910>

Hysell, D. L., Milla, M. A., & Woodman, R. F. (2017). High-altitude incoherent-scatter measurements at Jicamarca. *Journal of Geophysical Research: Space Physics*, 122(2), 2292–2299. <https://doi.org/10.1002/2016JA023569>

Jacchia, L. G., & Slowey, J. (1966). The Shape and Location of the Diurnal Bulge in the Upper Atmosphere. *SAO Special Report*, 207.

Jensen, W. J. (2007). Climatology of Middle and Low-Latitude F-Region Plasma Drifts from Satellite Measurements, (Doctoral dissertation). Logan, Utah: Utah State University. Retrieved from Digital Commons (<https://digitalcommons.usu.edu/etd/7444>).

Joshi, P. P., H. Baker, J. B., Ruohoniemi, J. M., Makela, J. J., Fisher, D. J., Harding, B. J., et al. (2015). Observations of storm time midlatitude ion-neutral coupling using superdarn radars and nation fabry-perot interferometers. *Journal of Geophysical Research: Space Physics*, 120(10), 8989-9003. <https://doi.org/10.1002/2015JA021475>

Kakad, B., Tiwari, D., & Pant, T. K. (2011). Study of disturbance dynamo effects at nighttime equatorial F region in Indian longitude. *Journal of Geophysical Research*, 116(A12). <https://doi.org/10.1029/2011JA016626>

Kelley, M. C. (2009). *The Earth's Ionosphere: Plasma Physics & Electrodynamics* (2nd ed., Vol. 96). Academic Press.

Kelley, M. C., Fejer, B. G., & Gonzales, C. A. (1979). An explanation for anomalous equatorial ionospheric electric fields associated with a northward turning of the interplanetary magnetic field. *Geophysical Research Letters*, 6(4), 301-304. <https://doi.org/10.1029/GL006i004p00301>

Kelley, M. C., Makela, J. J., Chau, J. L., & Nicolls, M. J. (2003). Penetration of the solar wind electric field into the magnetosphere/ionosphere system. *Geophysical Research Letters*, 30(4). <https://doi.org/10.1029/2002GL016321>

Kikuchi, T., & Hashimoto, K. K. (2016). Transmission of the electric fields to the low latitude ionosphere in the magnetosphere-ionosphere current circuit. *Geoscience Letters*, 3(1), 4. <https://doi.org/10.1186/s40562-016-0035-6>

Kudeki, E., Bhattacharyya, S., & Woodman, R. F. (1999). A new approach in incoherent scatter F region  $E \times B$  drift measurements at Jicamarca. *Journal of Geophysical Research*, 104(A12), 28145-28162. <https://doi.org/10.1029/1998JA900110>

- Liu, H.-L., Bardeen, C. G., Foster, B. T., Lauritzen, P., Liu, J., Lu, G., et al. (2018). Development and Validation of the Whole Atmosphere Community Climate Model With Thermosphere and Ionosphere Extension (WACCM-X 2.0). *Journal of Advances in Modeling Earth Systems*, 10(2), 381–402. <https://doi.org/10.1002/2017MS001232>
- Makela, J. J., Fisher, D. J., Meriwether, J. W., Buriti, R. A., & Medeiros, A. F. (2013). Near-continual ground-based nighttime observations of thermospheric neutral winds and temperatures over equatorial Brazil from 2009 to 2012. *Journal of Atmospheric and Solar-Terrestrial Physics*, 103, 94 – 102. <https://doi.org/10.1016/j.jastp.2012.11.019>
- Makela, J. J., Meriwether, J. W., Huang, Y., & Sherwood, P. J. (2011). Simulation and analysis of a multi-order imaging Fabry–Perot interferometer for the study of thermospheric winds and temperatures. *Applied Optics*, 50(22), 4403–4416. <https://doi.org/10.1364/AO.50.004403>
- Makela, J. J., Meriwether, J. W., Lima, J. P., Miller, E. S., & Armstrong, S. J. (2009). The Remote Equatorial Nighttime Observatory of Ionospheric Regions Project and the International Heliospherical Year. *Earth, Moon, and Planets*, 104(1), 211–226. <https://doi.org/10.1007/s11038-008-9289-0>
- Makela, J. J., Meriwether, J. W., Ridley, A. J., Ciocca, M., & Castellez, M. W. (2012). Large-Scale Measurements of Thermospheric Dynamics with a Multisite Fabry-Perot Interferometer Network: Overview of Plans and Results from Midlatitude Measurements. *International Journal of Geophysics*, 2012. <https://doi.org/10.1155/2012/872140>
- Malki, K., Bounhir, A., Benkhaldoun, Z., Makela, J. J., Vilmer, N., Fisher, D. J., et al. (2018). Ionospheric and thermospheric response to the 27–28 February 2014 geomagnetic storm over north Africa. *Annales Geophysicae*, 36(4), 987–998. <https://doi.org/10.5194/angeo-36-987-2018>
- Manoj, C., Maus, S., Lühr, H., & Alken, P. (2008). Penetration characteristics of the interplanetary electric field to the daytime equatorial ionosphere. *Journal of Geophysical Research: Space Physics*, 113(A12). <https://doi.org/10.1029/2008JA013381>
- Martinis, C., Eccles, J. V., Baumgardner, J., Manzano, J., & Mendillo, M. (2003). Latitude dependence of zonal plasma drifts obtained from dual-site airglow observations. *Journal of Geophysical Research*, 108(A3). <https://doi.org/10.1029/2002JA009462>
- Martinis, C., Meriwether, J., Niciejewski, R., Biondi, M., Fesen, C., & Mendillo, M. (2001). Zonal neutral winds at equatorial and low latitudes. *Journal of Atmospheric and Solar-Terrestrial Physics*, 63(14), 1559–1569. [https://doi.org/10.1016/S1364-6826\(01\)00022-0](https://doi.org/10.1016/S1364-6826(01)00022-0)
- Mayaud, P. N. (1980). *Derivation, meaning, and use of geomagnetic indices* (Vol. 22). Washington, D. C.: American Geophysical Union (AGU). <https://doi.org/10.1029/GM022>
- Mazaudier, C., & Venkateswaran, S. V. (1990). Delayed ionospheric effects of March 22, 1979 studied by the sixth co-ordinated data analysis workshop (CDAW-6). *Annales Geophysicae*, 8, 511–518.

- Meriwether, J. W. (2013). Thermospheric Dynamics at Low and Mid-Latitudes During Magnetic Storm Activity. In *Midlatitude ionospheric dynamics and disturbances* (pp. 201-219). American Geophysical Union (AGU). <https://doi.org/10.1029/181GM19>
- Meriwether, J. W., Faivre, M., Fesen, C., Sherwood, P., & Veliz, O. (2008). New results on equatorial thermospheric winds and the midnight temperature maximum. *Annales Geophysicae*, 26(3), 447–466. <https://doi.org/10.5194/angeo-26-447-2008>
- Meriwether, J. W., Makela, J., Fisher, D., Buriti, R., Medeiros, A., Akmaev, R., et al. (2013). Comparisons of thermospheric wind and temperature measurements in equatorial Brazil to Whole Atmosphere Model Predictions. *Journal of Atmospheric and Solar-Terrestrial Physics*, 103, 103 - 112. <https://doi.org/10.1016/j.jastp.2013.04.002>
- Meriwether, J. W., Makela, J. J., & Fisher, D. J. (2016). Simultaneous Measurements and Monthly Climatologies of Thermospheric Winds and Temperatures in the Peruvian and Brazilian Longitudinal Sectors. In *Ionospheric space weather* (pp. 175-186). Switzerland: American Geophysical Union (AGU). <https://doi.org/10.1002/9781118929216.ch15>
- Meriwether, J. W., Makela, J. J., Huang, Y., Fisher, D. J., Buriti, R. A., Medeiros, A. F., et al. (2011). Climatology of the nighttime equatorial thermospheric winds and temperatures over Brazil near solar minimum. *Journal of Geophysical Research*, 116(A4). <https://doi.org/10.1029/2011JA016477>
- Meriwether, J. W., Moody, J. W., Biondi, M. A., & Roble, R. G. (1986). Optical interferometric measurements of nighttime equatorial thermospheric winds at Arequipa, Peru. *Journal of Geophysical Research*, 91(A5), 5557-5566. <https://doi.org/10.1029/JA091iA05p05557>
- Mesquita, R. L. A., Meriwether, J. W., Makela, J. J., Fisher, D. J., Harding, B. J., Sanders, S. C., et al. (2018). New results on the mid-latitude midnight temperature maximum. *Annales Geophysicae*, 36(2), 541–553. <https://doi.org/10.5194/angeo-36-541-2018>
- Navarro, L. A., & Fejer, B. G. (2019). Storm-Time Thermospheric Winds Over Peru. *Journal of Geophysical Research: Space Physics*, 124(12), 10415–10427. <https://doi.org/10.1029/2019JA027256>
- Newell, P. T., Sotirelis, T., Liou, K., Meng, C.-I., & Rich, F. J. (2007). A nearly universal solar wind-magnetosphere coupling function inferred from 10 magnetospheric state variables. *Journal of Geophysical Research*, 112(A1). <https://doi.org/10.1029/2006JA012015>
- Ochs, G. R. (1965). *The large 50 Mc/s dipole array at Jicamarca radar observatory* (Tech. Rep. No. 8772). National Bureau of Standards.
- Oughton, E. J., Skelton, A., Horne, R. B., Thomson, A. W. P., & Gaunt, C. T. (2017). Quantifying the daily economic impact of extreme space weather due to failure in electricity transmission infrastructure. *Space Weather*, 15(1), 65-83. <https://doi.org/10.1002/2016SW001491>
- Pandey, K., Chakrabarty, D., & Sekar, R. (2018). Critical Evaluation of the Impact of



Disturbance Dynamo on Equatorial Ionosphere During Daytime. *Journal of Geophysical Research: Space Physics*, 123(11), 9762-9774. <https://doi.org/10.1029/2018JA025686>

Pingree, J. E. (1990). Incoherent Scatter Measurements and Inferred Energy Fluxes in the Equatorial F-region Ionosphere, (Doctoral dissertation). Itaca, New York: Cornell University.

Pingree, J. E., & Fejer, B. G. (1987). On the height variation of the equatorial F region vertical plasma drifts. *Journal of Geophysical Research: Space Physics*, 92(A5), 4763-4766. <https://doi.org/10.1029/JA092iA05p04763>

Prölss, G. W. (1993). Common origin of positive ionospheric storms at middle latitudes and the geomagnetic activity effect at low latitudes. *Journal of Geophysical Research: Space Physics*, 98(A4), 5981-5991. <https://doi.org/10.1029/92JA02777>

Prölss, G. W. (2004). *Physics of the earth's space environment*. Springer Berlin Heidelberg. <https://doi.org/10.1007/978-3-642-97123-5>

Qian, L., Burns, A. G., Emery, B. A., Foster, B., Lu, G., Maute, A., et al. (2014). The near tie-gcm. In *Modeling the ionosphere-thermosphere system* (pp. 73-83). American Geophysical Union (AGU). <https://doi.org/10.1002/9781118704417.ch7>

Ren, Z., Wan, W., Liu, L., Chen, Y., & Le, H. (2011). Equinoctial asymmetry of ionospheric vertical plasma drifts and its effect on F-region plasma density. *Journal of Geophysical Research*, 116(A2). <https://doi.org/10.1029/2010JA016081>

Richmond, A. D. (1978). Gravity wave generation, propagation, and dissipation in the thermosphere. *Journal of Geophysical Research*, 83(A9), 4131-4145. <https://doi.org/10.1029/JA083iA09p04131>

Richmond, A. D. (1979a). Large-amplitude gravity wave energy production and dissipation in the thermosphere. *Journal of Geophysical Research*, 84(A5), 1880-1890. <https://doi.org/10.1029/JA084iA05p01880>

Richmond, A. D. (1979b). Thermospheric heating in a magnetic storm: Dynamic transport of energy from high to low latitudes. *Journal of Geophysical Research*, 84(A9), 5259-5266. <https://doi.org/10.1029/JA084iA09p05259>

Richmond, A. D. (1995a). The ionospheric wind dynamo: Effects of its coupling with different atmospheric regions. In *The upper mesosphere and lower thermosphere: A review of experiment and theory* (pp. 49-65). American Geophysical Union (AGU). <https://doi.org/10.1029/GM087p0049>

Richmond, A. D. (1995b). Modeling equatorial ionospheric electric fields. *Journal of Atmospheric and Terrestrial Physics*, 57(10), 1103 - 1115. (The Equatorial Ionosphere-Thermosphere Coupling and Dynamics Symposium) [https://doi.org/10.1016/0021-9169\(94\)00126-9](https://doi.org/10.1016/0021-9169(94)00126-9)

Richmond, A. D. (2011). Electrodynamics of Ionosphere-Thermosphere Coupling. In

- M. A. Abdu & D. Pancheva (Eds.), *Aeronomy of the earth's atmosphere and ionosphere* (pp. 191–201). Dordrecht, Netherlands: Springer. [https://doi.org/10.1007/978-94-007-0326-1\\_13](https://doi.org/10.1007/978-94-007-0326-1_13)
- Richmond, A. D. (2016). Ionospheric electrodynamics. In G. V. Khazanov (Ed.), (chap. 14). CRC Press.
- Richmond, A. D., & Matsushita, S. (1975). Thermospheric response to a magnetic substorm. *Journal of Geophysical Research (1896-1977)*, 80(19), 2839–2850. <https://doi.org/10.1029/JA080i019p02839>
- Richmond, A. D., & Maute, A. (2014). Ionospheric Electrodynamics Modeling. In *Modeling the ionosphere-thermosphere system* (pp. 57–71). American Geophysical Union (AGU). <https://doi.org/10.1002/9781118704417.ch6>
- Richmond, A. D., Ridley, E. C., & Roble, R. G. (1992). A thermosphere/ionosphere general circulation model with coupled electrodynamics. *Geophysical Research Letters*, 19(6), 601–604. <https://doi.org/10.1029/92GL00401>
- Rishbeth, H. (1971a). The F-layer dynamo. *Planetary and Space Science*, 19(2), 263 - 267. [https://doi.org/10.1016/0032-0633\(71\)90205-4](https://doi.org/10.1016/0032-0633(71)90205-4)
- Rishbeth, H. (1971b). Polarization fields produced by winds in the equatorial F-region. *Planetary and Space Science*, 19(3), 357–369. [https://doi.org/10.1016/0032-0633\(71\)90098-5](https://doi.org/10.1016/0032-0633(71)90098-5)
- Rishbeth, H. (1972a). Superrotation of the upper atmosphere. *Reviews of Geophysics*, 10(3), 799–819. <https://doi.org/10.1029/RG010i003p00799>
- Rishbeth, H. (1972b). Thermospheric winds and the F-region: A review. *Journal of Atmospheric and Terrestrial Physics*, 34(1), 1 - 47. [https://doi.org/10.1016/0021-9169\(72\)90003-7](https://doi.org/10.1016/0021-9169(72)90003-7)
- Rishbeth, H. (1975). F-region storms and thermospheric circulation. *Journal of Atmospheric and Terrestrial Physics*, 37(6), 1055 - 1064. [https://doi.org/10.1016/0021-9169\(75\)90013-6](https://doi.org/10.1016/0021-9169(75)90013-6)
- Rishbeth, H., & Garriot, O. (1969). *Introduction to ionospheric physics* (1st ed.). New York: Academic Press.
- Rishbeth, H., Müller-Wodarg, I. C. F., Zou, L., Fuller-Rowell, T. J., Millward, G. H., Moffett, R. J., et al. (2000). Annual and semiannual variations in the ionospheric F2-layer: II. Physical discussion. *Annales Geophysicae*, 18(8), 945–956. <https://doi.org/10.1007/s00585-000-0945-6>
- Roble, R. G., Ridley, E. C., Richmond, A. D., & Dickinson, R. E. (1988). A coupled thermosphere/ionosphere general circulation model. *Geophysical Research Letters*, 15(12), 1325–1328. <https://doi.org/10.1029/GL015i012p01325>



- Rodrigues, F. S., Crowley, G., Heelis, R. A., Maute, A., & Reynolds, A. (2012). On TIE-GCM simulation of the evening equatorial plasma vortex. *Journal of Geophysical Research: Space Physics*, 117(A5). <https://doi.org/10.1029/2011JA017369>
- Rodrigues, F. S., Hickey, D. A., Zhan, W., Martinis, C. R., Fejer, B. G., Milla, M. A., et al. (2018). Multi-instrumented observations of the equatorial F-region during June solstice: large-scale wave structures and spread-F. *Progress in Earth and Planetary Science*, 5(1), 14. <https://doi.org/10.1186/s40645-018-0170-0>
- Santos, A. M., Abdu, M. A., Souza, J. R., Sobral, J. H. A., & Batista, I. S. (2016). Disturbance zonal and vertical plasma drifts in the Peruvian sector during solar minimum phases. *Journal of Geophysical Research: Space Physics*, 121(3), 2503–2521. <https://doi.org/10.1002/2015JA022146>
- Sazykin, S. (2000). Theoretical Studies of Penetration of Magnetospheric Electric Fields to the Ionosphere, (Doctoral dissertation). Utah State University. Retrieved from Digital Commons (<https://digitalcommons.usu.edu/etd/7152>).
- Scherliess, L. (1997). Empirical Studies of Ionospheric Electric Fields, (Doctoral dissertation). Logan, Utah: Utah State University. Retrieved from Digital Commons (<https://digitalcommons.usu.edu/etd/6823>).
- Scherliess, L., & Fejer, B. G. (1997). Storm time dependence of equatorial disturbance dynamo zonal electric fields. *Journal of Geophysical Research*, 102(A11), 24,037–24,046. <https://doi.org/10.1029/97JA02165>
- Scherliess, L., & Fejer, B. G. (1999). Radar and satellite global equatorial F region vertical drift model. *Journal of Geophysical Research: Space Physics*, 104(A4), 6829–6842. <https://doi.org/10.1029/1999JA900025>
- Schunk, R., & Nagy, A. (2009). *Ionospheres: Physics, Plasma Physics, and Chemistry*. Cambridge: Cambridge University Press. <https://doi.org/10.1017/CBO9780511635342>
- Shidler, S. A., & Rodrigues, F. S. (2019). On the Magnitude and Variability of Height Gradients in the Equatorial F Region Vertical Plasma Drifts. *Journal of Geophysical Research: Space Physics*, 124(6), 4916–4925. <https://doi.org/10.1029/2019JA026661>
- Shidler, S. A., Rodrigues, F. S., Fejer, B. G., & Milla, M. A. (2019). Radar Studies of Height-Dependent Equatorial F region Vertical and Zonal Plasma Drifts. *Journal of Geophysical Research: Space Physics*, 124(3), 2058–2071. <https://doi.org/10.1029/2019JA026476>
- Siddiqui, T. A., Lühr, H., Stolle, C., & Park, J. (2015). Relation between stratospheric sudden warming and the lunar effect on the equatorial electrojet based on Huancayo recordings. *Annales Geophysicae*, 33(2), 235–243. <https://doi.org/10.5194/angeo-33-235-2015>
- Sipler, D. P., & Biondi, M. A. (2003). Simulation of hot oxygen effects on ground-based Fabry-Perot determinations of thermospheric temperatures. *Journal of Geophysical Research: Space Physics*, 108(A6). <https://doi.org/10.1029/2003JA009911>

- Stoneback, R. A., Heelis, R. A., Burrell, A. G., Coley, W. R., Fejer, B. G., & Pacheco, E. (2011). Observations of quiet time vertical ion drift in the equatorial ionosphere during the solar minimum period of 2009. *Journal of Geophysical Research: Space Physics*, 116(A12). <https://doi.org/10.1029/2011JA016712>
- Tapping, K. F. (2013). The 10.7 cm solar radio flux (f10.7). *Space Weather*, 11(7), 394–406. <https://doi.org/10.1002/swe.20064>
- Tesema, F., Mesquita, R., Meriwether, J., Damtie, B., Nigussie, M., Makela, J., et al. (2017). New results on equatorial thermospheric winds and temperatures from Ethiopia, Africa. *Annales Geophysicae*, 35(2), 333–344. <https://doi.org/10.5194/angeo-35-333-2017>
- Valladares, C. E., Meriwether, J. W., Sheehan, R., & Biondi, M. A. (2002). Correlative study of neutral winds and scintillation drifts measured near the magnetic equator. *Journal of Geophysical Research: Space Physics*, 107(A7), SIA 7-1-SIA 7-15. <https://doi.org/10.1029/2001JA000042>
- Valladares, C. E., Sheehan, R., Basu, S., Kuenzler, H., & Espinoza, J. (1996). The multi-instrumented studies of equatorial thermosphere aeronomy scintillation system: Climatology of zonal drifts. *Journal of Geophysical Research*, 101(A12), 26,839–26,850. <https://doi.org/10.1029/96JA00183>
- Vineeth, C., Ajesh, A., Pant, T. K., & Ruohoniemi, J. M. (2019). Response of thermospheric nightglow emissions over the magnetic equator to prompt penetration electric field events. *Journal of Geophysical Research: Space Physics*, 124(7), 5918–5935. <https://doi.org/10.1029/2018JA026317>
- Wanliss, J. A., & Showalter, K. M. (2006). High-resolution global storm index: Dst versus sym-h. *Journal of Geophysical Research: Space Physics*, 111(A2). <https://doi.org/10.1029/2005JA011034>
- Wolf, R. A. (1995). Magnetospheric configuration. In M. G. Kivelson & C. T. Russell (Eds.), *Introduction to space physics* (pp. 288–329). New York: Cambridge University Press.
- Woodman, R. F. (1970). Vertical drift velocities and east-west electric fields at the magnetic equator. *Journal of Geophysical Research (1896-1977)*, 75(31), 6249–6259. <https://doi.org/10.1029/JA075i031p06249>
- Woodman, R. F. (1971). Inclination of the geomagnetic field measured by an incoherent scatter technique. *Journal of Geophysical Research (1896-1977)*, 76(1), 178–184. <https://doi.org/10.1029/JA076i001p00178>
- Woodman, R. F. (1972). East-west ionospheric drifts at the magnetic equator. In *14th plenary meeting on space research xii*.
- Woodman, R. F., Farley, D. T., Balsley, B. B., & Milla, M. A. (2019). The early history of the Jicamarca Radio Observatory and the incoherent scatter technique. *History of Geo-*

and *Space Sciences*, 10(2), 245–266. <https://doi.org/10.5194/hgss-10-245-2019>

Woodman, R. F., & Hagfors, T. (1969). Methods for the measurement of vertical ionospheric motions near the magnetic equator by incoherent scattering. *Journal of Geophysical Research (1896-1977)*, 74(5), 1205–1212. <https://doi.org/10.1029/JA074i005p01205>

Wu, Q., Killeen, T. L., & Spencer, N. W. (1994). Dynamics explorer 2 observations of equatorial thermospheric winds and temperatures: Local time and longitudinal dependences. *Journal of Geophysical Research: Space Physics*, 99(A4), 6277–6288. <https://doi.org/10.1029/93JA02521>

Xiong, C., Lühr, H., & Fejer, B. G. (2015). Global features of the disturbance winds during storm time deduced from CHAMP observations. *Journal of Geophysical Research: Space Physics*, 120(6), 5137–5150. <https://doi.org/10.1002/2015JA021302>

Xiong, C., Lühr, H., & Fejer, B. G. (2016). The response of equatorial electrojet, vertical plasma drift, and thermospheric zonal wind to enhanced solar wind input. *Journal of Geophysical Research: Space Physics*, 121(6), 5653–5663. <https://doi.org/10.1002/2015JA022133>

Yamazaki, Y., & Kosch, M. J. (2015). The equatorial electrojet during geomagnetic storms and substorms. *Journal of Geophysical Research: Space Physics*, 120(3), 2276–2287. <https://doi.org/10.1002/2014JA020773>

Yee, J.-h. (1988). Non-thermal distribution of O(1D) atoms in the night-time thermosphere. *Planetary and Space Science*, 36(1), 89–97. [https://doi.org/https://doi.org/10.1016/0032-0633\(88\)90149-3](https://doi.org/https://doi.org/10.1016/0032-0633(88)90149-3)

Zhang, K., Liu, J., Wang, W., & Wang, H. (2019). The effects of imf bz periodic oscillations on thermospheric meridional winds. *Journal of Geophysical Research: Space Physics*, 124(7), 5800–5815. <https://doi.org/10.1029/2019JA026527>

Zhang, R., Liu, L., Le, H., & Chen, Y. (2017). Equatorial ionospheric electrodynamics during solar flares. *Geophysical Research Letters*, 44(10), 4558–4565. <https://doi.org/10.1002/2017GL073238>

Zhang, R., Liu, L., Le, H., Chen, Y., & Kuai, J. (2017). The Storm Time Evolution of the Ionospheric Disturbance Plasma Drifts. *Journal of Geophysical Research: Space Physics*, 122(11), 11,665–11,676. <https://doi.org/10.1002/2017JA024637>

Zhang, S.-R., Erickson, P. J., Zhang, Y., Wang, W., Huang, C., Coster, A. J., et al. (2017). Observations of ion-neutral coupling associated with strong electrodynamic disturbances during the 2015 St. Patrick's Day storm. *Journal of Geophysical Research: Space Physics*, 122(1), 1314–1337. <https://doi.org/10.1002/2016JA023307>

## APPENDIX

Material (Figures, Tables and text) in chapter 4 is copyrighted and reused with permission.

## JOHN WILEY AND SONS LICENSE TERMS AND CONDITIONS

Mar 13, 2020

This Agreement between Utah State University -- Luis Navarro ("You") and John Wiley and Sons ("John Wiley and Sons") consists of your license details and the terms and conditions provided by John Wiley and Sons and Copyright Clearance Center.

License Number	4786191098129
License date	Mar 11, 2020
Licensed Content Publisher	John Wiley and Sons
Licensed Content Publication	Journal of Geophysical Research: Space Physics
Licensed Content Title	Storm-Time Thermospheric Winds Over Peru
Licensed Content Author	L. A. Navarro, B. G. Fejer
Licensed Content Date	Dec 4, 2019
Licensed Content Volume	124
Licensed Content Issue	12
Licensed Content Pages	13
Type of Use	Dissertation/Thesis
Requestor type	Author of this Wiley article
Format	Print and electronic
Portion	Full article
Will you be translating?	No
Title of your thesis / dissertation	Storm-Time Equatorial Thermospheric Dynamics and Electrodynamics
Expected completion date	Apr 2020
Expected size (number of pages)	150
Requestor Location	Utah State University
	LOGAN, UT 84321
	United States
	Attn: Utah State University
Publisher Tax ID	EU826007151

Material (Figures, Tables and text) in chapter 5 is copyrighted and reused with permission.

## JOHN WILEY AND SONS LICENSE TERMS AND CONDITIONS

Mar 13, 2020

This Agreement between Utah State University -- Luis Navarro ("You") and John Wiley and Sons ("John Wiley and Sons") consists of your license details and the terms and conditions provided by John Wiley and Sons and Copyright Clearance Center.

License Number	4786191152223
License date	Mar 11, 2020
Licensed Content Publisher	John Wiley and Sons
Licensed Content Publication	Journal of Geophysical Research: Space Physics
Licensed Content Title	Equatorial Disturbance Dynamo Vertical Plasma Drifts Over Jicamarca: Bimonthly and Solar Cycle Dependence
Licensed Content Author	L. A. Navarro, B. G. Fejer, L. Scherliess
Licensed Content Date	Jun 25, 2019
Licensed Content Volume	124
Licensed Content Issue	6
Licensed Content Pages	9
Type of Use	Dissertation/Thesis
Requestor type	Author of this Wiley article
Format	Print and electronic
Portion	Full article
Will you be translating?	No
Title of your thesis / dissertation	Storm-Time Equatorial Thermospheric Dynamics and Electrodynamics
Expected completion date	Apr 2020
Expected size (number of pages)	150
Requestor Location	Utah State University
	LOGAN, UT 84321
	United States
	Attn: Utah State University
Publisher Tax ID	EU826007151

Figure 1.1 is copyrighted and reused with permission.

## ELSEVIER LICENSE TERMS AND CONDITIONS

Mar 13, 2020

This Agreement between Utah State University -- Luis Navarro ("You") and Elsevier ("Elsevier") consists of your license details and the terms and conditions provided by Elsevier and Copyright Clearance Center.

License Number	4786200002607
License date	Mar 11, 2020
Licensed Content Publisher	Elsevier
Licensed Content Publication	Elsevier Books
Licensed Content Title	International Geophysics
Licensed Content Author	Michael C. Kelley
Licensed Content Date	Jan 1, 2009
Licensed Content Pages	26
Start Page	1
End Page	26
Type of Use	reuse in a thesis/dissertation
Portion	figures/tables/illustrations
Number of figures/tables/illustrations	1
Format	both print and electronic
Are you the author of this Elsevier chapter?	No
Will you be translating?	No
Title	Storm-Time Equatorial Thermospheric Dynamics and Electrodynamics
Institution name	Utah State University
Expected presentation date	Apr 2020
Portions	Figure 1.1
Requestor Location	Utah State University
	LOGAN, UT 84321
	United States
	Attn: Utah State University
Publisher Tax ID	98-0397604

Figure 2.2 is copyrighted and reused with permission.

## JOHN WILEY AND SONS LICENSE TERMS AND CONDITIONS

Mar 13, 2020

This Agreement between Utah State University -- Luis Navarro ("You") and John Wiley and Sons ("John Wiley and Sons") consists of your license details and the terms and conditions provided by John Wiley and Sons and Copyright Clearance Center.

License Number	4786141232066
License date	Mar 11, 2020
Licensed Content Publisher	John Wiley and Sons
Licensed Content Publication	Journal of Geophysical Research: Space Physics
Licensed Content Title	Equatorial and low latitude thermospheric winds: Measured quiet time variations with season and solar flux from 1980 to 1990
Licensed Content Author	C. G. Fesen, J. W. Meriwether, B. G. Fejer, et al
Licensed Content Date	Aug 1, 1999
Licensed Content Volume	104
Licensed Content Issue	A8
Licensed Content Pages	16
Type of Use	Dissertation/Thesis
Requestor type	University/Academic
Format	Print and electronic
Portion	Figure/table
Number of figures/tables	1
Original Wiley figure/table number(s)	Figure 5
Will you be translating?	No
Title of your thesis / dissertation	Storm-Time Equatorial Thermospheric Dynamics and Electrodynamics
Expected completion date	Apr 2020
Expected size (number of pages)	150
Requestor Location	Utah State University
	LOGAN, UT 84321
	United States
	Attn: Utah State University
Publisher Tax ID	EU826007151



Figure 2.4 is copyrighted and reused with permission.

## ELSEVIER LICENSE TERMS AND CONDITIONS

Mar 13, 2020

This Agreement between Utah State University -- Luis Navarro ("You") and Elsevier ("Elsevier") consists of your license details and the terms and conditions provided by Elsevier and Copyright Clearance Center.

License Number	4786210325039
License date	Mar 11, 2020
Licensed Content Publisher	Elsevier
Licensed Content Publication	Journal of Atmospheric and Terrestrial Physics
Licensed Content Title	F-region storms and thermospheric circulation
Licensed Content Author	H Rishbeth
Licensed Content Date	June–July 1975
Licensed Content Volume	37
Licensed Content Issue	6-7
Licensed Content Pages	10
Start Page	1055
End Page	1064
Type of Use	reuse in a thesis/dissertation
Portion	figures/tables/illustrations
Number of figures/tables/illustrations	1
Format	both print and electronic
Are you the author of this Elsevier article?	No
Will you be translating?	No
Title	Storm-Time Equatorial Thermospheric Dynamics and Electrodynamics
Institution name	Utah State University
Expected presentation date	Apr 2020
Portions	Figure 1
Requestor Location	Utah State University
	LOGAN, UT 84321
	United States
	Attn: Utah State University
Publisher Tax ID	98-0397604

Figure 2.5 is copyrighted and reused with permission.

## JOHN WILEY AND SONS LICENSE TERMS AND CONDITIONS

Mar 13, 2020

This Agreement between Utah State University -- Luis Navarro ("You") and John Wiley and Sons ("John Wiley and Sons") consists of your license details and the terms and conditions provided by John Wiley and Sons and Copyright Clearance Center.

License Number	4786191224170
License date	Mar 11, 2020
Licensed Content Publisher	John Wiley and Sons
Licensed Content Publication	Geophysical Research Letters
Licensed Content Title	Average nighttime F region disturbance neutral winds measured by UARS WINDII: Initial results
Licensed Content Author	B. H. Solheim, G. G. Shepherd, B. G. Fejer, et al
Licensed Content Date	Nov 27, 2004
Licensed Content Volume	31
Licensed Content Issue	22
Licensed Content Pages	4
Type of Use	Dissertation/Thesis
Requestor type	University/Academic
Format	Print and electronic
Portion	Figure/table
Number of figures/tables	1
Original Wiley figure/table number(s)	Figure 4
Will you be translating?	No
Title of your thesis / dissertation	Storm-Time Equatorial Thermospheric Dynamics and Electrodynamics
Expected completion date	Apr 2020
Expected size (number of pages)	150
Requestor Location	Utah State University
	LOGAN, UT 84321
	United States
	Attn: Utah State University
Publisher Tax ID	EU826007151

Figure 2.6 is copyrighted and reused with permission.

## JOHN WILEY AND SONS LICENSE TERMS AND CONDITIONS

Mar 13, 2020

This Agreement between Utah State University -- Luis Navarro ("You") and John Wiley and Sons ("John Wiley and Sons") consists of your license details and the terms and conditions provided by John Wiley and Sons and Copyright Clearance Center.

License Number	4786210225381
License date	Mar 11, 2020
Licensed Content Publisher	John Wiley and Sons
Licensed Content Publication	Geophysical Research Letters
Licensed Content Title	Average nighttime F region disturbance neutral winds measured by UARS WINDII: Initial results
Licensed Content Author	J. T. Emmert, B. G. Fejer, G. G. Shepherd, et al
Licensed Content Date	Nov 27, 2004
Licensed Content Volume	31
Licensed Content Issue	22
Licensed Content Pages	4
Type of Use	Dissertation/Thesis
Requestor type	University/Academic
Format	Print and electronic
Portion	Figure/table
Number of figures/tables	1
Original Wiley figure/table number(s)	Figure 3
Will you be translating?	No
Title of your thesis / dissertation	Storm-Time Equatorial Thermospheric Dynamics and Electrodynamics
Expected completion date	Apr 2020
Expected size (number of pages)	150
Requestor Location	Utah State University
	LOGAN, UT 84321
	United States
	Attn: Utah State University
Publisher Tax ID	EU826007151

Figure 2.7 is copyrighted and reused with permission.

## JOHN WILEY AND SONS LICENSE TERMS AND CONDITIONS

Mar 13, 2020

This Agreement between Utah State University -- Luis Navarro ("You") and John Wiley and Sons ("John Wiley and Sons") consists of your license details and the terms and conditions provided by John Wiley and Sons and Copyright Clearance Center.

License Number	4786170775178
License date	Mar 11, 2020
Licensed Content Publisher	John Wiley and Sons
Licensed Content Publication	Journal of Geophysical Research: Space Physics
Licensed Content Title	DWM07 global empirical model of upper thermospheric storm-induced disturbance winds
Licensed Content Author	C. A. Tepley, D. P. Sipler, R. J. Niciejewski, et al
Licensed Content Date	Nov 26, 2008
Licensed Content Volume	113
Licensed Content Issue	A11
Licensed Content Pages	16
Type of Use	Dissertation/Thesis
Requestor type	University/Academic
Format	Print and electronic
Portion	Figure/table
Number of figures/tables	1
Original Wiley figure/table number(s)	Figure 8
Will you be translating?	No
Title of your thesis / dissertation	Storm-Time Equatorial Thermospheric Dynamics and Electrodynamics
Expected completion date	Apr 2020
Expected size (number of pages)	150
Requestor Location	Utah State University
	LOGAN, UT 84321
	United States
	Attn: Utah State University
Publisher Tax ID	EU826007151

Figure 2.8 is copyrighted and reused with permission.

## JOHN WILEY AND SONS LICENSE TERMS AND CONDITIONS

Mar 13, 2020

This Agreement between Utah State University -- Luis Navarro ("You") and John Wiley and Sons ("John Wiley and Sons") consists of your license details and the terms and conditions provided by John Wiley and Sons and Copyright Clearance Center.

License Number	4786191008967
License date	Mar 11, 2020
Licensed Content Publisher	John Wiley and Sons
Licensed Content Publication	Wiley Books
Licensed Content Title	Thermospheric Dynamics at Low and Mid-Latitudes During Magnetic Storm Activity
Licensed Content Author	J. W Meriwether
Licensed Content Date	Mar 21, 2013
Licensed Content Pages	19
Type of Use	Dissertation/Thesis
Requestor type	University/Academic
Format	Print and electronic
Portion	Figure/table
Number of figures/tables	1
Original Wiley figure/table number(s)	Plate 3
Will you be translating?	No
Title of your thesis / dissertation	Storm-Time Equatorial Thermospheric Dynamics and Electrodynamics
Expected completion date	Apr 2020
Expected size (number of pages)	150
Requestor Location	Utah State University
	LOGAN, UT 84321
	United States
	Attn: Utah State University
Publisher Tax ID	EU826007151
	- - - - -

Figure 2.9 is copyrighted and reused with permission.

## JOHN WILEY AND SONS LICENSE TERMS AND CONDITIONS

Mar 13, 2020

This Agreement between Utah State University -- Luis Navarro ("You") and John Wiley and Sons ("John Wiley and Sons") consists of your license details and the terms and conditions provided by John Wiley and Sons and Copyright Clearance Center.

License Number	4786170829908
License date	Mar 11, 2020
Licensed Content Publisher	John Wiley and Sons
Licensed Content Publication	Journal of Geophysical Research: Space Physics
Licensed Content Title	Radar and satellite global equatorial F region vertical drift model
Licensed Content Author	B. G. Fejer, L. Scherliess
Licensed Content Date	Apr 1, 1999
Licensed Content Volume	104
Licensed Content Issue	A4
Licensed Content Pages	14
Type of Use	Dissertation/Thesis
Requestor type	University/Academic
Format	Print and electronic
Portion	Figure/table
Number of figures/tables	1
Original Wiley figure/table number(s)	Figure 6
Will you be translating?	No
Title of your thesis / dissertation	Storm-Time Equatorial Thermospheric Dynamics and Electrodynamics
Expected completion date	Apr 2020
Expected size (number of pages)	150
Requestor Location	Utah State University
	LOGAN, UT 84321
	United States
	Attn: Utah State University
Publisher Tax ID	EU826007151

Figure 2.10 and 2.15 are copyrighted and reused with permission.

## JOHN WILEY AND SONS LICENSE TERMS AND CONDITIONS

Mar 13, 2020

This Agreement between Utah State University -- Luis Navarro ("You") and John Wiley and Sons ("John Wiley and Sons") consists of your license details and the terms and conditions provided by John Wiley and Sons and Copyright Clearance Center.

License Number	4786170923652
License date	Mar 11, 2020
Licensed Content Publisher	John Wiley and Sons
Licensed Content Publication	Journal of Geophysical Research: Space Physics
Licensed Content Title	Climatology of F region zonal plasma drifts over Jicamarca
Licensed Content Author	A. E. Costa Pereira, A. S. Santos, J. R. Souza, et al
Licensed Content Date	Dec 21, 2005
Licensed Content Volume	110
Licensed Content Issue	A12
Licensed Content Pages	10
Type of Use	Dissertation/Thesis
Requestor type	University/Academic
Format	Print and electronic
Portion	Figure/table
Number of figures/tables	2
Original Wiley figure/table number(s)	Figure 1, Figure 5
Will you be translating?	No
Title of your thesis / dissertation	Storm-Time Equatorial Thermospheric Dynamics and Electrodynamics
Expected completion date	Apr 2020
Expected size (number of pages)	150
Requestor Location	Utah State University
	LOGAN, UT 84321
	United States
	Attn: Utah State University
Publisher Tax ID	EU826007151

Figure 2.12 and 2.14 are copyrighted and reused with permission.

## JOHN WILEY AND SONS LICENSE TERMS AND CONDITIONS

Mar 13, 2020

This Agreement between Utah State University -- Luis Navarro ("You") and John Wiley and Sons ("John Wiley and Sons") consists of your license details and the terms and conditions provided by John Wiley and Sons and Copyright Clearance Center.

License Number	4786170973449
License date	Mar 11, 2020
Licensed Content Publisher	John Wiley and Sons
Licensed Content Publication	Journal of Geophysical Research: Space Physics
Licensed Content Title	Storm time dependence of equatorial disturbance dynamo zonal electric fields
Licensed Content Author	Bela G. Fejer, Ludger Scherliess
Licensed Content Date	Nov 1, 1997
Licensed Content Volume	102
Licensed Content Issue	A11
Licensed Content Pages	10
Type of Use	Dissertation/Thesis
Requestor type	University/Academic
Format	Print and electronic
Portion	Figure/table
Number of figures/tables	2
Original Wiley figure/table number(s)	Figure 1, Figure 5
Will you be translating?	No
Title of your thesis / dissertation	Storm-Time Equatorial Thermospheric Dynamics and Electrodynamics
Expected completion date	Apr 2020
Expected size (number of pages)	150
Requestor Location	Utah State University
	LOGAN, UT 84321
	United States
	Attn: Utah State University
Publisher Tax ID	EU826007151



Figure 2.12 is copyrighted and reused with permission.

## JOHN WILEY AND SONS LICENSE TERMS AND CONDITIONS

Mar 13, 2020

This Agreement between Utah State University -- Luis Navarro ("You") and John Wiley and Sons ("John Wiley and Sons") consists of your license details and the terms and conditions provided by John Wiley and Sons and Copyright Clearance Center.

License Number	4786170973449
License date	Mar 11, 2020
Licensed Content Publisher	John Wiley and Sons
Licensed Content Publication	Journal of Geophysical Research: Space Physics
Licensed Content Title	Storm time dependence of equatorial disturbance dynamo zonal electric fields
Licensed Content Author	Bela G. Fejer, Ludger Scherliess
Licensed Content Date	Nov 1, 1997
Licensed Content Volume	102
Licensed Content Issue	A11
Licensed Content Pages	10
Type of Use	Dissertation/Thesis
Requestor type	University/Academic
Format	Print and electronic
Portion	Figure/table
Number of figures/tables	2
Original Wiley figure/table number(s)	Figure 1, Figure 5
Will you be translating?	No
Title of your thesis / dissertation	Storm-Time Equatorial Thermospheric Dynamics and Electrodynamics
Expected completion date	Apr 2020
Expected size (number of pages)	150
Requestor Location	Utah State University
	LOGAN, UT 84321
	United States
	Attn: Utah State University
Publisher Tax ID	EU826007151

## CURRICULUM VITAE

Luis Navarro

Born: June 20, 1985 in Lima, Peru

---

### EDUCATION

PhD (Physics), Utah State University, USA, 2020

BS (Electronic Engineer), San Marcos Major National University, Peru, 2007

---

### RESEARCH EXPERIENCE

2016 – present      Research Assistant at Upper Electrodynamics Group, USU

2015 – 2016        Research Assistant at Resonance Lidar Group, USU

2014 – 2015        Research Assistant at Rayleigh Lidar Group, USU

2014 – present     Summer Teaching Assistant at Physics, USU

2009 - 2014        Jicamarca Radio Observatory, Geophysical Institute of Peru

---

### PUBLICATIONS

Navarro, L. A., Fejer, B. G., & Scherliess, L. (2019). Equatorial Disturbance Dynamo Vertical Plasma Drifts Over Jicamarca: Bimonthly and Solar Cycle Dependence. *Journal of Geophysical Research: Space Physics*, 124(6), 4833-4841. <https://doi.org/10.1029/2019JA026729>

Navarro, L. A., & Fejer, B. G. (2019). Storm-Time Thermospheric Winds Over Peru. *Journal of Geophysical Research: Space Physics*, 124(12), 10415-10427. <https://doi.org/10.1029/2019JA027256>

Navarro, L. A., & Fejer, B. G. (2020). Storm-time coupling of equatorial nighttime F-region neutral winds and plasma drifts. *Journal of Geophysical Research: Space Physics* (Manuscript in preparation)

---

### PAPERS PRESENTED AT PROFESSIONAL MEETINGS

#### INVITED PAPERS

"Gravity Wave detection over the Jicamarca Radio Observatory using a Nightglow Allsky Imager", **L. A. Navarro**, F. Vargas, G. Swenson, M. A. Milla, CEDAR Workshop, Santa Fe, NM, 2016

"Effects of disturbance winds on equatorial regions recorded by the Fabry-Perot Interferometer network over Peru", **L. A. Navarro**, and B. G. Fejer, CEDAR Workshop, Keystone, Co, 2017

#### CONTRIBUTED PAPERS

"Simultaneous measurements of thermospheric winds and ion drifts at Jicamarca and Arequipa, Peru", **L. A. Navarro**, J. Meriwether, O. Veliz, and J. Chau. CEDAR Workshop, Boulder, Co, 2010.

"Fabry-Perot Interferometer Network in Peru for Aeronomy studies", **L. A. Navarro**, J. Meriwether, O. Veliz, and J. Chau, 10th Latin-American Meeting on Optics, Lasers and Applications, Lima, Peru, 2010.

"A two dimensional approach for Fabry-Perot Interferometer image analysis: Modeling, filtering, and parameter estimation", **L. A. Navarro**, M. Milla, P. Rodriguez, J. Chau, and J. Meriwether, 13th International Symposium of Equatorial Aeronomy, Nasca, Peru, 2012.

"Database of upper atmospheric winds and temperatures measured with the network of Fabry Perot Interferometers in Peru", **L. A. Navarro**, R. Rojas, R. Alonso, M. Milla, J. Chau, and J. Meriwether, CEDAR Workshop, Boulder, Co, 2013.

"Detection and parameter estimation of Gravity Waves from the Jicamarca All-Sky Imager", **L. A. Navarro**, M. Milla, and F. Vargas, Encuentro Cientifico Internacional de Verano, Lima, Peru, 2014.

"The Online System for Lidar Data Handling and Real Time Monitoring of Lidar Operations at ALO-USU", **L. A. Navarro**, V. Wickwar, J. Gamboa, and M. Milla, 27th International Laser Radar Conference, New York City, NY, 2015

"Latitudinal variations on winds and temperature between ALO and USU Na Lidars", **L. A. Navarro**, T. Yuan, F. Vargas, G. Swenson, and A. Liu, CEDAR Workshop, Santa Fe, NM, 2016.

"Magnetic Activity Effects on Night-Time Thermospheric Winds Over Peru using Fabry-Perot Interferometers", **L. A. Navarro**, Physics Colloquium, Logan, UT, 2017

"Seasonal and Solar Flux Dependence of the Equatorial Ionospheric Disturbance Dynamo Electric Fields", **L. A. Navarro**, Physics Colloquium, Logan, UT, 2018

"Seasonal and solar flux dependence of equatorial disturbance vertical plasma drifts over Jicamarca", **L. A. Navarro**, B. G. Fejer, and L. Scherliess, Fall Meeting of the American Geophysical Union, Washington DC, 2018

"Equatorial Ionospheric Electric Field During Geomagnetic Storm Main-Phases", **L. A. Navarro**, Physics Colloquium, Logan, UT, 2019

"Topside Equatorial Vertical Ionospheric Plasma Drifts over Jicamarca", **L. A. Navarro**, and B. G. Fejer, Fall Meeting of American Geophysical Union, San Francisco, CA ,2019

---

#### CO-AUTHORED PAPERS PRESENTED AT PROFESIONAL MEETINGS

"Measurements of Ion Drifts and Thermospheric Neutral Winds at the Jicamarca Radio Observatory" J. Meriwether, **L. A. Navarro**, J. Chau, and B. Fejer, Fall Meeting of the American Geophysical Union, Washington DC, 2010

"Thermospheric wind and temperature climatology for the equatorial region: Results and comparisons with the WAM model predictions", J. Meriwether, J. Makela, J. Huang, D. Fisher, **L. A. Navarro**, O. Veliz, R. Buriti, A. Medeiros, R. Akmaec, T. Fuller-Rowell, and F. Wu, Fall Meeting of the American Geophysical Union, Washington DC, 2011

"Equatorial thermospheric winds: New results using data from a network of three Fabry-Perot interferometers located in central Peru", J. Meriwether, **L. A. Navarro**, M. Milla, and J. Chau, Fall Meeting of the American Geophysical Union, Washington DC, 2013

"Coordinated observations of thermospheric neutral winds and equatorial plasma bubbles from low-latitude sites", J. Makela, J. Meriwether, D. Fisher, N. Chapagain, S. Sanders, R. Buriti, R. Mesquita, **L. A. Navarro**, M. Milla, and J. Chau, Fall Meeting of the American Geophysical Union, Washington DC, 2013

"Estimation of three-dimensional wind maps of the Ionosphere over the central region of Peru using the FPI network", J. Gamboa, **L. A. Navarro**, M. Milla, and J. Meriwether, 10th Latin American Conference on Space Geophysics (COLAGE), Cusco, Peru, 2014

"A new approach to the mapping of the equatorial neutral wind field", J. Meriwether, J. Makela, **L. A. Navarro**, B. Harding, and M. Milla, 40th COSPAR Scientific Assembly, Moscow, Russia, 2014

"FPI Observations of Enhanced Temperatures and Vertical Wind Activity in the Auroral Thermosphere", J. Meriwether, D. Hampton, M. Larsen, B. Harding., and **L. A. Navarro**, Fall Meeting of the American Geophysical Union, Washington DC, 2018

"Variability of Ionospheric Storm-Time Electric Fields", B. G. Fejer, **L. A. Navarro**, and S. Y. Sazykin, Fall Meeting of the American Geophysical Union, San Francisco, CA, 2019

"Storm-Time Ionospheric Electrodynamics During the September 2017 Geomagnetic Storm", S. Y. Sazykin, A. Newheart, B. G. Fejer, **L. A. Navarro**, J. D. Huba, A. Coster, V. N., Coffey, M. O. Chandler, M. R. Hairston, and P. J. Erickson, Fall Meeting of the American Geophysical Union, San Francisco, CA, 2019

- "Observations of Vigorous Vertical Thermospheric Neutral Winds at High Latitudes", J. Meriwether, D. Hampton., M. Conde, B. Harding, and **L. A. Navarro**, Fall Meeting of the American Geophysical Union, San Francisco, CA, 2019
- "Strong vertical winds observed from Eagle, AK during the superstorm of 17 March 2015", J. Meriwether, D. Hampton, M. Conde, **L. A. Navarro**, H. Wu, and R. Varney, 43rd COSPAR Scientific Assembly, Sydney, Australia, 2020
- "Storm-time Ionospheric Electrodynamics During the September 7-9, 2017 Geomagnetic Storm", S. Y. Sazykin, A. Newheart, A. Coster, J. D. Huba, B. G. Fejer, M. Hairston, V. Coffey, M. Chandler, P. Erickson, and **L. A. Navarro**, 43rd COSPAR Scientific Assembly, Sydney, Australia, 2020